การปลูกผลึกด้วยลำโมเลกุลของโครงสร้างนาโนชนิดแกลเลียมแอนติโมไนด์
และอินเดียมแอนติโมไนด์บนฐานรองชนิดเจอร์เมเนียมระนาบ (001)

นางสาวซอน

วิทยานิพนธ์นี้เป็นส่วนหนึ่งของการศึกษาตามหลักสูตรปริญญาวิศวกรรมศาสตรดุษฎีบัณฑิต
สาขาวิชาวิศวกรรมไฟฟ้า ภาควิชาวิศวกรรมไฟฟ้า
คณะวิศวกรรมศาสตร์ จุฬาลงกรณ์มหาวิทยาลัย
ปีการศึกษา 2560
ลิขสิทธิ์ของจุฬาลงกรณ์มหาวิทยาลัย

MOLECULAR BEAM EPITAXIAL GROWTH OF GASB AND INSB

NANOSTRUCTURES ON (001) GE SUBSTRATES

Miss Zon

A Dissertation Submitted in Partial Fulfillment of the Requirements
for the Degree of Doctor of Philosophy Program in Electrical Engineering
Department of Electrical Engineering
Faculty of Engineering
Chulalongkorn University
Academic Year 2017
Copyright of Chulalongkorn University

Thesis Title	MOLECULAR BEAM EPITAXIAL GROWTH OF GASB AND INSB NANOSTRUCTURES ON (001) GE SUBSTRATES
By	Miss Zon
Field of Study	Electrical Engineering
Thesis Advisor	ProfessorSomsak Panyakaew, D.Eng.

Accepted by the Faculty of Engineering, Chulalongkorn University in Partial Fulfillment of the Requirements for the Doctoral Degree

....Dean of the Faculty of Engineering
(Associate ProfessorSupot Teachavorasinskun, D.Eng.)

THESIS COMMITTEE

....Chairman
(ProfessorYasuhiko Arakawa, D.Eng.)

....Thesis Advisor
(ProfessorSomsak Panyakaew, D.Eng.)

....Examiner
(ProfessorSongphol Kanjanachuchai, Ph.D.)

....Examiner
(Associate ProfessorSomchai Ratanathammaphan, D.Eng.)

....External Examiner
(Associate ProfessorSuwit Kiravittaya, D.Eng.)

....External Examiner
(Dr. Chanchana Thanachayanont, Ph.D.)

ซอน : การปลูกผลึกด้วยลำโมเลกุลของโครงสร้างนาโนชนิดแกลเลียมแอนติโมไนด์และอินเดียมแอน ติโมไนด์บนฐานรองชนิดเจอร์เมเนียมระนาบ (001) (MOLECULAR BEAM EPITAXIAL GROWTH OF GASB AND INSB NANOSTRUCTURES ON (001) GE SUBSTRATES) อ. ที่ปรึกษาวิทยานิพนธ์หลัก: สมศักดิ์ ปัญญาแก้ว, หน้า.

วิทยานิพนธ์นี้เป็นการศึกษาโครงสร้างนาโนที่ก่อตัวขึ้นเองของแกลเลียมแอนติโมไนด์และอินเดียม แอนติโมไนด์ (ควอนตัมด็อต) ที่ถูกสร้างขึ้นบนฐานรองชนิดเจอร์เมเนียมระนาบ (001) ด้วยการปลูกผลึกด้วยลำ โมเลกุลในโหมดการปลูกสทรานสกี-คราสตานอฟ การวัดด้วยกล้องจุลทรรศน์แรงอะตอมแสดงคุณสมบัติทาง โครงสร้าง และ การวัดโฟโตลูมิเนสเซนต์แสดงคุณสมบัติทางแสง การปลูกแกลเลียมอาร์เซไนด์ที่มีลักษณะมีขั้ว บนเจอร์เมเนียมที่ไม่มีขั้วก่อให้เกิดโดเมนเฟสตรงข้าม เราสามารถควบคุมการปลูกผลึกให้ได้โดเมนเฟสตรงข้ามที่ เรียบและมีพื้นที่ใหญ่ในระดับตารางไมครอน ซึ่งเพียงพอที่ทำให้เกิดอาเรย์ของควอนตัมด็อตในแต่ละโดเมน ผลกระทบของการมีโดเมนเฟสตรงข้ามต่อการก่อตัวของควอนตัมด็อตถูกนำมาอภิปราย การเปลี่ยนเงื่อนไขการ ปลูกผลึกทำให้ควอนตัมด็อตที่สร้างได้มีลักษณะที่แตกต่างกันอย่างเห็นได้ชัด การปลูกที่อุณหภูมิ 400-450 องศา เซลเซียสทำให้แกลเลียมแอนติโมไนด์/แกลเลียมอาร์เซไนด์ควอนตัมด็อตเกิดบนพื้นที่ผิวเรียบภายในโดเมนเป็น ส่วนมาก ควอนตัมด็อตมีการเปลี่ยนรูปร่างจากฐานวงกลมเป็นฐานสี่เหลี่ยมผืนผ้าเมื่อมีการปลูกหนาเกิน 2.5 ชั้น อะตอม ที่อัตราการปลูกต่ำประมาณ 0.11 และ 0.09 ชั้นอะตอมต่อวินาที ที่อุณหภูมิปลูกประมาณ 450 องศา เซลเซียส ควอนตัมด็อตบนผิว มีโครงสร้างที่ยืดไปในทิศ [110] ซึ่งโดเมนเฟสตรงข้ามของแกลเลียมอาร์เซไนด์มี ลักษณะตั้งฉากกัน แสงที่เปล่งจากควอนตัมด็อตนี้มีการเลื่อนในทิศความยาวคลื่นสั้นเมื่อเพิ่มกำลังในการกระตุ้น ซึ่งเป็นลักษณะของการเรียงแถบพลังงานแบบชนิดที่สอง ตำแหน่งการก่อตัวสำหรับควอนตัมด็อตชนิดอินเดียม แอนติโมไนด์ต่างจากควอนตัมด็อตชนิดแกลเลียมแอนติโมไนด์คือเกิดควอนตัมด็อตที่ขอบของโดเมน ซึ่งเป็นตัว แหน่งที่ผิวแกลเลียมอาร์เซไนด์ในสองทิศทางมาพบกัน ขนาด รูปร่าง ความหนาแน่น และ ตำแหน่งของ ควอนตัมด็อตเปลี่ยนแปลงไปตามอุณหภูมิของการปลูกและอัตราเร็วในการปลูก การใช้อุณหภูมิที่สูงและอัตราเร็ว ในการปลูกต่ำก่อให้เกิดควอนตัมด็อตขนาดใหญ่ขึ้นซึ่งมีลักษณะเดียวกันกับควอนตัมด็อตชนิดแกลเลียมแอนติโม ไนด์ การเพิ่มอัตราเร็วในการปลูกจาก 0.023 ไปเป็น 0.14 ชั้นอะตอมต่อวินาที ทำให้ได้ควอนตัมด็อตความ หนาแน่นสูง (ประมาณ 10^{10} ด็อตต่อตารางเซนติเมตร) ทั้งในโดเมนและบนขอบโดเมนแต่ขนาดและรูปร่างของ ควอนตัมด็อตมีความแตกต่างกันอย่างมาก งานวิจัยนี้ทำให้ได้รับความรู้เกี่ยวกับความสัมพันธ์ระหว่างเงื่อนไข การปลูกผลึกด้วยลำโมเลกุลและลักษณะรูปร่างของควอนตัมด็อตที่สร้างด้วยแอนติโมนี และ ผลงานนี้สามารถ นำไปใช้ต่อยอดในการสร้างอุปกรณ์อิเล็กทรอนิกส์และอิเล็กทรอนิกส์เชิงแสงที่ใช้โครงสร้างนาโนควอนตัมด็อต

ภาควิชา	วิศวกรรมไฟฟ้า	ลายมือชื่อนิสิต _____
สาขาวิชา	วิศวกรรมไฟฟ้า	ลายมือชื่อ อ.ที่ปรึกษาหลัก _____
ปีการศึกษา	2560	

5771450421 : MAJOR ELECTRICAL ENGINEERING

KEYWORDS: NANOSTRUCTURE / GASB / INSB / MOLECULAR BEAM EPITAXY

ZON: MOLECULAR BEAM EPITAXIAL GROWTH OF GASB AND INSB NANOSTRUCTURES ON (001) GE SUBSTRATES. ADVISOR: PROF.SOMSAK PANYAKAEW, D.Eng., pp.

The self-assembled GaSb and InSb nanostructures (quantum dots, QDs) are grown on (001) Ge substrates in Stranski-Krastanow growth mode by molecular beam epitaxy. The structural properties are characterized by *ex situ* atomic force microscopy (AFM), and the related optical properties are observed by photoluminescence (PL) spectroscopy. Growing of polar GaAs on non-polar Ge creates anti-phase domains (APDs). By careful controlling of growth, APDs surface becomes flat and having large surface area ($\sim\mu m^2$) which is sufficient to form QD array in each domain. The effects of APDs on the formation of QDs are discussed. By varying the growth conditions, different QD morphologies for two types of QDs; GaSb and InSb, are observed. At the growth temperature of 400-450ºC, GaSb/GaAs QDs are mainly formed on the flat area of each APD. Only a few QDs are also found along the APD boundaries (APBs). The self-assembled GaSb QD shape transforms from circular to rectangular based shape by GaSb depositing over 2.5 monolayer (ML) with the low growth rates ~0.11 ML/s and ~0.09 ML/s, at low growth temperature ~450ºC. The free-standing GaSb/GaAs QDs elongate along [110] direction on (001) GaAs surface having the orthogonal nature of GaAs APDs. The PL emission from QDs exhibits a strong blue shift with increasing the excitation power, which is the characteristic of type-II band alignment. Different from the GaSb QD nucleation position, the low-growth-rate InSb QDs are mostly formed at the APBs, where two orthogonal GaAs surfaces meet. The QD size, shape, density and position are varied with the QD growth temperature and In growth rate. At higher growth temperature and low growth rate, larger InSb QDs are observed as qualitatively similar to the GaSb QD system. By increasing growth rate from 0.023 ML/s to 0.14ML/s, the high density ($\sim10^{10}$cm^{-2}) InSb QDs array is obtained, and the QDs accumulate in both APDs and APBs. The QD size and shape are very different on APBs and on the flat GaAs APDs. This work enhances our understanding of the relation between molecular beam epitaxial growth conditions and antimony-based QD morphologies and it provides a basis for practical realization of electronic and opto-electronic devices based on QD nanostructures.

Department:	Electrical Engineering	Student's Signature	_____
Field of Study:	Electrical Engineering	Advisor's Signature	_____
Academic Year:	2017		

ACKNOWLEDGEMENTS

CONTENTS

จุฬาลงกรณ์มหาวิทยาลัย
CHULALONGKORN UNIVERSITY

Chapter 1

Introduction

1.1. Historical Background

III-V compound semiconductor nanostructures provide a wide range of very different electronic and optical properties from the bulk materials by combining two or more materials. In low-dimensional nanostructures; quantum dot (QD), quantum wire (QWR) and quantum well (QW), charge carriers are confined and can move in corresponding regions accompanying with the carrier density of states and energy levels which belong to the structural dimensions [1]. Due to their unique properties such as tuneable energy bandgap and controllable carrier movement directions, there is increasing interest in preparing, study and applications of low dimensional nanostructures.

It has been a few decades that semiconductor QDs based on III-V compounds have attracted much attention as the next generation nanostructures for novel devices. Zero-dimensional QD nanostructure is an interesting structure for both study of physics and device applications because of the obtained delta-like density of states and discrete energy levels from three-dimensional confinement. The development of crystal growth and post-growth processing techniques such as molecular beam epitaxy (MBE) and metal-organic chemical vapour deposition (MOCVD) provide route to realize complicated and complex low-dimensional nanostructures for practical applications [2, 3].

For the development of optoelectronic and high-speed electronic devices, the integration of III-V compound materials on group IV elemental substrates, such as silicon (Si) and germanium (Ge), has attracted the attention of many research groups. Optoelectronic devices based on a combination of group IV and III-V material systems might offer a new possibility for realizing novel devices with new functionalities. This heterostructure allows the combination of different material properties by utilizing the benefits of different materials. The advantage of similar lattice constants of GaAs and Ge (lattice mismatch of less than 0.1%) offers the defect-free and minimal generation of dislocation during epitaxial growth while there is a large lattice mismatch of ~4% between GaAs and Si [4, 5]. Growth of GaAs on

Ge has been received great interest for optoelectronic devices such as high efficiency multi-junction solar cells, multiband photodetectors due to their bandgap properties, direct/indirect, wide/narrow bandgaps and the electronic properties, electron mobility, carrier lifetime, etc. [6-8].

Antimonide-based narrow bandgap semiconductors persuade the great attention of many research groups in recent years. Combination of group–III elements (Ga, In, Al) and Sb provides compound semiconductors with unique bandgap structure and physical properties. Their flexibility regarding bandgap tailoring over a wide spectral range (visible to infrared (IR) wavelength) drives them to the first candidate materials for fabrication of electronic and photonic devices such as third generation IR photo-detectors, mid- and far- IR quantum cascade lasers for optical fiber communication [9-11]. Our research will focus on the GaSb/GaAs and InSb/GaAs semiconductor nanostructures grown on (001) Ge substrate. High lattice mismatch of GaSb/GaAs (~7.8%) and InSb/GaAs (~14.6%) heterostructure systems allows the deposition of self-assembled QDs in Stranski-Krastanow (SK) growth mode.

Type-II band structure has potential applications in basic studies of quantum confinement as well as electronic and optical devices. Type-II band alignment of GaSb/GaAs and InSb/GaAs QDs generates quantum confinement effects by separating holes in the QDs and electrons in the GaAs matrix. Most of studied III-V QD material systems has type-I band alignment e.g. InAs/GaAs. The nature of type-I system is that both electrons and holes are confined in QD, and results in fast recombination rates [12-14]. On the contrary, in the type-II QD, less overlapping between electron and hole wave functions results in a long carrier lifetime, hence it leads to be useful for single carrier, unipolar storage devices such as optical memory, and the detecting devices such as IR photodetectors [15-17]. Moreover, by varying the composition of QDs as a function of surrounded matrix layer, the type-II staggered active region can be designed to work at a wide wavelength range (near IR to mid IR region) and longer carrier lifetime [18]. However, the number of different lattice mismatch, percentage of material composition and surface energy combinations within three atomic types (GaSb/GaAs) or four atomic types (InSb/GaAs) of materials can highly affect their properties and performances for

optoelectronic applications. Therefore, the systematically growth study on GaSb/GaAs and InSb/GaAs nanostructures is needed to probe and develop for employing them in nano-electronic and nano-photonic devices.

In this dissertation, we focus on the growth of type-II GaSb/GaAs, and InSb/GaAs on (001) Ge substrate. The unique properties and the mechanism of type-II band system have been described in Chapter 2. B.R. Bennett *et al*., reported that the GaSb/GaAs system and InSb/GaAs system grown on GaAs substrates have photo response in the range of 1-1.3 eV and 1-1.2 eV revealed by low-temperature photoluminescence measurement [19]. InSb/GaAs system can have in both type-I and type-II band alignment properties based on the amount of In-Ga and Sb-As composition into QDs, while GaSb/GaAs system performs as type-II band characteristics [20]. The emission energy can be varied by means of various QD natures, and which can be controlled by utilizing optimum growth conditions and parameters. The characteristics of QD (density, size, uniformity and composition) influence on the electrical and optical properties of all the applications and realization of devices. Therefore, various growth parameters such as deposition time of QDs, growth rate of QDs and growth temperature come up to be studied and characterized in this research. The surface exchange reaction between Sb-As and/or In-Ga (intermixing effect) at the interfaces is also a considered topic.

Apart of type-II QD system, epitaxial growth of polar GaAs material on group-IV non-polar Ge substrate is interesting topic because of introducing the formation of anti-phase domains (APDs) containing APD boundaries (APBs). GaAs APDs can grow and align in two crystallographic orientations by 90º rotating with respect to each other. The surface roughening and the APDs densities can be suppressed by optimum growth mechanisms [21-24].

These above issues lead to the changing of quantum confinement effect and carrier dynamic behaviour of the nanostructures by means of type-II band alignment nature. So far, due to the technical challenges to grow III-V semiconductors on Ge substrate, comparative study of structural and optical properties of proposed nanostructures (GaSb/GaAs and InSb/GaAs on Ge) has still remained and rarely reported. Moreover, Sb-based epitaxial growth on Ge has the great potential not only for longer wavelength IR photodetectors but also for cost reduction in IR systems. Ge

has higher thermal conductivity which makes better cooling for electronic components and cooling can be further enhanced using the thinner substrates. Although a few or several degree off cut (001) Ge substrate is a possible solution to avoid the occurrence of steps of monatomic height, it is reported that APDs formation depends on the controllable growth conditions; such as growth temperature, GaAs nucleation mechanisms, dependent APDs formation [4, 25]. Moreover, conventional (001) Ge substrate is compatible with standard semiconductor processing and larger as well as cheaper wafers are available.

1.2. Objective

This research investigates the relation between structural and optical properties of GaSb/GaAs and InSb/GaAs nanostructures grown on (001) Ge substrates. The growth of QDs focuses on the simple growth of GaSb/GaAs and InSb/GaAs nanostructures, and the influence of growth temperature, QD deposition amount and QD deposition rate on the QDs morphologies and optical properties.

1.3. Overview

This dissertation presents the detailed study of the growth of GaSb/GaAs and InSb/GaAs self-assembled QDs by MBE.

Chapter 2 presents the brief overview of the basic concepts of self-assembled quantum dot (QD) nanostructure and growth methods of low-dimensional nanostructure. Moreover, the mechanism of type-II band alignment of GaSb/GaAs nanostructure and the atomic process of GaAs APDs and APBs formation on (001) Ge substrate are described. In Chapter 3, the experimental details accompanying with the *in situ* monitoring tool and *ex situ* measurement tools are provided. Chapter 4 presents the optimum conditions to obtain flat GaAs surface grown on (001) Ge substrate by suppressing high density APD formation. In Chapter 5, the growth of GaSb/GaAs QDs on (001) Ge substrate and related optical properties are studied. In Chapter 6, by varying growth parameters (growth temperature, GaSb deposited amount and Ga growth rate), the QD shape transformation and the improvement of optical quality of QDs are observed. The generic growth scenarios for the self-assembled InSb/GaAs as a function of growth rate and local growth position on the

material diffusion are developed and discussed in Chapter 7. The conclusion of this dissertation is provided in Chapter 8.

Chapter 2

Background Knowledge

In this chapter, the basic concepts of self-assembled QD nanostructure and growth methods of low-dimensional nanostructure are briefly discussed. The mechanism of type-II band alignment and the formation of APDs and APBs are also described.

2.1 Low-Dimensional Nanostructures

In low-dimensional nanostructures, the charge carriers can be restricted by the dimensions of nanostructures. As quantum well (QW), quantum wires (QWR), and quantum dot (QD) can be characterized by the confinement dimensions; one-, two-, and three- dimensional confinements, respectively. This is the significant different from the bulk semiconductor, in which the carrier can move freely in all directions, and there is no quantum confinement effects. When the size or dimension of a material is reduced to the nanometre range, it is well-known as quantum nanostructure with quantum confinement effects. The size quantization effect will be observed when the dimension of the material becomes small enough and comparable to the mean free path of the de Broglie wavelength of carrier [26]. The wave-like properties and the length scale of carriers in the quantization phenomena can be described by

$$\lambda_{de\,Broglie} = \frac{h}{p} = \frac{h}{\sqrt{3m_{eff}k_BT}} \tag{2.1}$$

where the de Broglie wavelength of carrier $\lambda_{de\,Broglie}$, depends on the carrier effective mass m_{eff}, and temperature T. k_B and h are Boltzmann and Planck constants, and p is the carrier momentum.

The discrete energy levels like an atom and delta-like density of states obtained by three-dimensional confinements make QD as an artificial atom. Figure 2.1 shows a schematic comparison between a bulk semiconductor, a waveguide for visible light, a QD, and an atom. In a case of atom, the electronic state is described by

discrete energy level, whereas the band theory is used in the bulk-crystal structure. Figure 2.2 shows the schematic views and density of states (D.O.S) of (a) bulk, (b) QW, (c) QWR and (d) QD. Because of having zero dimension, QDs have delta-like-function density of state.
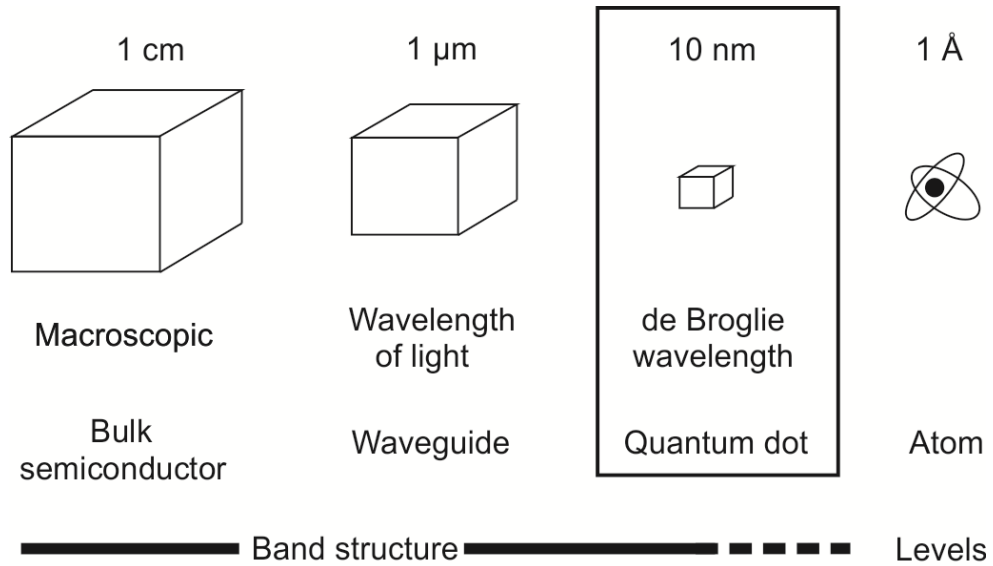
Figure 2.1 Schematic comparison of typical dimensions of bulk semiconductor,
waveguide for visible light, QD, and atom [26].

Assuming parabolic band dispersion, band-edge electron states of semiconductors can be described by the Shrödinger equation as

$$\left[-\frac{\hbar^2}{2m^*}\nabla^2 + V(r)\right]F(r) = E\,F(r) \qquad (2.2)$$

where, m^* is the effective mass, $\hbar$ is the reduced Planck's constant, $r = (x,\ y,\ z)$ is the carrier position vector, $V(r)$ is the confinement potential due to band offset and strain; $F(r)$ is the envelope wave function, and E is the carrier energy.

From Eq. (2.2), the carrier energy E for bulk, QW, QWR and QD can be expressed as follows; [27]

$$E_{bulk} = E(\mathbf{k}) = \frac{\hbar^2 k^2}{2m^*} \qquad (2.3)$$

$$E_{\text{QW}} = E(\mathbf{k}) = \frac{\hbar^2 k_{//}^{\,2}}{2m^*} + E_{n,z} \tag{2.4}$$

$$E_{\text{QWR}} = E(\mathbf{k}) = \frac{\hbar^2 k_{\perp}^{\,2}}{2m^*} + E_{m,y} + E_{n,z} \tag{2.5}$$

$$E_{\text{QD}} = E(\mathbf{k}) = E_{l,x} + E_{m,y} + E_{n,z} \tag{2.6}$$

where $\mathbf{k} = (k_x, k_y, k_z)$ is the wave vector of carriers, $k^2 = k_x^2 + k_y^2 + k_z^2$, $k_{//}^2 = k_x^2 + k_y^2$, and $k_{\perp}^2 = k_x^2$. The energies $E_{l,x}$, $E_{m,y}$ and $E_{n,z}$ which are a function of the potential $V(\mathrm{r})$, depend on the quantum numbers l, m, and n.

The density of states per unit volume $D(E)$ which is the number of states between the energy E and $E + dE$, of each quantum nanostructure is written as

$$D_{bulk}(E) = \frac{1}{2\pi^2} \left(\frac{2m^*}{\hbar^2} \right)^{3/2} E^{1/2} \tag{2.7}$$

$$D_{QW}(E) = \frac{m^*}{\pi \hbar^2} \sum_n \Theta(E - E_{n,z}) \tag{2.8}$$

$$D_{QWR}(E) = \frac{N_{wi}}{\pi} \frac{\sqrt{2m^*}}{\hbar} \sum_{m,n} \frac{1}{\sqrt{E - E_{m,y} - E_{n,z}}} \tag{2.9}$$

$$D_{QD}(E) = 2N_D \sum_{l,m,n} \delta(E - E_{l,x} - E_{m,y} - E_{n,z}) \tag{2.10}$$

where Θ is the Heaviside's unit step function, N_{wi} is the area density of the quantum wires, δ is the delta function, and N_D is the volume density of the QD.

Bulk	Quantum well	Quantum wire	Quantum dot
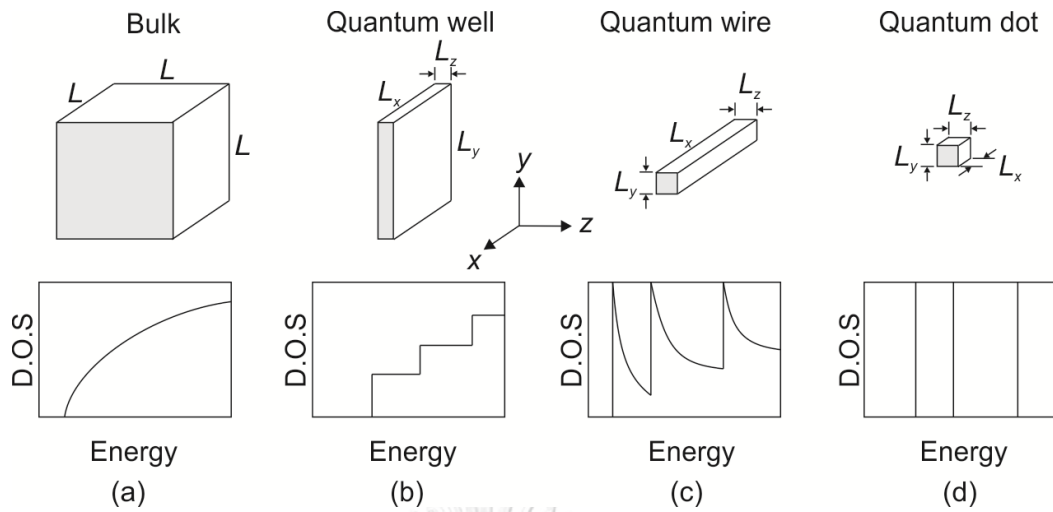
Figure 2.2 Schematic views and density of states (D.O.S) of (a) bulk, (b) quantum well, (c) quantum wire, and (d) quantum dot. L is in macroscopic scale (~cm), while L_x, L_y, L_z are in nanoscale.

2.2   Strain Effects on Quantum Dot Formation

For the lattice-matched epitaxy, the deposited material has almost the same lattice constant as that of the substrate material. When the layer having different lattice constant with a substrate is grown on the substrate, a strained epitaxial layer is obtained by the induced stress/strain in the system. Therefore, highly lattice mismatched heteroepitaxy creates self-assembled QDs. Figure 2.3 shows the schematic representation of lattice-matched and lattice-mismatched system. There are two kinds of strain called compressive and tensile strains. The structural aspect of compressive strain mechanism is shown in Figure 2.3 (b), and the tensile strain mechanism is shown in Figure 2.3 (c). Within the layer growth, the deposited material and the in-plane lattice constant of the substrate material are matched by the biaxial stress (force) laterally. The in-plane strain, $\varepsilon_{//}$, is given by

$$\varepsilon_{//} = \varepsilon_{xx} = \varepsilon_{yy} = (a_s - a_e)/a_e \qquad (2.11)$$

where a_e is the lattice constant of the deposited material and a_s is the lattice constant of the substrate. The strain in the growth direction is given by

$$\varepsilon_\perp = \varepsilon_{zz} = -(2\sigma/(1-\sigma))\,\varepsilon_{//} \qquad (2.12)$$

where σ is Poisson's ratio. For tetrahedral semiconductors, σ is approximately 1/3, so that $\varepsilon_\perp \approx \varepsilon_{//}$. The total strain can be described by a uniaxial component,

$$\varepsilon_{ax} = \varepsilon_\perp - \varepsilon_{//} \qquad (2.13)$$

And a hydrostatic component ε_{vol} $(=\Delta V/V)$,

$$\varepsilon_{vol} = \varepsilon_{xx} + \varepsilon_{yy} + \varepsilon_{zz} \approx \varepsilon_{//} \qquad (2.14)$$

ε_{ax} and ε_{vol} are the terms used to predict the band gap of strained layers by deformation potential theory. If the strained material is depostied beyond the critical thickness, the total energy exceeds the energy of the relaxed sytem, and the relaxation process occurs.

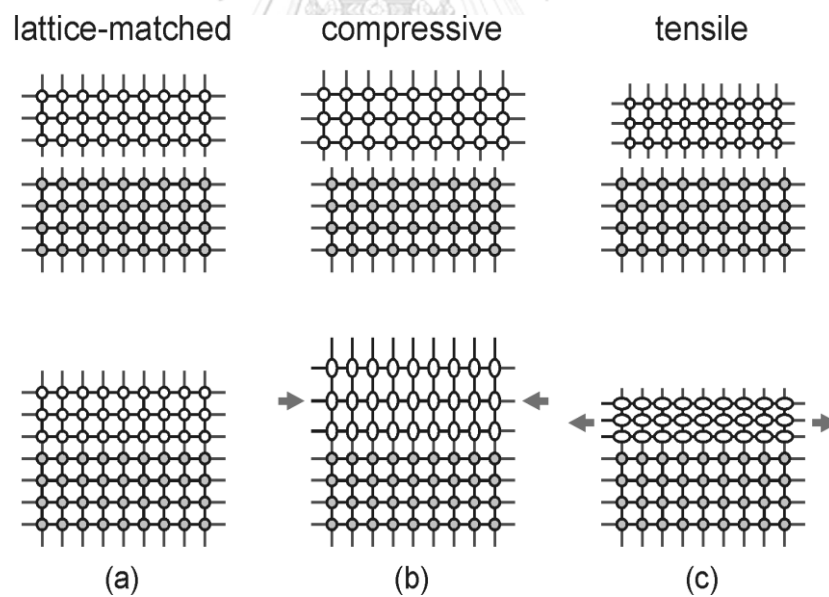Figure 2.3 Schematic representation of (a) unstrained layer, (b) compressive strained layer, and (c) tensile strained layer. The closed circles represent atoms of the substrate material and the open circles are atoms of the deposited material. In (b) and (c) the lattice constants of the deposited material are different from the epitaxial layer. The arrows in (b) and (c) represent forces (stresses) exerted on the epitaxial layer.

2.3   Growth Modes: Stranski-Krastanow (SK) mode

The most frequently occurring modes of epitaxial crystal growth on the surface under near equilibrium conditions are depicted in Figure 2.4 (a-e). They are layer-by-layer or Frank-van der Merwe (FM-mode) (Figure 2.4 (a)), step flow (SF-mode) (Figure 2.4 (b)), layer plus island or Stranski-Krastanov (SK-mode) (Figure 2.4 (c)), island or Volmer-Weber (VW-mode) (Figure 2.4 (d)) and columnar growth mode (CG-mode) (Figure 2.4 (e)). The type of epitaxial growth will be determined by surface/interface free energy model [28] and the lattice match/mismatch systems. If the change of total energy of a surface before and after deposition is considered as $\Delta\gamma$,

$$\Delta\gamma = \gamma_e + \gamma_i - \gamma_s \qquad (2.15)$$

where, γ_e, γ_i and γ_s are denoted as the free energies of the epilayer/vacuum interface, epilayer/substrate interface and substrate/vacuum interface, respectively. If the epitaxial layer and substrate are lattice matched or has small lattice mismatch, and $\Delta\gamma < 0$, layer-by-layer growth mode occurs because the deposited atoms are more strongly bond to substrate than to each other. Thus, this can be so called FM-mode as shown in Figure 2.4 (a). The FM-mode to the VW-mode can be changed by variation of this energy relation. The difference between layer-by-layer or FM-mode and island or VW-mode can be considered as $\Delta\gamma > 0$, in which circumstance, the lattice mismatch is higher and the deposited materials more strongly attract to themselves than those to the substrate results the island growth, and which can be called VW-mode (Figure 2.4 (d)). The "intermediate" case between FM-mode and VW-mode is known as SK-mode, in which case, the growth initially proceeds in layer-by-layer mode. After arriving the critical layer thickness of epilayer material, the accumulation of large strain energy occurs and strain relaxed 3D islands are formed to reduce its energy. This is well known as layer plus island growth mode or SK-mode as shown in Figure 2.4 (c).

Difference from the SK- and VW-modes, CG-mode can occur by depositing the material in the shape of column. In SK- and VW- modes, when the grown epilayer thickens, the deposited phase islands merge each other and cover the whole substrate

surface with the variations of surface thickness. On the contrary to those of growth modes, CG-mode can generate the columns of deposited materials without merging with each other, i.e., the separated columns throughout the surface is achieved. In addition, similar to the FM-mode or layer-by-layer mode for the case of lattice matched system, the so-called step flow SF-mode can also be observed. In which, 2D nucleation or layer deposition can be occur on the misoriented substrate in the specific direction. Because of the crystallographic misorientation and the vicinal atomic planes of the crystal lattice of the substrate, the substrate surface can be broken up into the monoatomic steps or terrace surfaces and edges. Under the optimum growth conditions; high enough growth temperature and low enough flux, the deposited materials can directly incorporate into the surface steps or edges and which proceeds the further steps growth along the terraces as shown in Figure 2.4 (b).
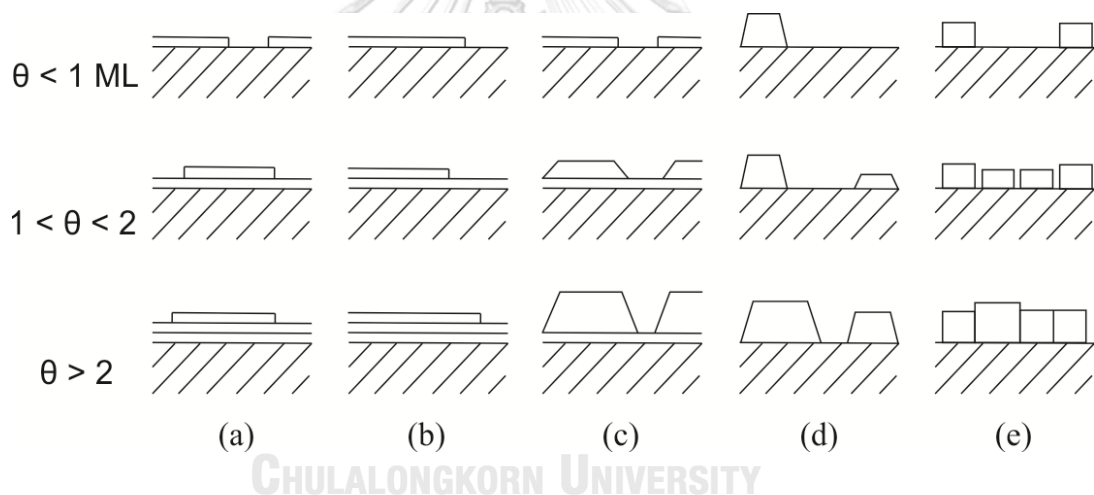
Figure 2.4 Schematic representation of the five crystal growth modes most frequently occurring on flat surfaces of substrate crystals. (a) Layer-by-layer or Frank-van der Merwe (FM-mode); (b) step flow (SF-mode); (c) layer plus island or Stranski-Krastanov (SK-mode); (d) island or Volmer-Weber (VW-mode); (e) columnar growth mode (CG-mode). θ represents the coverage in monolayers (Redrawn from Herman et al., 2004) [29].

Figure 2.5 shows the island formation during epitaxial growth in SK growth mode. SK growth mode provides defect-free QD structures. In SK growth mode, a few monolayers (MLs) of strained material deposit and grow first. Then after over-growth at a critical thickness, 3D strained relaxed islands are occurred. During the

layer growth, elastic strain energy, $E(el)$ builds up due to the lattice mismatch, and it is given by

$$E(el) = \lambda \varepsilon^2 At \qquad (2.16)$$

where λ is the elastic modulus, ε is the misfit, and A is surface area. The total energy for the layer-by-layer growth increases as a function of the film thickness, t. The deposited 3D islands formed in the SK growth mode are called self-assembled QDs.
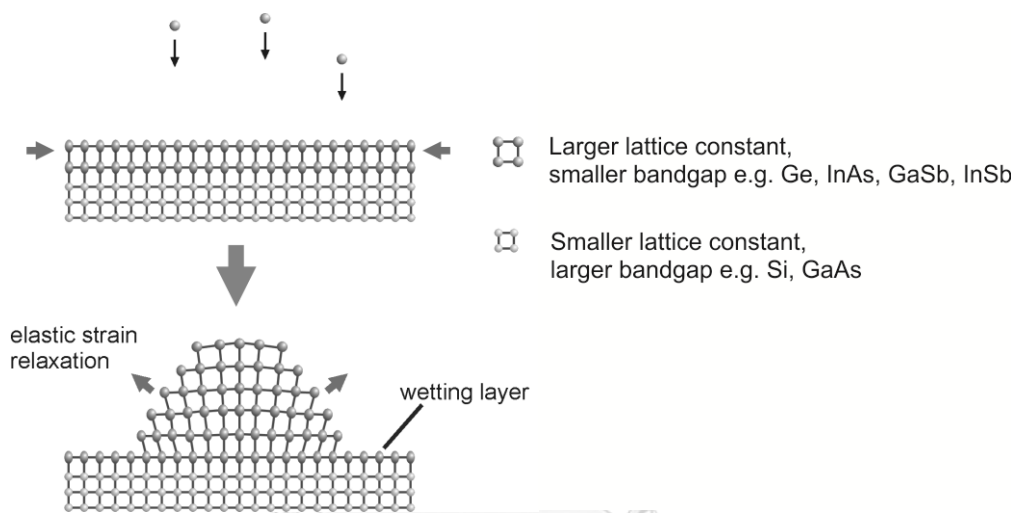
Figure 2.5 Illustration of island formation during epitaxial growth of a semiconductor material (dark) on top of another semiconductor with a smaller (by a few percent) lattice constant (bright). The cluster formation is energetically favourable, because the lattice can elastically relax compressive strain and, thus, reduce strain energy.

2.4 Material Consideration: Antimonide-based III-V Nanostructures

After the multi-elements IR detectors; first generation for scanning system and second generation for staring systems, third generation systems are being developed nowadays. Type-II InAs/GaInSb strain layer superlattices (SLSs) and QD IR photodetectors (QDIPs) are the new promising candidates to raise the primary objectives of IR detector system; multiband sensing and boosting the sensitivity to maximize the identification range. The applications requiring multiband capability and fast response become the challenge of the HgCdTe technology. Type-II Sb-based

supperlattices (SL) and QD structures are the relatively new alternative IR material system, and has great potential for using at long and very long wavelength IR (VLWIR) spectral ranges with performance comparable to HgCdTe [30]. Moreover, QD IR system is the strong demanded component not only for detecting but also for source and sensing in mid-IR and far-IR regions. Figure 2.6 shows the band gap energy as a function of lattice constant for the Sb-based III-V material systems. In this dissertation, GaSb/GaAs and InSb/GaAs material systems will be concentrated. GaSb/GaAs system and InSb/GaAs system grown on GaAs substrates have photo response in the range of 1-1.3 eV and 1-1.2 eV revealed by low-temperature photoluminescence measurement [19].
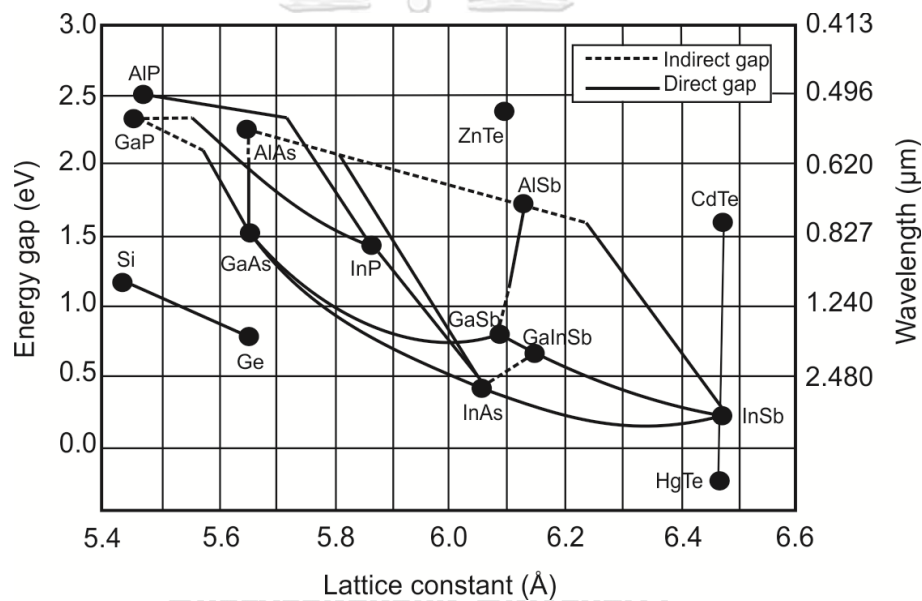
Figure 2.6 Composition and wavelength diagram of Sb-based III-V materieal systems
(Redrawan from Rogalski, A., 2006) [30].

2.5 Type-II Band Alignment

In a staggered type-II band alignment system, electrons or holes are localized within the QDs and keep the other outside, which leads to the reducing of electron-hole wavefunctions overlapping. This behavior is different from type-I band structure, in which both electrons and holes are confined in QD, and results in fast recombination rate. On the contrary, type-II band structure provides long carrier lifetime [31].

GaSb, InSb QDs embedded in a GaAs matrix are such type II system, where only holes are confined in QD because of large valence band offset between QD and GaAs, while electrons are loosely bound around the QD by the Coulomb attraction force. When the carrier density (number of electrons and holes) becomes larger at the interface induced by Coulomb interaction, band bending up occurs at the interfaces in the appearance of a triangle-well-like confinement potential for electrons around the QDs and consequently quantization energies increase. The relative energies of the electron and hole states (E1 and HH1) are shifted by the resultant electric potential as shown in Figure 2.7 (b). This can be defined as the band bending effect. The increasing of the excitation power creates the stronger band bending effect leading the shift of discrete energy levels of electrons at the interface of GaSb/GaAs heterostructure. Thus, a blue shift of the PL emission spectra occurs with increasing the excitation power. The blue shift is a fundamental property of type-II nanostructures which differ from type-I system [32- 35].

For the flat-band condition, the electron is almost spatially unconfined and thus the weak confinement is provided by electron-hole Coulomb interaction. Therefore, we can speculate that the quantized carrier (hole) density and hole occupancy are the important roles in the PL energy blue shift.

Type-I
Quantum Dot

Type-II
Quantum Dot

Type-II
Quantum Dot

(a)   (b)
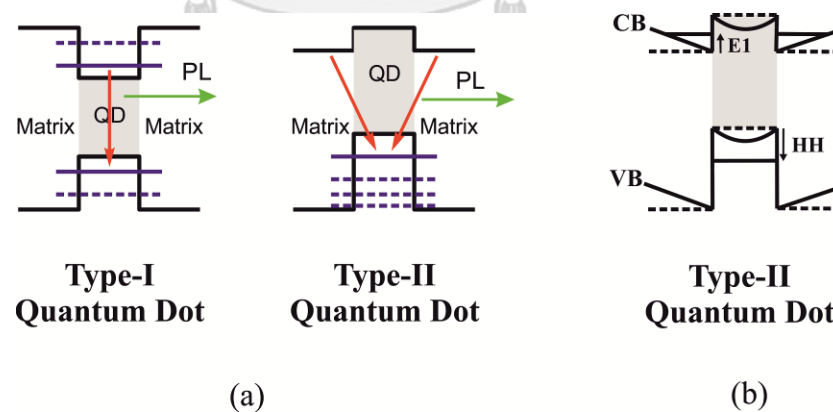
Figure 2.7 The schematic diagrams of (a) the comparison between type-I and type-II
band structures and, (b) band bending behaviour in type-II band structure.

2.6   Anti-Phase Domains (APDs) and Anti-Phase Domains Boundaries (APBs)

The integration of group III-V compound semiconductor on group IV elemental semiconductors example; Si and Ge, can create the devices with new functionalities by combining the properties of different materials to develop the optoelectronic and high speed electronic devices such as metal-oxide-semiconductor field-effect transistor (MOSFET) devices and enable the realization of non-classical, advanced complementary metal-oxide semiconductor (CMOS) devices. Lattice mismatch between GaAs and Ge ($< 0.1\%$) leads to the possibility of forming the defect-free heterostructure. As Ge is a relatively low-bandgap material, it offers low electron-hole pair creation energy. The successful growth of GaAs/Ge heterostructure gives potential for low cost high efficiency solar cells and longer wavelength photodetectors.   However, the formation of APDs is the challenge in this growth mechanism. During the growth of polar structure of GaAs on nonpolar Ge, two different face- centered-cubic (FCC) sublattice allocations occur, and depend on the type of atoms occupying the FCC sublattice. Due to opposite domain polarity rotated by 90º with respect to each other, it creates the anti-phase domain boundaries APBs between the APDs [36, 37]. In which regions, nonradiative recombination and mobility degradation due to carrier scattering can be occurred. Figure 2.8 shows the two possible sublattice locations of Ga and As atoms in GaAs grown on a Ge (110) substrate. The APD defect can be eliminated by utilizing miscut Ge substrates and/or controllable growth mechanisms.
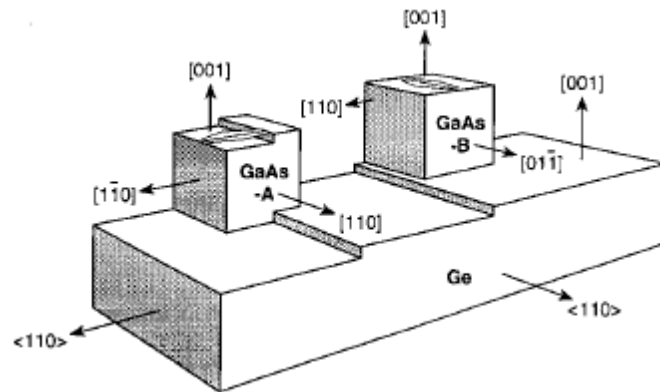
Figure 2.8 The two possible sublattice locations of Ga and As atoms in GaAs grown on a Ge (110) substrate. Here domain GaAs-A, with its $[1\bar{1}0]$ orientation perpendicular to the surface steps, corresponds to the case that the first atomic layer on the Ge surface is As, while GaAs-B, with its $[1\bar{1}0]$ orientation parallel with the surface steps, represents the situation that the first atomic layer on the Ge surface is Ga, based on the double step model of the Ge (001) surface and the simple layer-by-layer growth mechanism. The hexagonal figures on the GaAs (001) surfaces represent the shape of the molten KOH etch pits [23].

Chapter 3
Experimental Details

The experimental details of sample fabrication are explained in this chapter. The samples are fabricated by MBE, and the whole growth process is monitored by *in situ* reflection high energy electron diffraction (RHEED) pattern observation. The structural and optical properties of samples are characterized by *ex situ* atomic force microscopy (AFM), and photoluminescence (PL) spectroscopy.

3.1   Molecular Beam Epitaxy

All the samples in this work are fabricated by the solid source-MBE (RIBER, Compact 21 TM) equipped with antimony (Sb) valved cracker cell. The MBE system is composed of four chambers: load-lock chamber, buffer chamber, introduction/pre-heating chamber and growth chamber. High-purified group III and group V elements of gallium (Ga), indium (In), arsenic (As) and antimony (Sb) are mainly used in this work. All elements are contained in pyrolytic boron nitride (PBN) crucibles which are installed in separated standard effusion cells. While other effusion cells are heated by one heater in each, antimony cracker cell is heated by three independent heaters for reservoir, valve and cracker to produce the beam of Sb radicals; Sb_1, Sb_2 and Sb_4. The heaters' temperatures of all effusion cells and valved-cracker cell are controlled by feedback from standard thermocouples via computer. The growth chamber and effusion cells are cooled by liquid nitrogen (LN_2) to keep the ultra-high vacuum environment and to prevent chamber contamination and sequential impurities deposition onto the sample surface during growth. The beam equivalent pressure (BEP) and background pressure (BP) are measured by two separated ionization gauges situated behind the substrate heater and in front of the ion pump respectively. The ion pump and titanium sublimation pump are used to maintain the ultra-high vacuum growth chamber ($\leq 10^{-10}$ torr), and another ion pump is used to keep the pressure ($\leq 5 \times 10^{-8}$ torr) in the buffer chamber. The turbomolecular pump is used to be lower the load-lock chamber pressure ($\leq 3 \times 10^{-6}$ torr) before and after opening of the gate valve which connects the buffer and load-lock chambers. The nitrogen gas pipe is

equipped to the load-lock chamber for venting. A schematic drawing of MBE growth chamber accompanied by effusion cells is shown in Figure 3.1.

The growth rate calibrations of GaAs and InAs as a function of cell temperatures are deduced by utilizing the *in situ* RHEED intensity oscillation. All experiments are calibrated under As_4 flux of about 5×10^{-6} torr.
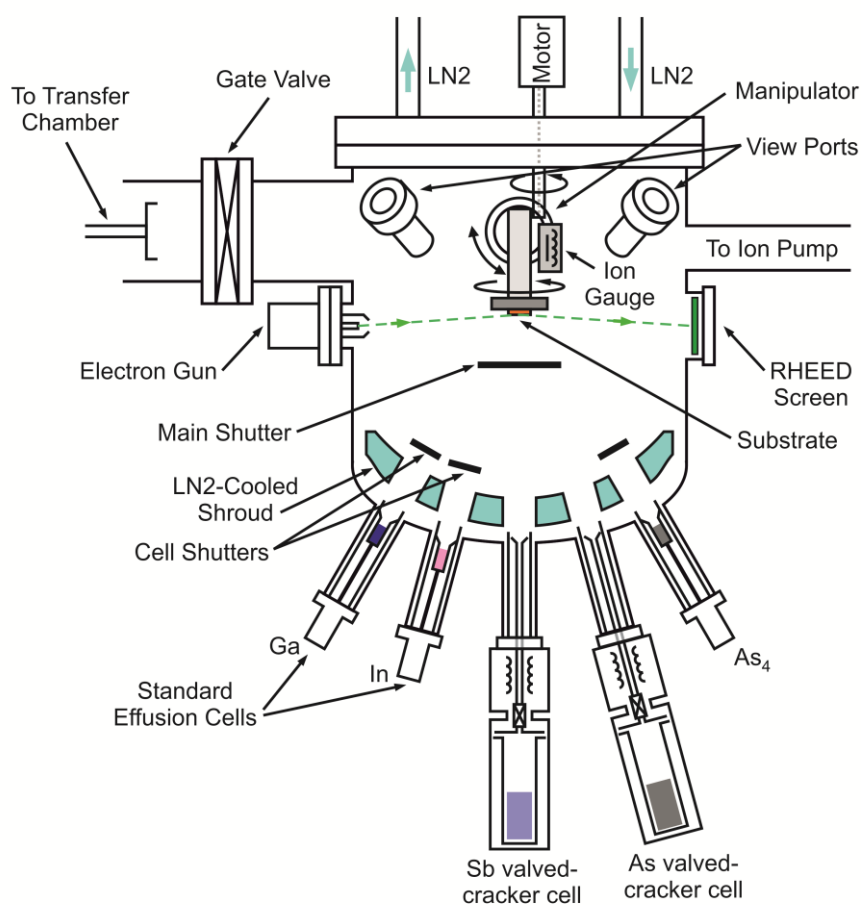
Figure 3.1   Schematic drawing of MBE growth chamber equipped by Sb and As valved-cracker cells.

The sample fabrication procedure is described as follows. $1.5 \times 1.5\text{-cm}^2$ piece of epi-ready semi-insulating p-typed (001)Ge substrate is cleaned by chemical etching method to remove the thick oxid layer on the surface. In this step, the substrate is dipped into hydrochloric acid (HCl) for a few second and cleaned by de-ionized water (DIW). Then the substrate is soaked by hydrogen peroxide (H_2O_2) and cleaned by DIW, alternatively. These steps are repeated for three times. After that the substrate is

dried under nitrogen gas and glued on 3" Si wafer by melted indium glue. Then the wafer was mounted onto the molybdenum block, and transferred into the introduction chamber for substrate preheating. The wafer with the substrate is preheated at 400ºC for 30 min in order to remove the contanminats and water vapour. After that the wafer is transferred into the growth chamber which keeps the background pressure $\sim 10^{-10}$ torr. Before growing any layers on the smaple surface, (001) Ge substrate is annealed at ~500ºC under the As_4 rich environment for removing surface oxide. After oxide removal, 250-nm GaAs buffer layer is grown with V/III ratio ~11 at 500ºC. The GaAs growth rate is kept at 0.51 monolayer/s (ML/s). During the growth, RHEED pattern is always observed. The (2×2)-to-$c(4\times 4)$ RHEED pattern transition is used to calibrate the actual surface temperature after 250 nm buffer layer growth. Then 250-nm GaAs layer is followed to flatten the surface. After the buffer layer growth, As cell temperature is decreased to reduce the As_4 amount in the growth chamber and to have an arsenic-free atmosphere for GaSb QD growth (which will be discussed in Chapter 5) and InSb QDs growth (which will be discussed in Chapter 7). The substrate temperature is also ramped down to desired QD growth temperature. Single layer of QDs is grown at various growth parameters for this dissertation. Note that 60-s Sb soaking is performed before opening desired QDs material shutter. For preserving QDs after the growth, the substrate temperature is reduced to about 50-100ºC lower than the QDs growth temperature. Then QDs are capped by 150-nm GaAs in two-step method; a few nm of capped layer at temperature lower than the QDs growth temperatuer and another capped layer at the same temperature of QD growth temperature. The lower temperature capping in the first step is the purpose of preventing QDs dissolving during capping. To investigate the surface morphology by AFM, the same QDs are grown on the GaAs surface with the same conditions. The amount of deposited QDs; GaSb (Chapter 5 and 6) and InSb (Chapter 7), the effects of growth rate and growth temperature are studied in this work. The schematic diagram of the sample structure is shown in Figure 3.2.
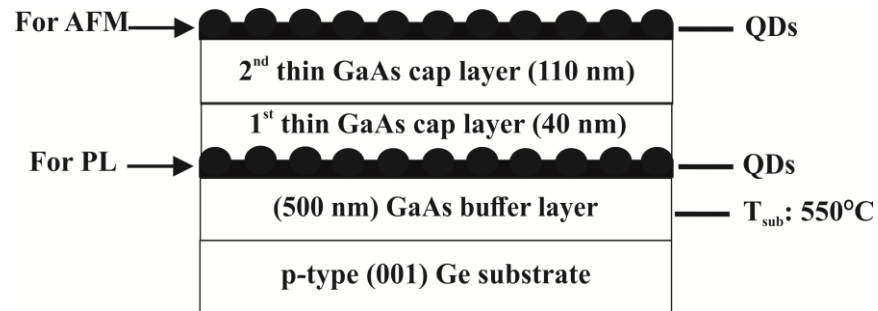
Figure 3.2   Schematic diagram of the sample structure grown in this work.

3.2   In-situ Reflection High-Energy Electron Diffraction (RHEED) Pattern Observation

RHEED technique is the most common *in-situ* monitoring tool for MBE growth to investigate the surface morphology of the sample and the proper growth conditions. The pre-growth conditions such as sample surface cleanness and optimum growth parameters (substrate temperature and growth rate) calibrations, and the MBE growth kinetics can be evaluated by RHEED patterns observation. The RHEED pattern is the reciprocal lattice representation of the sample surface, and which consists of streaky and spotty diffraction patterns corresponding to the smooth and rough surfaces. In a typical RHEED process, high energy (10-100 keV) electron beam is incident on the sample surface at a small angle ($\theta \sim < 5°$), and is diffracted by the uppermost atomic layer. The view of reciprocal space of two-dimensional sample surface in real space is represented by the reciprocal lattice space rods which are perpendicular to the surface. This can be explained by the application of Ewald sphere construction to the reciprocal lattice space rods, which is called Laue method. The imaging of RHEED patterns on the florescent screen occurs when Laue diffraction condition is satisfied, which corresponds to Bragg's law in the simple diffraction theory.

Laue diffraction condition [38]:

$$k_{in} - k_{diff} = G \qquad\qquad (3.1)$$

where k_{in} and $k_{in} - k_{diff} = G$ are the wavevectors of the incident and diffracted electrons, respectively, and G is the reciprocal lattice vector. Laue diffraction condition assumes $|k_{diff}| = |k_{in}|$, i.e., the elastic scattering condition k_{diff} must be a vector connecting the origin of k_{in} and a point on a Ewald sphere whose radius is $|k|$ (see Figure 3.3 (b)). The pattern observed on the screen by the 2D-smooth surface is the periodic array of lines (streaky pattern), and spotty pattern is observed from the diffraction of 3D islands or rough surface.

(a)

(b)

(c)
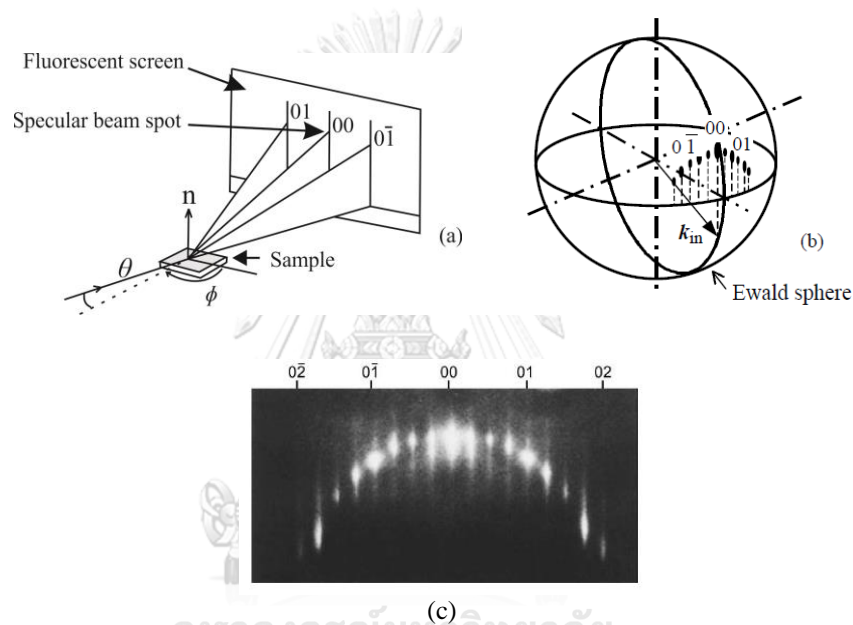
Figure 3.3   (a) Schematic representation of the RHEED observation system, and (b) Ewald sphere construction for a reconstructed surface [$\bar{1}10$] azimuth [39], and (c) RHEED pattern from the GaAs (001) 2×4 surface in the [$\bar{1}10$] azimuth; E = 12.5 keV, an incident angle of $\approx 3°$ [40].

3.2.1 RHEED pattern oscillation

In this work, the growth rate calibration and temperature calibration could be done by using RHEED pattern oscillations and RHEED pattern changing with temperature. In order to know the desired composition of related materials in QDs growth and buffer layer growth, the growth rates of GaAs and InAs are need to be

calibrated in this work. Moreover, the desorption rate InSb on GaAs are calibrated under Sb flux; ~5×10⁻⁷ torr, as the new attempt in this work.

3.2.2 Temperature calibration

Surface reconstruction transition by means of temperature gives the real surface temperature and which is used the reference temperature for the growth process. The calibration process is explained as follows. After the 250 nm GaAs buffer layer growth on (001) Ge substrate, the substrate temperature is decreased from the GaAs buffer layer growth temperature by 10ºC/min until RHEED pattern changes from (2×4) to c(4×4) patterns, and then substrate temperature is increased to appear (2×4) pattern again. For (001) GaAs surface, As-stabilized reconstruction pattern during the growth of GaAs under an excess of As is defined as (2×4) pattern, while Ga-stabilized is defined as (4×2) or c(4×4) pattern. In this work, the calibration process is performed under the As-rich atmosphere ~5-6×10⁻⁶ torr. The transition temperatures T_1, T_2, T_3 and T_4 are recorded in every steps and the average temperature; $(T_1+T_2+T_3+T_4)/4$, can be calculated, and which is equivalent to the real surface temperature of 500ºC. Figures 3.4 (a- d) show the schematic representations of the RHEED intensity interpretation of GaAs (001) with $\beta2$(2×4) surface reconstruction.

(a) Top view

→ [110]

↓ [1$\bar{1}$0]

● As   ○ Ga

(b) Side view

$\beta2$(2×4)

(c) [110] azimuth

$\bar{1}$0 00 10

(d) [1$\bar{1}$0] azimuth

0$\bar{1}$ 00 01
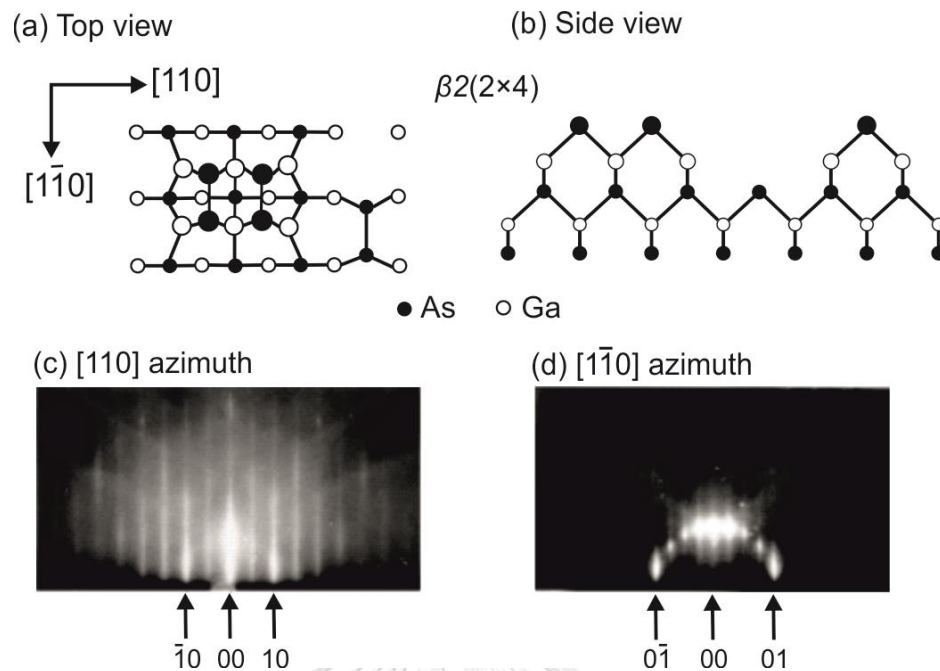
Figure 3.4 (a) Schematic representation of top view [41] and (b) side view of $\beta2$(2×4) GaAs (001) relaxed structure (Larger circles represent atoms closer to the surface.), and RHEED pattern of GaAs (001) 2×4 surface with the beam in (c) [110] and (d) [1$\bar{1}$0] azimuths [42].

3.2.3 Growth rate calibration

Figure 3.5 shows the real space representation of the formation of a single complete monolayer corresponding RHEED signal oscillation. $\bar{\theta}$ is the fractional layer coverage. The growth rate of GaAs and InAs can be calibrated by the observing and interpreting the RHEED pattern oscillations.

| MONOLAYER GROWTH | ELECTRON BEAM | RHEED SIGNAL |
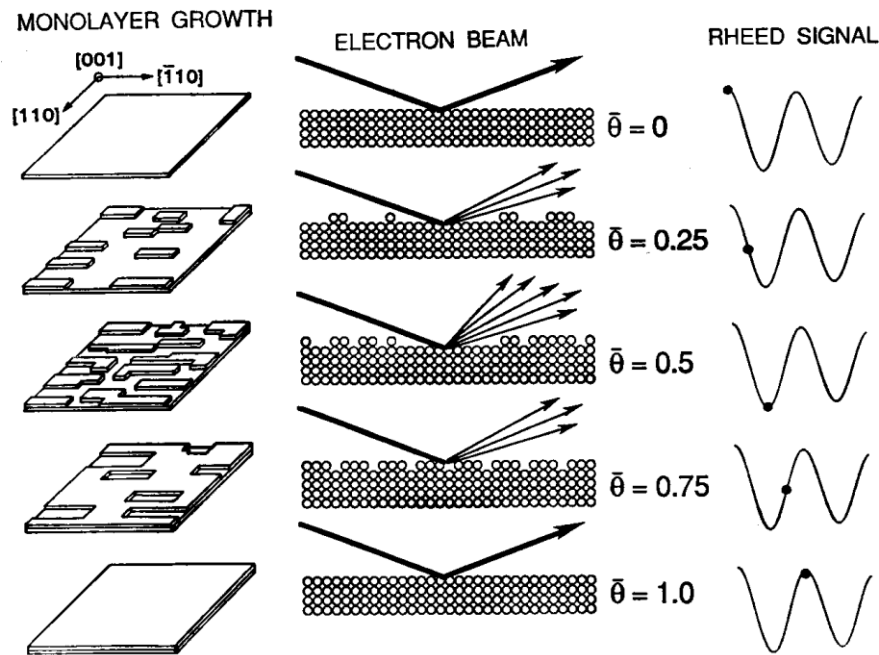
Figure 3.5   Schematic representation of the formation of a single complete mono-
layer corresponding RHEED oscillation signal [43].

The RHEED intensity corresponds to the surface roughness changes according to the fraction of the surface coverage as shown in the Figure 3.5. RHEED intensity shows the maximum value at the starting of the growth, and it decreases as the 2D layer-by-layer islands or surface step features on the growing surface increase. At the higher surface density of steps, RHEED oscillation shows the minimum value, and reaches again to the maximum after the growth of 1 ML.

The experimental data of GaAs and InAs growth rate calibrations as a function of cell temperatures are shown in Figure 3.6 (a) and (b). The growth rate of GaAs (r_{GaAs}) can be calculated from the number of oscillations (number of ML grown) divided by the time taken. For the growth rate of InAs (r_{InAs}) calibration, the time taken of RHEED transition from streaky (2D) to spotty (3D) pattern is recorded, and which shows the 1.7 ML InAs deposition [44]. The ratio of 1.7 to the time taken of the growth mode changing gives r_{InAs}.

The desorption rate of InSb under Sb-environment is affected by the substrate temperature, and which can be different from that of InAs under As-rich environment. To understand and investigate the effect of growth temperature on the growth of InSb,

RHEED intensity oscillation experiment is performed by varying substrate temperatures as shown in Figure 3.6 (c). In this case, the critical thickness of InSb/GaAs is assumed that constant 2 MLs. However, it can be different from the InAs/GaAs case, and it cannot be fully assumed that the critical thickness is a constant. Bennett *et al.*, 1996 and Bennett *et al.*, 1997 [2, 45] reported that the critical thickness of InSb/GaAs is about 1.5-2 ML at 400ºC growth temperature. InSb/GaAs cannot be grown at higher temperature because the low growth rate (~0.01 ML/s) is used in this experiment. Alternatively, the InSb growth rate r_{InSb} can be determined by

$$r_{InSb} = r_{InGaSb} - r_{GaSb} \qquad (3.2)$$

where r_{InGaSb} and r_{GaSb} are the growth rates of InGaSb and GaSb respectively.
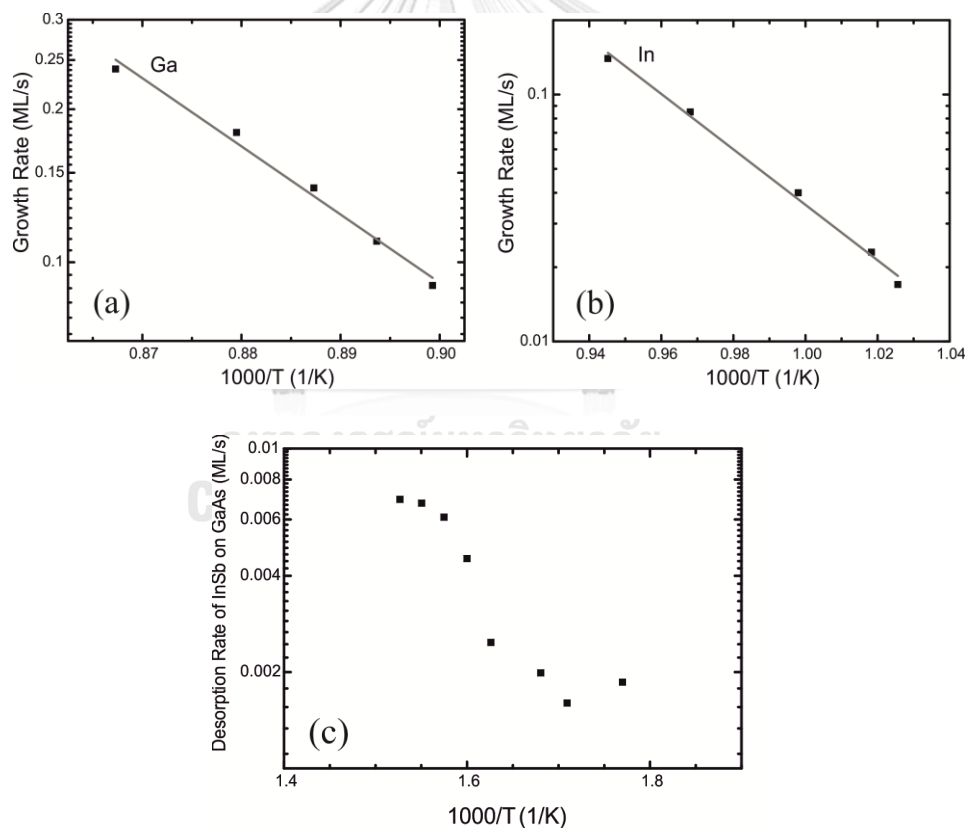

Figure 3.6   Plots showing the growth rates dependence of GaAs (a) and InAs (b) as a function of effusion cell temperatures, and the InSb desorption rate on GaAs by means of substrate temperatures (c). (Assume that the critical thickness of InSb/GaAs is 2 ML.)

3.3 Structural Characterization

3.3.1 Atomic force microscopy (AFM)

The surface morphology of all samples grown in this dissertation is characterized by using an AFM (Seiko SPA-400 AFM), which is operated in dynamic force mode in air. Sample surface areas of 2×2, 3×3 and 5×5 µm^2 are scanned according to the various sample surface morphology and nanostructures; QD size, shape and density. Slow scan speed (0.3 – 0.7 Hz) are used to achieve high image quality. AFM tip is Si with Al coating on the back side for high laser reflectance with tip radius of curvature of less than 8 nm, and high accuracy noncontact (HA_NC)/Au composite probe having the octahedral based cone shaped tip are used. The lateral resolution of AFM is ~4 nm by the 512 data points per scan line. The shape and lateral size of the QD structure can be larger than the actual QD structure due to the tip convolution.

3.3.2 Facet plot

To quantify the formulated QDs, the surface orientation mapping, which is so-called facet-plot was analysed [46]. In this dissertation, the plotted facet diagrams of self-assembled QDs are obtained by using the Matlab program. A brief discussion of surface orientation mapping is as follows. From any height profile, one can obtain the polar angle θ and the azimuth angle φ. These angles are used to plot the surface orientation mapping (or so-called facet plot). This is a kind of polar plot. In this plot, the θ is treated as the radial distance while the φ is treated as the polar angle. Each AFM surface pixel will be represented by a point (θ, φ) in the facet plot (see in Figure 3.7). Due to the statistical fluctuation nature of the AFM image, this plot is shown as a 2D histogram of surface orientation. An example of a real experimental data is shown in Figure 3.8. Note that a scale bar (0.5) is corresponding to an arctangent value of θ (26.6º).
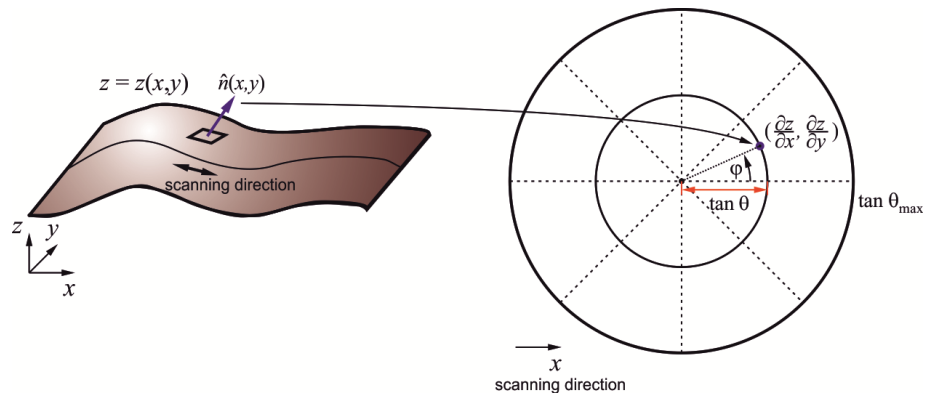
Figure 3.7 Illustration of the transformation from an AFM surface point to a point in a facet plot.
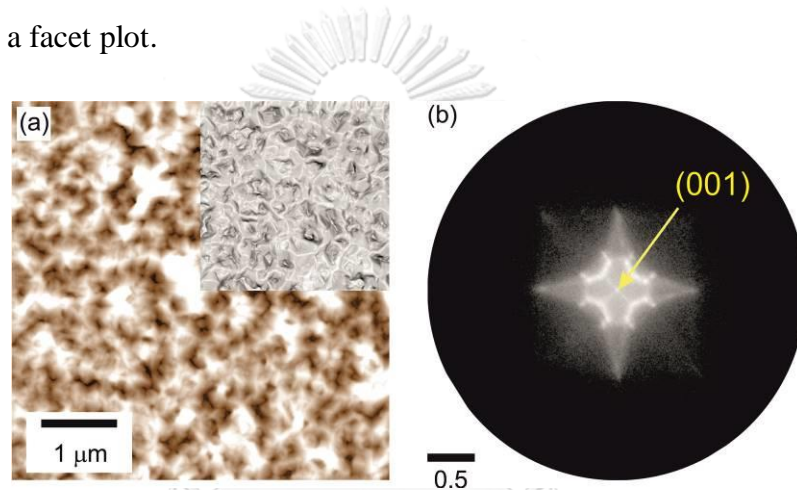
Figure 3.8 (a) Input AFM image of GaAs layer and (b) the corresponding facet plot [21].

3.4 Photoluminescence (PL) Spectroscopy

PL spectroscopy is the fundamental characterization technique to investigate the crystal quality, compositions, electronic states and optical properties of semiconductor nanostructure. PL emission can occur from the radiative recombination of generated electrons and holes occupied in the discrete energy density of states in the conduction band and valance band (in the case of semiconductor nanostructures), respectively. In our case, the sample is excited by higher laser energies ~ 2.3 & 2.4 eV (514.5 & 532 nm) than the GaAs bandgap (1.52 eV at low temperature). Thus electrons and holes are generated in the GaAs matrix surrounding the QDs firstly. Because of the special band structure of type-II QDs (GaSb/GaAs), only holes are

strongly confined within the QDs while the electrons are localized around the QDs by Coulomb attraction [47- 51].

In order to study the excitation power and temperature dependences of carrier dynamics, the power dependence PL and temperature dependence PL are carried out in this work. By increasing the excitation power, the number of photogenerated carriers increased, and the ground states and excited states PL emission can be observed at higher excitation power. The characteristic of type-II band alignment; the blue shift of PL energy as a function of cubic root of excitation power, can be investigated by power dependence PL. From the temperature dependent PL, the thermalization process where the carriers in GaSb/GaAs QDs escape to the GaAs barriers in type-II system is studied, and the activation energy can be extracted.

The full-width-at-half-maximum (FWHM) or PL linewidth is related with the QD size distribution. The better homogeneity and less number of QD array give the narrower PL linewidth and stronger PL peak intensity [52, 53]. The eigenspectrum of a single QD represents the discrete set of eigenenergies due to full quantization in all three dimensions. It can be considered only ground-state transitions if the quantization effects are so high, and thus the recombination spectrum R_N of N QDs can be described as;

$$R_N(h\nu) = \sum_{n=1}^{N} S(h\nu - E_n) \qquad (3.3)$$

where $S(E)$ is the Lorentzian broadening of finite width Γ. However, it still needs to take account other factors such as variations of strain or shape of QD and size fluctuation of QD because self-assembled QD array exhibits the large number of QDs with high size fluctuation. Therefore the recombination spectrum of the dot ensemble R_∞ by the convolution of the single QD spectrum with the distribution function can be expressed as

$$R_\infty(h\nu) = \int S(h\nu - E) P(E) dE \sim P(h\nu) \qquad (3.4)$$

where $P(E)$ is the statistical distribution of the eigenenergies corresponds to the spectral width [54] . In this work, the PL of QDs obtained under various growth conditions based on QD size, shape and material compositions will be studied and discussed.

3.4.1 Optical setup

In this work, two PL systems are used for sample characterization as shown in Figure 3.9 (a) and (b). LN_2 cooled InGaAs detector is used in both systems. Ar^+ laser and diode-pumped solid state laser (DPSSL) having wavelength 514.5 nm and 532 nm are used as the excitation laser sources in two PL systems, respectively. The laser spot size is a few hundred of micron in both systems. In the first PL system (Figure 3.9 (a)), the standard lock-in technique is used to detect the frequency of signals which have been sent by the chopper controller and the detector. The optical beam chopper sends the reference signal (square wave with the frequency that the beam is being chopped) and the detector sends the specific wavelength signal diffracted by the diffraction grating to the lock-in amplifier.

In the case of the InGaAs photo-detector array (PDA) of the second PL system (Figure 3.9 (b)), the background is acquired and saved by using the identical experiment settings while the experiment signal source remains off. Then the experiment signal is acquired, and the background subtraction is performed to remove the ambient signal and the dark current component of the signal data. The laser excitation power is controlled by placing neutral density filters (NDF) in front of the laser, and heat absorbing filter (HAF) is placed consecutively for the purpose of absorbing heat or UV from laser light for experiment. Between the two objective lenses; L6 and L7, IR transmitting filter (IR-83) having transition wavelength 830±10- nm is inserted to emphasize the signal wavelength higher than 800 nm and to block other stray light entering the spectrometer. A 100-mm focal length and 150-mm focal length lenses (L6 and L7) are used to collect the PL signal. In this PL setup, 0.3-m focal length triple grating imaging monocromator (Acton SpectraPro-300i) can provide three gratings with groove densities; 300 mm^{-1}, 600 mm^{-1} and 1200 mm^{-1}, respectively. In this work, the measurement set at the grating with groove densities 600 mm^{-1}. The mechanical entrance slit shutter is mounted to the spectrometer and connected to the detector controller to be able to control the exposure time.

To measure the low-temperature PL and the temperature dependence PL, samples are mounted into helium cooled cryostats.

(a)

(b)
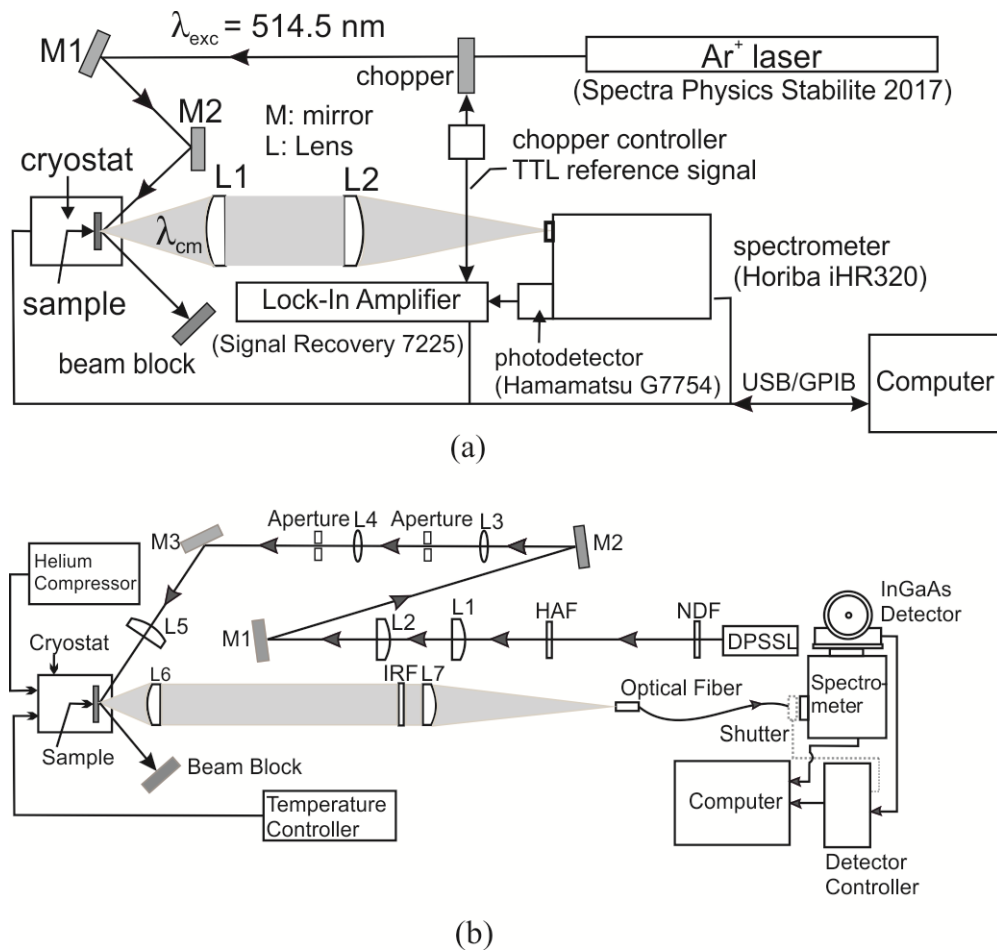
Figure 3.9   Schematic   diagrams   of   the   experimental   PL   systems   at
(a) Semiconductor Device Research Laboratory, Department of
Electrical Engineering, Chulalongkorn University, Thailand, and
(b) Aralab, Nano Quine, Institute of Industrial Science, The University
of Tokyo, Japan.

3.5   Raman Scattering Spectroscopy

In this work, Raman spectroscopy is used as the quantitative characterization
tool for obtaining the detailed information about the self-assembled nanostructures
such as strain at the interfaces; between buffer layer and QDs, and between QDs and
capped layer etc. The vibrational properties of QDs due to strain effects between the
QDs and matrix layer can be characterized by Raman spectroscopy.

The reflecting, absorbing and scattering of light can take place when a sample
is irradiated with an intense monochromatic light source (usually a laser). When the

incident light encounters the sample, the photon interacts with the molecules and can scatter from it. Most of the scattered light is the same wavelength as the incident light source, and which can be defined as the elastic scattering or Rayleigh scattering (see Figure 3.10). A small amount of light is scattered at different wavelengths, and it is called inelastic or Raman scattering (see Figure 3.10). In Raman spectroscopy, frequency (ν) or wavenumber is often used to discuss about the interaction of radiation with the states of molecule in terms of energy. According to the frequency of the light source (laser) used, the induced polarized condition called virtual state is created.

At the time of interaction, a photon with energy $h\nu_0$ is absorbed by the Raman-active molecule, which is promoted to the virtual states. In relaxation process, there are three types of scatterings can be occurred. Relaxation from the virtual states to the initial ground state is predominantly occurred in Rayleigh scattering. But relaxation to the first excited vibrational state by transferring part of photon energy to the Raman-active mode or molecule with the frequency ν_m results the decreasing of frequency of scattered photon to ν_0-ν_m, which is called Stokes scattering. In anti-Stokes scattering, the frequency of scattered photon is higher than the initial frequency, and thus it indicates that the Raman-active molecule or the system has already to be in excited state before, and transferred energy to the scattered photon.

Therefore, Raman scattering measures the energy difference between the ground state and excited state by subtracting the energy of scattered photon from that of the incident photon energy as follows:

$$E_{Raman\,shift} = hc/\lambda_{laser} - hc/\lambda_{Raman} \tag{3.5}$$

In this work, Raman spectroscopy is carried out by using room temperature (RT) Invia Reflex Confocal Raman spectrometer with 532-nm laser. The system set up is shown in Figure 3.11.
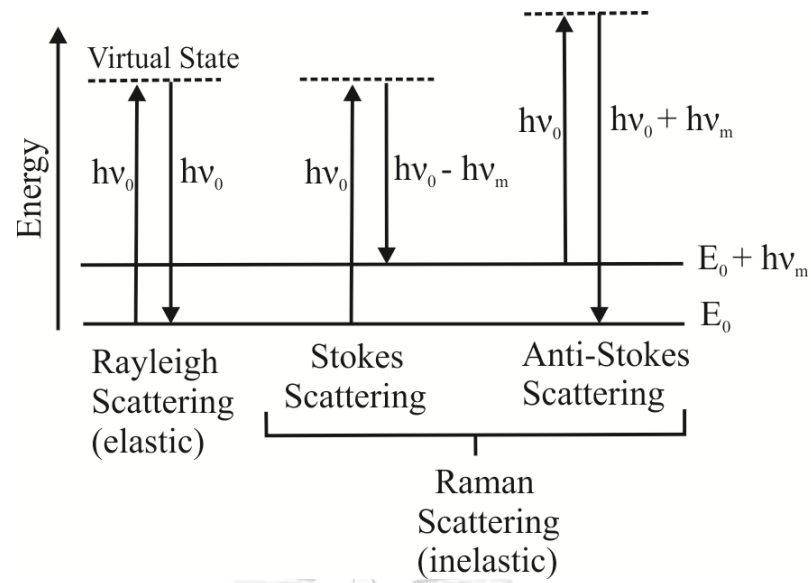
Figure 3.10   Band diagram representing the quantum energy transition for Rayleigh
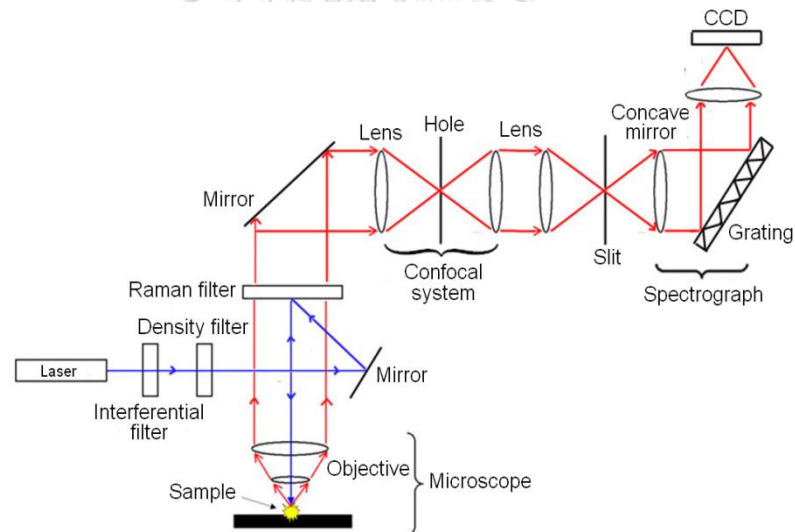   and Raman scatterings.

Figure 3.11   Schematic view of the experimental arrangement for Raman
             spectroscopy.

Chapter 4
GaAs Matrix Layer Growth on (001) Ge Substrate

In this chapter, the epitaxial growth of GaAs buffer layer on (001) Ge substrate and the improvement of GaAs surface quality decorated with APDs are presented. The effects of V/III ratio and growth temperature on APD formation are investigated by using (001) Ge substrate. The detailed growth process is controlled by observing RHEED patterns. The applicable growth conditions to improve GaAs layer quality can be considered by the combination of *in situ* and *ex situ* measurements; RHEED and AFM.

4.1 Experimental Details

The formation of APD is mainly affected by the growth temperature, V/III ratio and the substrate misorientation angle. In the past, the growth of GaAs on Ge has been investigated in several growth techniques [55-57]. The MOCVD growth by using a few degree (typically 6º) miscut (001) Ge substrate is the possible solution for defect-free GaAs layer with completely free APDs (single GaAs domain) [58, 59]. In MBE, the physical evaporation of As_4 is not self-terminating at low temperature which results in the multiple As monolayers coverage on the Ge surface and induces the APD formation. A few nanometers prior growth of epitaxial Ge layer on the Ge substrate before GaAs layer, and the migration enhanced epitaxy (MEE) technique to carefully control the initial GaAs nucleation condition are the probably solutions for the APD free or nearly free GaAs growth [60, 61]. In MEE growth, a few nanometers of GaAs layer is initially grown by applying Ga and As beams alternatively at low temperature, which is contradictory to the standard GaAs MBE growth.

In this work, 500 nm thick GaAs buffer layer is directly grown on conventional (001) Ge substrate at 550ºC. Before the buffer layer growth, 10 min substrate annealing is carried out at 570°C under As_4 rich atmosphere for surface oxide desorption. As_4 flux is adjusted according to the target beam flux V/III ratio (As_4/Ga) of following buffer layer growth. The variation ranges of V/III ratio are limited at 10, 13 and 15, and the growth temperature is limited to 350ºC and 550°C respectively. In the V/III ratio dependence growth, As_4 beam flux is variable and Ga

growth rate is fixed at 0.5 ML/s. As is self-terminating on Ge at temperature of 350ºC and higher, and which makes the possible growth of GaAs layer with low APD density on Ge in this work. The surface quality is improved and APD density is reduced by careful control of growth conditions (As_4 pressure and growth temperature).

4.2 Flat Surface Quality Improvement: *In Situ* and *Ex Situ* Observation by RHEED and AFM

Figure 4.1 (a) shows the 2×2 μm^2 AFM images of GaAs buffer layer growth on Ge substrate at various growth conditions (referred as samples A, B, C and D). Sample A and B are grown in V/III ratio ~15 and 13 at 550°C. Sample C and D are grown at same V/III ratio ~10 at different growth temperatures; 400°C and 550°C respectively. The distinct transition of APD condition is displayed in AFM images of sample A to D. To investigate the surface roughness because of APDs formation in each sample, the AFM cross-sectional line profiles are extracted as shown in Figure 4.1 (b). The line data are extracted from the upper left corner to the lower right corner of the 2×2 μm^2 AFM results showing in Figure 4.1 (a).

The surface roughness can be described by measuring the root mean square (RMS) value. The RMS values are extracted by Gwyddion software. The RMS of samples A, B, C and D are 2.7 nm, 2.4 nm, 1.1 nm and 0.5 nm respectively for 500 nm thick GaAs layer. It can be clearly seen that the surface roughness of sample A and B are larger than those of sample C and D, and sample D has the lowest RMS value of surface roughness. It shows that in the direct growth of GaAs on Ge, the GaAs nucleation as the function of As_4 flux is important to control carefully in order to reduce APD density.

In samples A and B, the APD density is very high, and which can be attributed to the As_4 contamination during the growth and after the growth without Ga beam. In detailed growth procedure, when the target thickness of GaAs is reached, Ga cell shutter is closed and As cell still remains opening. Then As cell temperature and growth temperature is ramp down under 200ºC in As cell and to the target QD growth temperature in MBE substrate manipulator. After the prolonged buffer layer growth, the amount of As_4 in the growth chamber is very high, and it takes long time to reduce

the As$_4$ amount or pressure in the chamber. If the sample substrate temperature is decreased abruptly within high As$_4$ pressure condition, As accumulation on the surface and As contamination can occurred. On the other hand, the annealing effect after growth can improve the surface quality under As$_4$ exposure. This can be clearly seen in real time RHEED patterns observation. When the V/III ratio is reduced to ~10, the surface quality improves significantly as shown in Figure 4.1 (a) sample C and D. The surface roughness is decreased to RMS roughness ~1.1 nm in sample C and 0.5 nm in sample D. Sample C has higher surface roughness than sample D, and this is because sample C is grown at low temperature at 350ºC and sample D is grown at higher temperature 550ºC. Although the low temperature and smaller V/III growth can improve the APD condition, the individual APD does not grow enough to connect completely with the adjacent APD, and which create the rough surface with small APD surface area. It can be suggested that the higher growth temperature can improve the APD formation.

As shown in Figure 4.1 (a), the nearly flat APD formation with APBs is occurred in samples C and D. The average domain size of sample D is smaller than that of sample C but the overall areal surface is smoother with narrower APBs. In the closer look at the AFM images, the small lines due to the wavy surface in each domain can be seen and it can be assumed that the favourable domain orientation corresponding to the substrate direction. Based on the AFM observation, the GaAs APDs on Ge are rotated 90ºC with respect to each other, and which is the proof of the two sublattice orientations in growing polar semiconductor (GaAs) on non-polar element (Ge).
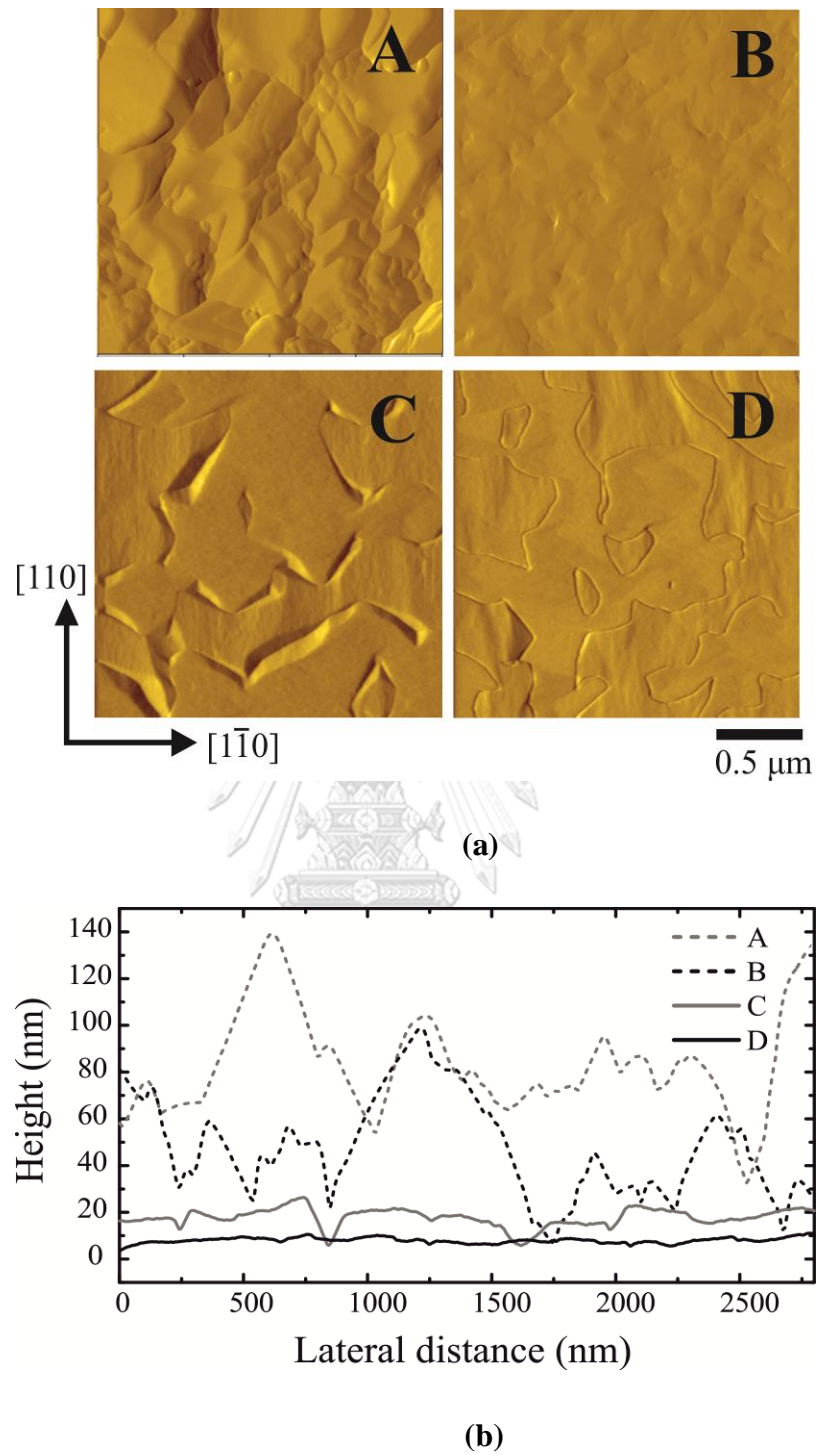
Figure 4.1 (a) 2×2 μm^2 AFM images of GaAs buffer layer grown on Ge with V/III ratio ~15 (sample A), 13 (sample B) at 550ºC, and with V/III ratio ~10 at 350ºC (sample C) and 550ºC (sample D). (b) Cross-sectional line profiles of samples A-D.

Figure 4.2 shows the RHEED patterns along the [110] and [100] azimuths corresponding to different surface conditions within GaAs buffer layer growth. At the de-oxidation process of Ge substrate annealing at 570ºC, the bright streaky RHEED pattern can be seen as shown in Figure 4.2 (a). The bright streaky pattern appears when the substrate temperature reaches around 550ºC, which shows that the substrate is completely de-oxidized, and ready to grow the GaAs layer. Since the As cell is already opened and the pressure is adjusted as the target V/III ratio during oxide desorption process, Ga cell shutter is opened to initiate the GaAs nucleation. As soon as the Ga cell shutter is opened, the streaky RHEED pattern transforms to spotty pattern as shown in Figure 4.2 (b). This is because of the rough surface of GaAs nucleation on Ge surface. After ~120 s (about 20 nm thick layer growth), the spotty RHEED pattern starts to elongate. This observation implies that the GaAs starts to cover the entire Ge surface. In this way, the GaAs nucleation process is monitored by the real time RHEED pattern observation. The complete streaky RHEED pattern shown in Figure 4.2 (c) indicates that the $c(4\times4)$ GaAs surface reconstruction. These streaky RHEED pattern can be seen in the cases of samples C and D. For samples A and B, the dark and partially spotty RHEED pattern (Figure 4.2(d)) is observed instead of streaky RHEED pattern. This is because of the surface roughness.
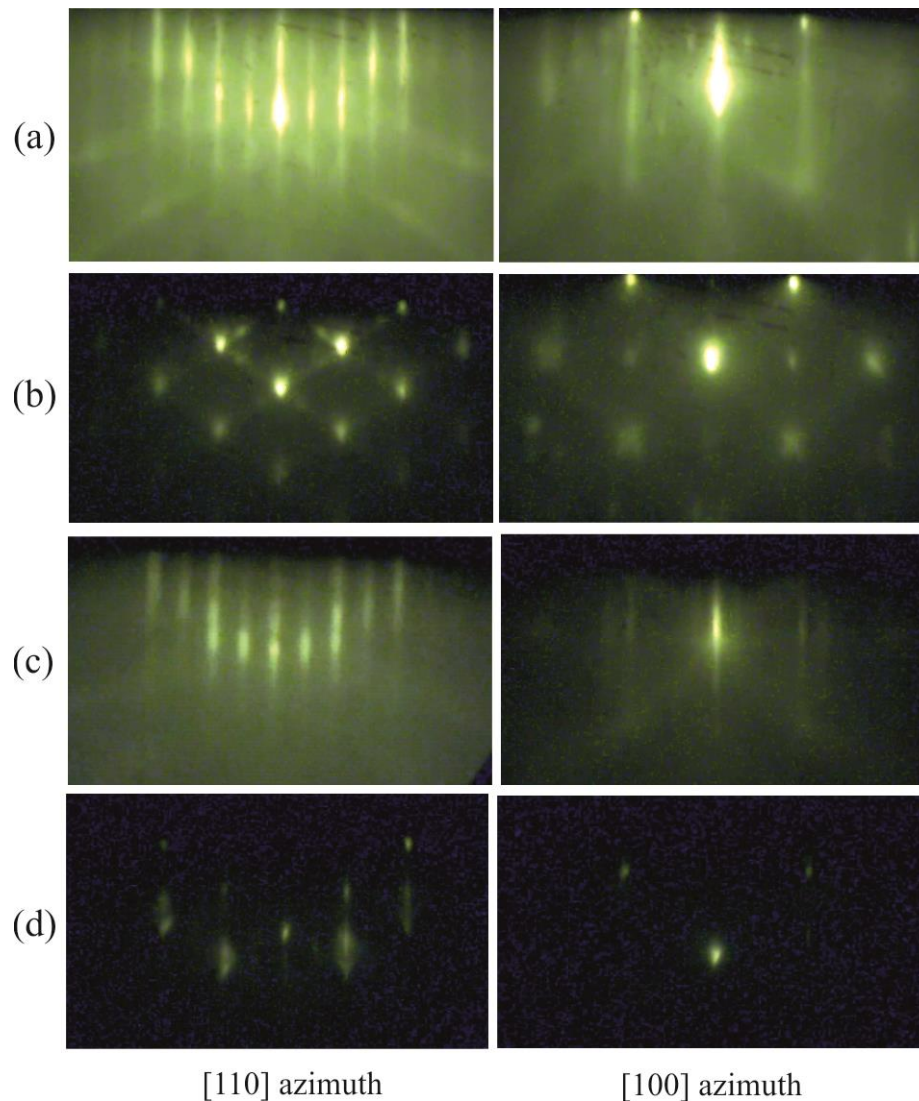
Figure 4.2 RHEED patterns along [110] and [100] azimuths: (a) during the oxide desorption process, (b) 20 s after Ga deposition, (c) $c(4\times4)$ surface reconstruction of GaAs layer, and (d) spotty RHEED pattern from the rough surface.

This chapter can be concluded that the low V/III ratio ~10 with careful controlling As_4 flux and the high growth temperature are needed for good GaAs nucleation with moderate buffer layer thickness. The result of nearly flat APD formation allows us to realize the subsequent nanostructure QDs growth on the buffer layer. In this work, the resultant APD condition is acceptable for the QD nanostructure growth and the effects of the nature of APDs and APBs on the QD formation will be studied and discussed in next chapters.

Chapter 5
Self-Assembled GaSb/GaAs Quantum Dots

GaSb/GaAs QDs are grown on (001) Ge substrate and their structural and optical properties are investigated by using AFM and PL in this chapter. The effect of GaAs matrix layer segmented to APDs on the morphology of QDs is also studied. Raman spectroscopy is carried out to study the strain induced effect due to the present of buried GaSb/GaAs QD layer.

5.1   Experimental Details

(001) Ge substrate is annealed at ~500ºC under the As_4 rich environment for removing surface oxide [62]. After the surface oxide desorption, 500-nm GaAs buffer layer is grown with V/III ratio ~13 at 500ºC. The Ga growth rate is kept at 0.51 ML/s. RHEED pattern observaion is performed during the growth. The surface temperature is calculated by extracting the (2×2)-to-$c(4\times4)$ surface reconstruction RHEED transition [63]. Then the growth temperature is decreased to 450ºC for QDs growth and As cell temperature is decreased to reduce the As_4 amount in the growth chamber. Ga growth rate is reduced to 0.14 ML/s for GaSb QDs growth, and V/III (Sb/Ga) ratio is ~4. GaSb/GaAs QDs are grown ~3 ML QDs thickness after performing of Sb soaking for 60 s. GaSb/GaAs QDs are capped by 150-nm GaAs by two step-growth method. In order to prevent the QD dissolving during capping [64], QDs are capped by a few nanometer ~40 nm GaAs layer at low temperature 400ºC followed by ~110 nm GaAs layer at higher temperature 450ºC. 2 ML GaSb/GaAs QDs are grown on the top layer to investigate the surface morphology.

The fabricated sample structure of GaSb/GaAs QDs grown on (001) Ge substrate is shown in Figure 5.1.
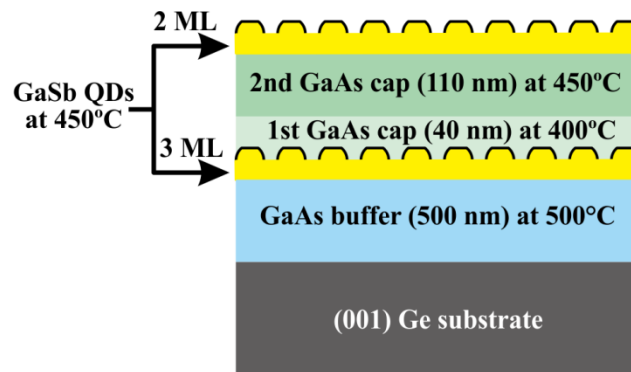
Figure 5.1 Schematic sample structure of type-II GaSb/GaAs QDs on (001) Ge substrate [24].

5.2 Statistical Analysis of GaSb/GaAs QD by AFM

Although there is the low lattice mismatch between GaAs and Ge (<0.1%), the growth of III-V polar (GaAs) on IV nonpolar (Ge) materials creates the formation of APD. Figure 5.2 (a) shows the formation of GaSb/GaAs QDs on the APDs and in the APBs as 3D AFM image. The surface morphology of GaAs APD segmented by anti-phase domain boundary (APB) can also be seen in the Figure 5.2 (a). The growing of GaAs on Ge arises the formation of APDs in two different phase orientations: As-As bond and Ga-Ga bond (90° rotated by each other) [56, 60]. APBs act as the non-radiative recombination centers. Therefore, by adjusting the growth conditions of GaAs buffer layer for flat and enlarging the size of APDs, the density of APBs can be reduced. As shown in Figure 5.2 (b), high density QDs can be deposited in the flat APD and low density QDs can be deposited along the APBs. The circular based-shape QDs are observed. Figures 5.2 (c, d) show the line profiles of GaSb/GaAs QDs on APDs and in APBs. The line profiles are extracted from the AFM result, and which are drawn perpendicular to the APBs. APB has the non-uniform depth in the range of 5-20 nm and the width of ~100 nm. The lines (i-iii) are drawn across three successive GaSb/GaAs QDs which are deposited in the APBs and the nearby QDs formulated on the APDs as shown in Figure 5.2 (c, d).
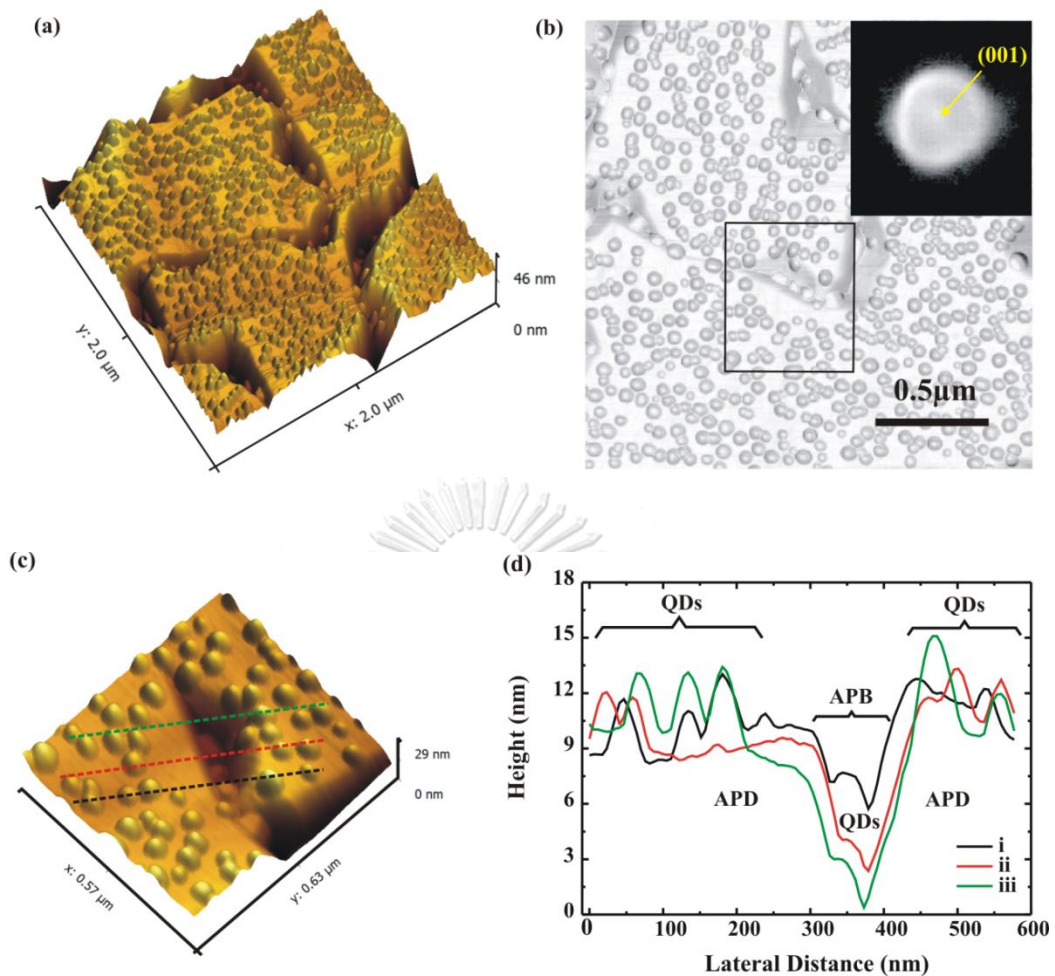
Figure 5.2 (a) 2×2 μm^2 3D AFM image with 2 ML GaSb QDs layer on (001) Ge substrate. (b) 2×2 μm^2 2D AFM image in surface slope scale of (a). Upper right inset shows the facet plot of QD surface. The rectangle box marks an area of anti-phase domain boundaries (APB) and anti-phase domains (APDs) with the QDs. (c) 3D AFM image of the area in rectangle box of (b). (d) Line profiles of the QDs (i–iii) formed in both APB and APDs [24].

The histograms of QD diameter and height on APDs and in APBs are plotted by extracting the AFM data of QDs as shown in Figures 5.3 (a-d). Gaussian function is used to fit the data of histograms. The average value of dots height (diameters) and density on APDs are 4.47 ± 1.27 nm (48.8 ± 14.1 nm) and ~ 1.57×10^{10} cm^{-2}, and that in APBs are 4.38 ± 2.23 nm (82.1 ± 13.6 nm) and ~ 9.5×10^8 cm^{-2}, respectively. It can

be speculated that the deposited GaSb/GaAs QDs on APDs and in APBs give the same emission, although they have different QDs size distribution. Kunrugsa *et al.* have reported that GaSb/GaAs QDs in higher density of 1.9×10^{10} cm^{-2} could be deposited [36]. In this work, the QD density is lower than the reported value and this is due to the larger size of APBs and smaller area of flat APD surface, and the different growth conditions.
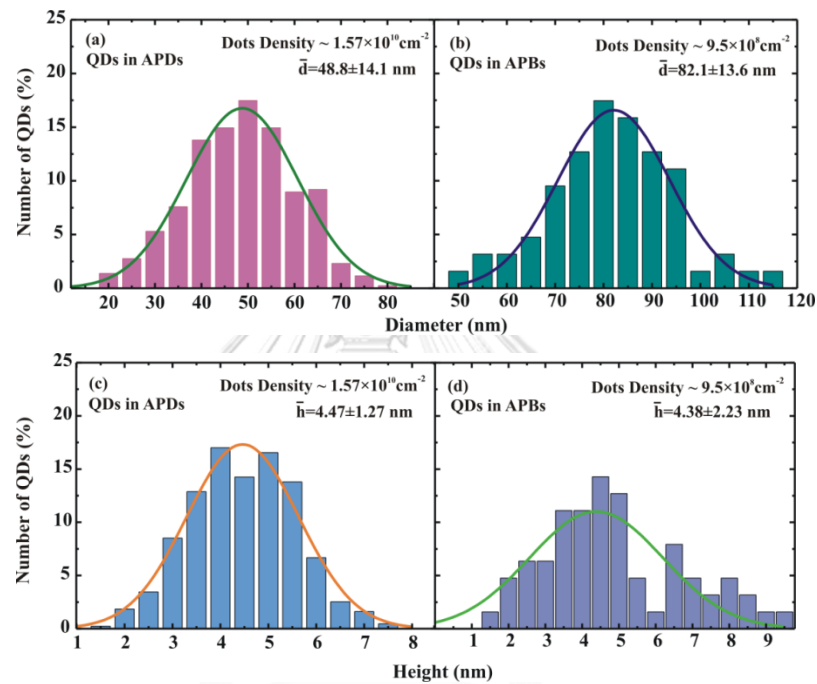

Figure 5.3 (a-d) Histograms show distributions of GaSb QDs by comparing diameters and height of QDs between APDs and along APBs. Solid lines are Gaussian fits. Dot density, mean and standard deviation of height and diameter values are shown [24].

5.3   Raman Scattering Analysis

Raman scattering analysis is carried out to investigate the strain effect originated from GaSb/GaAs QD layer. The free standing QDs or buried QDs produce the strain influence to the surrounding GaAs layers. Figures 5.4 (a, b) show the Raman spectra of the sample with GaSb/GaAs QDs and the sample without QDs. These spectra mainly exhibit the optical phonon scattering of (TO) transverse optical phonon and (LO) longitudinal optical phonon modes of GaAs. By using the Gaussian function fitting, the TO and LO peak positions can be quantified as shown in Figure 5.4 (b). For the sample without QDs, the fitted TO and LO peak positions are 267.8 cm^{-1} and 290.6 cm^{-1}. With GaSb QDs, The TO and LO GaAs peaks show the red shift of to 266.2 cm^{-1} and 289.9 cm^{-1} by 1.6 cm^{-1} and 0.7 cm^{-1}. We can attribute the peak shift to the strain effect of tensile strain in GaAs layers because of the presence of compressively strained GaSb QDs [65].
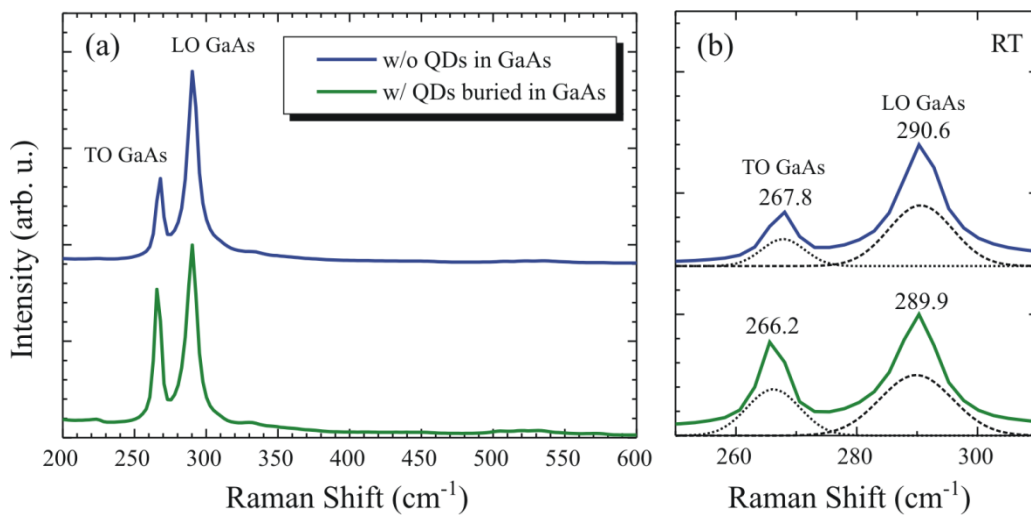
Figure 5.4 (a) Normalized Raman spectra measured from the epitaxial GaAs samples without and with buried GaSb QDs and (b) Raman spectra described the redshift of TO and LO GaAs peaks due to the presence of GaSb QD layer. The dash and dotted lines are from Gaussian fits (shown with a division by one half) [24].

5.4   Optical Characterization of GaSb/GaAs QD

The optical properties of GaSb/GaAs QDs grown on (001) Ge substrate is carried out by the photoluminescence PL measurement. Figure 5.5 (a) shows the power-dependent PL spectra at low temperatures 20 K and 30 K. The two peaks from GaSb QDs and GaAs layer are observed. The peak emitted in energy range of 1.0-1.3 eV can be attributed to the GaSb QDs and that of 1.36-1.57 eV is from GaAs layer. Because of the lower bandgap energy of GaSb QDs than that of the GaAs, GaSb can response at longer wavelength or lower energy. But compare with the photo response of GaSb bulk, the emission from GaSb QDs has higher energy, and this is due to the Sb-for-As and/or As-for-Sb intermixing at the interfaces between GaSb QDs and neighboring GaAs layers. [53, 66]. In this work, the WL peak is not observed. It can be speculated that the WL peak incorporates into the QDs peak resulting the broad QD peak. The deposited WL thickness affects the WL peak position, and thus the peak position of WL can shift to the lower energy by increasing the WL thickness [67]. The related investigation and discussion on the combined peak of QD and WL are shown below.
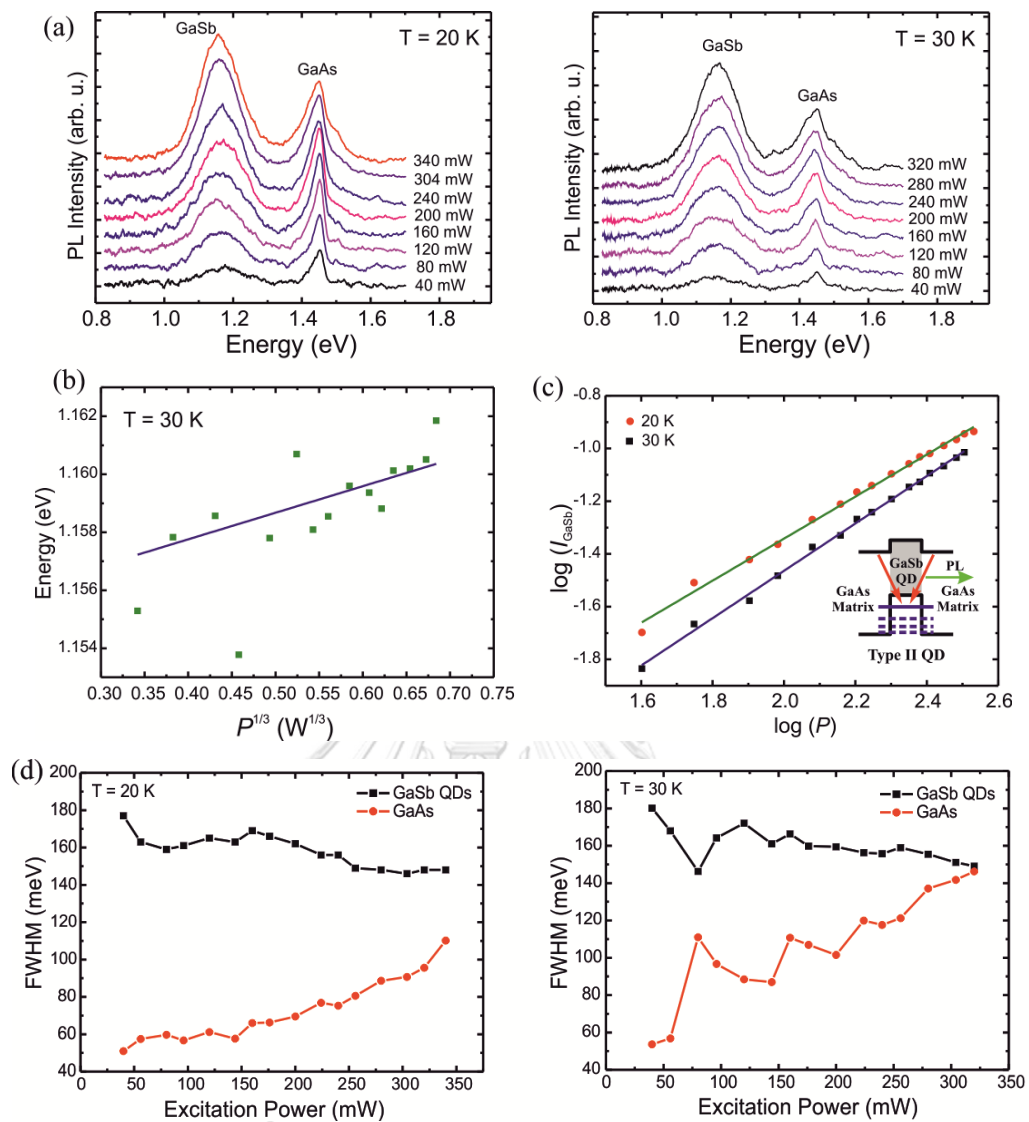
Figure 5.5 (a) Power-dependent PL spectra at different temperatures (20 K and 30 K) obtained from GaSb/GaAs QDs on (001) Ge substrate. (b) The shift of the PL peaks energy as the third root of the excitation power at 30 K. Solid line is a linear fit. (c) The comparison of the integrated peak intensity of GaSb QDs versus laser excitation power in log-log scale between PL obtained at 20 K and 30 K. The inset is the band diagram demonstrating radiative recombination in type-II GaSb/GaAs QD. Solid line is a linear fit. (d) The comparison of full-width at half maximum (FWHM) between GaSb QDs and GaAs as a function of laser excitation power at 20 K and 30 K respectively [24].

The PL spectra observed at 20 K show the broad QD peak and the sharp GaAs peak. The QD peak slightly shifts to both higher and lower energies by increasing the laser excitation power. However, the difference of PL peaks at lowest and highest excitation power (40 mW and 340 mW) is about 12 meV, and the peak shifts to lower energy by increasing excitation power. This can be explained by the combination of WL and the QD peak. The higher peak emission energy at low excitation power is mainly from the WL, and the peak emission from QD is more efficient at higher excitation power. Apart of two lower spectra, QD peak energy is almost the same at 1.16 eV. At higher excitation power of 224 to 340 mW, the intensity of GaSb QD peak is higher than that of GaAs peak. This can be attributed to the more efficient radiative recombination in QD than that in GaAs at higher excitation power. When the power dependent PL is performed at 30 K, the PL peak energy slightly shifts to higher energies by increasing the excitation power. This is the characteristic of GaSb/GaAs type II band alignment. This is because of the becoming weak and convolution of WL peak into the broad QD peak at higher temperature result the more efficient of QD peak [16]. By increasing the laser power from 40 mW to 320 mW, the QD peak shift to higher energy (blueshift) of about 6.6 meV. As shown in Figure 5.5(b), the peak energy slightly shifts to both higher and lower energies at low excitation laser powers. This could be attributed to the broad QD peak with the combination of WL peaks, and the QD peak from the combined peaks of QDs and WL cannot be extracted. The average hole localization energy, i.e., energy difference between QD and GaAs peaks, which can be defined as average hole localization energy of about 260 meV and 277 meV at 20 K and 30 K PL measuring temperature are observed. The large hole localization energy gives the possibility to use this QD as a cell in memory devices [36].

The rate of hole transferring from the GaAs cap and WL to GaSb QDs can be studied by the integrated QD peak intensity as the function of excitation laser power as shown in Figure 5.5 (c). It can be seen in Figure 5.5 (c), the integrated QD peak intensity I_{GaSb} linearly increases by means of excitation powers, which can occur in both temperatures of 20 K and 30 K. This can be considered that the steadily exciton recombination occurs. Due to the noise signal, the linear fit cannot fit well at low laser power. The saturating of peak intensity is observed at higher excitation power. This

can be speculated that the carrier recombination is slow with time and the band-bending effect of type-II QD also relates with time.

We can qualitatively explain the QD size distribution by FWHM of QDs PL peak. Figure 5.5 (d) shows the plots of FWHM of GaSb QDs and GaAs layers PL peaks measured at 20 K and 30 K. It can be generally considered that the FWHM of GaSb peaks are getting narrower by increasing excitation laser power, and which are varied in the range of 145-180 meV in both measured temperatures; 20 K and 30 K. The FWHM of GaAs peak oppositely increases by increasing excitation power. At 20 K, the FWHM of GaSb QD peak is constant at about 148 meV in the higher range of excitation power 256-340 mW, and at 30 K, the FWHM of QD peak is about 149 meV in the excitation power range of 176-320 mW, respectively. The observed values are larger than the reported value of 104 meV [36]. This can be attributed to the less homogeneity of QD size distribution and the large Sb-for-As intermixing at the interfaces.

Temperature dependent PL measurement is performed to investigate the carrier quantization and localization in the QDs and, carrier escaping from the QDs to nearby barrier via thermal activation process [68-72]. Temperature dependent PL is measured from 20 K to 290 K with 225 mW incident excitation power. Figure 5.6 (a) shows the temperature dependence PL spectra of GaSb/GaAs QDs. With increasing temperature, the red shift of PL has been occurred by PL intensity decaying which arises from the thermionic emission of the photo-carriers. The shift of the QDs lines is slightly pronounced at higher temperatures over 100 K. The decreasing of integrated PL intensity as a function of temperature is extracted by Gaussian peak fitting. Figure 5.6 (b) shows the temperature dependent curve of the GaSb peak energy as a function of increasing temperature fitting by the Varshni equation.

The PL intensities are rapidly decreased by increasing temperatures, and which can be attributed to the high thermionic carriers escaping caused by the non-radiative defect sites at the interfaces [73-75]. In order to investigate the carrier thermal escaping and PL quenching by means of increasing temperature, activation energies are calculated from the Arrhenius plots of temperature dependent integrated PL intensities as shown in figure 5.6 (c). Arrhenius plots are fitted by the Arrhenius equation [13]:

$$PL(T) = \frac{c}{1 + \alpha \exp\left(\dfrac{-E_a}{k_B T}\right)} \qquad (5.1)$$

where c and α are the constants, k_B is the Boltzmann constant, T is the measuring temperature and E_a is the activation energy, respectively. The activation energy of 44 meV is observed. In here, the fast PL quenching of QD peak intensity indicates the low the carriers (holes) transfer from WL to QDs due to the QDs peak is very close to WL peak originally, and the existence of non-radiative defect states at the interfaces of the heterostructrues due to higher Sb-As intermixing.
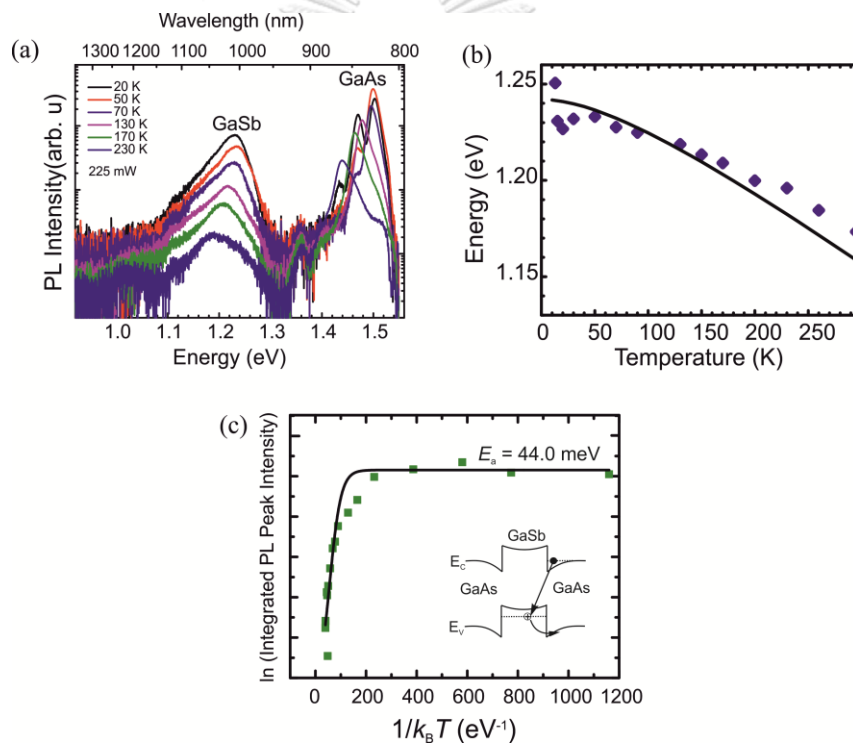
Figure 5.6 (a) Temperature dependent PL spectra of GaSb/GaAs QD at high excitation power $P = 225$ mW. (b) The temperature dependent curve of the GaSb peak energy. The solid line is fitted by the Varshni equation. (c) The integrated PL intensity in log scale as a function of reciprocal temperature. Arrhenius plots fitted (line) to the experimental result (symbol), showing thermal activation energy of GaSb QDs. Inset shows schematic diagram of energy band structure with carrier recombination and escaping process during temperature dependent PL measurement.

In this chapter, 3 ML GaSb/GaAs QDs are grown on (001) Ge substrate at 450ºC. The effect of APDs on the formation of QDs is discussed. By careful controlling of growth, APDs surface flattens and enlarge enough to deposit QDs array. The induced tensile strain in GaAs layer due to the buried GaAs QDs is investigated by Raman spectroscopy. The power dependent PL measurement shows the type II band alignment of GaSb/GaAs at 30 K. The broad PL linewidth indicates the high intermixing rate of Sb-for-As at the heterostructure interfaces. The low activation energy E_a supports to this result as well.

Chapter 6

Effects of Various Growth Conditions on GaSb/GaAs Quantum Dots

Controls of density, dimension, and position of semiconductor QDs are important prerequisites for utilizing them in many novel QD-based device applications [76-78]. In this chapter, the experimental results on the different growth conditions of GaSb/GaAs self-assembled QDs are shown and discussed. The QD formation is monitored by *in situ* RHEED pattern observation. The various growth parameters; the effect of growth rates, growth temperatures and amount of GaSb deposition on the morphology of QD nanostructure is characterized by AFM. The strain relieved behaviour corresponds to the morphology of QDs is observed by Raman scattering spectroscopy. The PL spectroscopy is utilized to investigate the optical quality of GaSb/GaAs type-II QDs in different growth conditions. In addition, the high emission polarization is successfully carried out by polarized resolved photo-luminescence (PRPL).

6.1 Effects of QD Growth Temperature on GaSb/GaAs QDs Morphology

At various growth temperatures, a total coverage of 3-ML GaSb/GaAs QDs are grown on 500 nm-thick GaAs buffer layer decorated by APD. All samples are grown with slow growth rate ~0.11 ML/s by fixing Sb_4 flux at ~5×10^{-7} torr. Self-assembled GaSb QDs are realized in SK mode. Then QDs layer is capped by 150 nm thick GaAs layer for PL measurement, and QDs at the same growth conditions are grown on top layer for AFM analysis. (The experimental details are described in Chapter 3.) The controlling growth parameter in this section is the QDs growth temperature in the range from 400ºC up to 550ºC.

Figure 6.1 (a) shows the 2×2 μm^2 AFM images of GaSb/GaAs QDs grown at different growth temperatures; 400ºC (i), 450ºC (ii) and 500ºC (iii) respectively. QDs cannot be deposited at high temperature 550ºC (iv). QD size, shape and density are varied by means of growth temperature. The corresponding height and diameter/length of GaSb/GaAs QDs at different growth temperature are shown in Figures 6.1 (b, c). By increasing growth temperature, QD size (height and diameter/length) increases from average height of 4.6 nm (400ºC) to 7.4 nm (450ºC)

and 10.9 nm (500°C), and from average diameter/length of 35.1 nm (400°C) to 46.9 nm (450°C) and 82.2 nm (500°C) respectively. The average QDs height, diameter/length are extracted from AFM data by assuming a Gaussian distribution of QDs. QD density decreases from 2.4×10^{10} cm^{-2} to 2.1×10^{10} cm^{-2} and 2.28×10^{9} cm^{-2} by increasing growth temperature from 400°C to 500°C. At higher temperature, QD size distribution is larger and density is lower. This is because the lower areal density leads to larger amount accumulated material per nanostructure.

GaSb/GaAs QDs shape interestingly transforms from circular based shape QDs to rectangular based shape QDs at growth temperature 450°C. Anisotropic QDs elongate along [110] direction on (001) GaAs APD surface. These APDs have a crystallographic direction perpendicular to the neighbouring domains. The orthogonal nature of GaAs APDs grown on (001) Ge substrate can therefore provide a unique driving force to align elongated GaSb QDs like mat pattern [24].The average elongation aspect ratio of QDs is ~1.22 by means of average length ~47.9 nm and average width ~42.4 nm, which are comparatively larger than the average diameter ~35.1 nm of round-based shape QDs. AFM image of free-standing GaSb/GaAs QDs on Ge substrate clearly reveals the elongation direction of the GaSb QDs in different domains as demonstrated in Figure 6.2.

In generally, the equilibrium shape of the self-assembled strained islands is determined by the balance of the surface free energy and the elastic strain energy [79], [80]. In this case, the surface energy of GaSb changes by increasing growth temperature. The streaky-to-spotty RHEED transition time is faster by decreasing growth temperature, illustrating the diffusion length/time of Ga is shorter. It can be probable that GaSb islands can elongate along [110] direction than other directions because of the existence of anisotropic diffusion length of Ga adatoms in the [110] and [1$\bar{1}$0] directions. When the growth temperature reaches at 500°C, elongated QDs shape cannot be maintained anymore, and the bimodal behaviour of dot size distribution is observed. One possible explanation comes from the role of Sb adatoms detachment, desorption and diffusion from the smaller QDs to the larger one, and results the decrease of QD density and an increase of QD size at higher growth temperature [81].
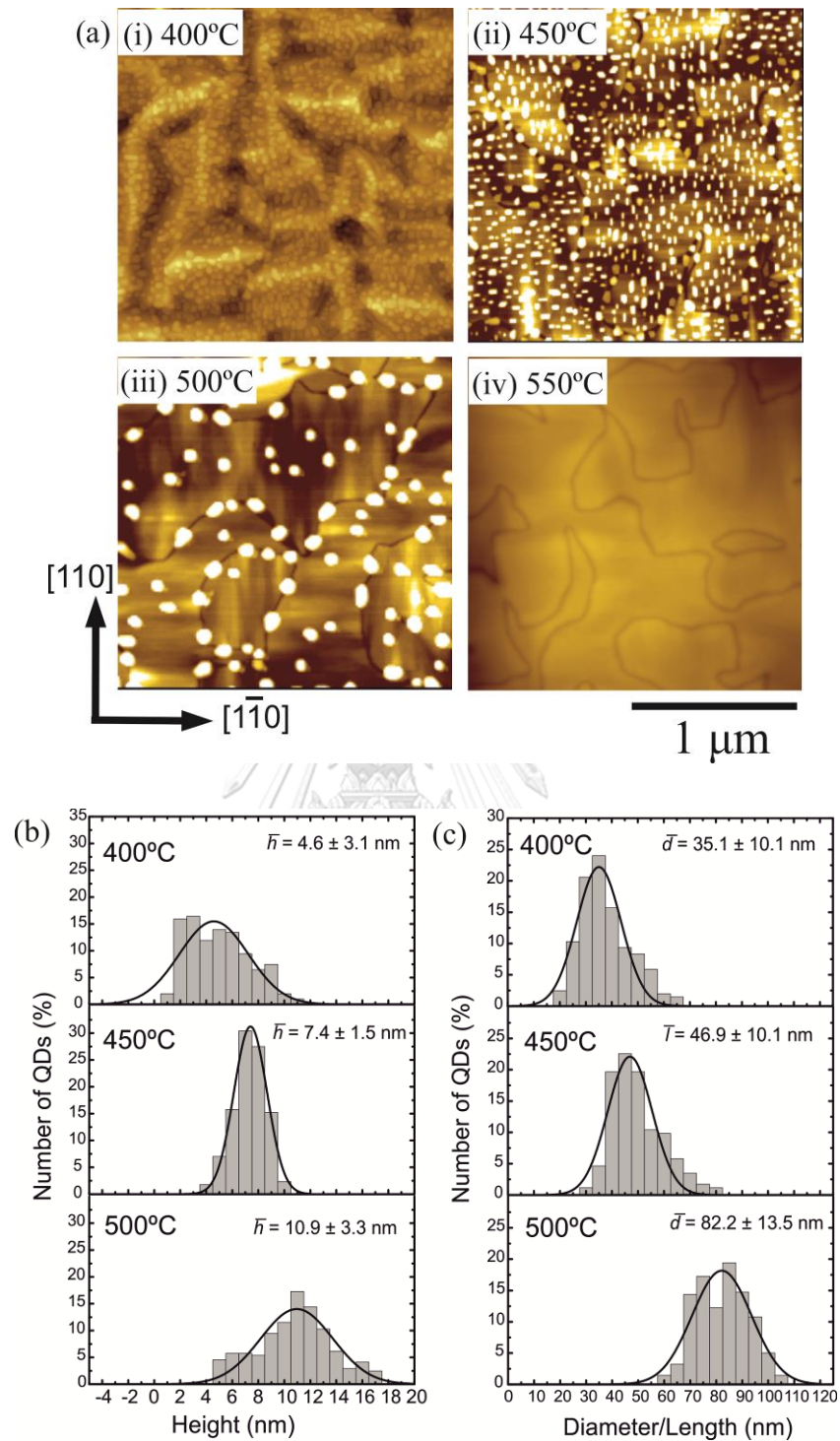
Figure 6.1 (a) 2×2 μm² AFM images of 3 ML GaSb/GaAs QDs grown at (i) 400ºC, (ii) 450ºC, (iii) 500ºC and (iv) 550ºC, and (b) the corresponding height and diameter/length histograms of 3 ML GaSb/GaAs QDs grown at different growth temperatures shown in (a). The dot density decreases as the growth temperature increases.
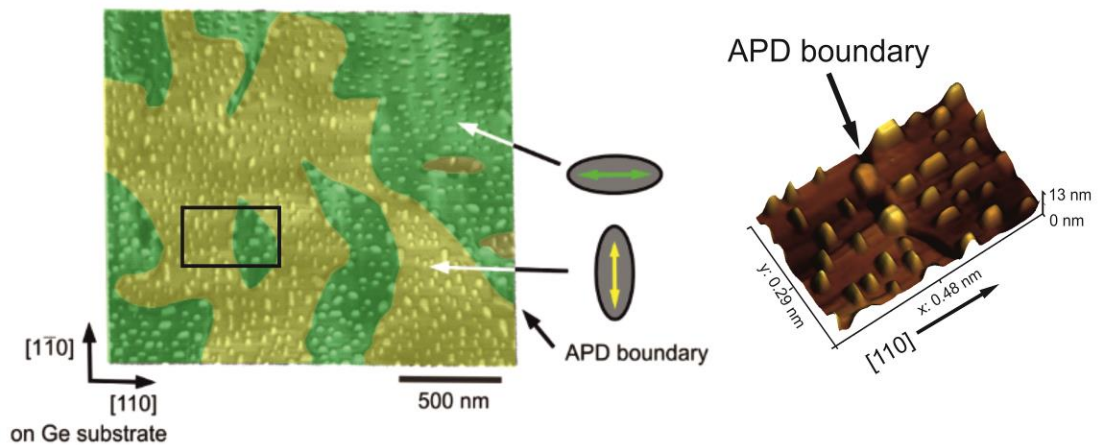
Figure 6.2 AFM image of the elongated GaSb QDs on different GaAs APDS. The orthogonal domains are highlighted with different colours. GaSb QDs on each domain are elongated along [110] crystallographic direction of underneath GaAs APDs. The rectangle box marks an area of APB and APDs with the QDs which shows on the right as a 3D AFM image.

PL spectroscopy on capped GaSb/GaAs QDs grown at different growth temperatures is conducted. The PL measurement is carried out at 20 K for all samples. Figure 6.3 shows the normalized PL spectra of 3 ML GaSb/GaAs QDs grown by increasing growth temperature from 400ºC up to 550ºC. In PL spectra, the ground state energy peak of GaSb QDs can be well resolved. By adjusting the objective/collecting lens in the PL set up, the target wavelength range for QDs emitted peak can be focused by suppressing the GaAs peak at ~1.47 eV. For the QDs with weak PL intensity, the GaAs peak cannot be suppressed completely.

The PL peak energies of GaSb QDs grown at 400ºC, 450ºC and 500ºC are at ~1.15 eV, 1.13 eV and 1.22 eV respectively. A slight redshift of PL peak energy from 1.15 eV to 1.13 eV for the QDs grown at 400ºC and 450ºC is the result of the larger QD size and height at higher growth temperature. Larger QDs have lower number of quantized energy levels of confined holes in QDs, which causes a lower PL peak energy position. Whereas at 500ºC, the PL peak shifts to higher energy, and this can be explained by the Sb-for-As exchange reaction and dissolution effect during capping process [82], leads to the decrease of buried QD volume. According to AFM and PL results, QDs cannot be deposited at very high growth temperature 550ºC due

to Ga evaporation and high Ga desorption rate. Note that the sample grown at 550ºC has not been capped by GaAs. The PL spectrum is emitted directly from the Sb-segregated/diffused GaAs layer. GaAs peak is emitted at ~1.47 eV contributing with the shoulder peak at ~1.38 eV which is emitted from Sb segregated/diffused $GaSb_xAs_{1-x}$ layer. This shows that the Sb segregation and/or Sb-As anion exchange can take place at very high substrate temperature.

Moreover, PL linewidth relates to the QD size homogeneity, and the structural properties of QDs can be deduced by PL. The PL linewidth of the ground state PL peak spectrum is extracted by Gaussian distribution function. The broad PL line width indicates the lower size homogeneity of QDs in both low and high growth temperatures; 400ºC and 450ºC. The narrow PL linewidth observed at very high growth temperature 500ºC provides the idea of carrier recombination occurs at the thin WL.

Figure 6.4 (a) shows the excitation power dependence of the PL spectra are depicted for GaSb/GaAs QDs grown at 400ºC, 450ºC and 500ºC respectively. The dependence of PL peak energy on the third root of excitation power ($P^{1/3}$) is shown in Figure 6.4 (b). When the excitation power increases, a shift of PL maximum to higher energy (blue shift) is observed. This is the characteristic of type-II band alignment, causing the spatial separation between holes confined in the GaSb QDs and electrons in the nearby GaAs region. The accumulated electrons in the GaAs barrier are attracted by the holes confined in GaSb QDs by Coulomb attraction force, results the bending of conduction band into a triangular QW shape and gives rise to discrete electron energy levels. By increasing the excitation power, the larger photo-generated carriers accumulate in and around the QDs, and which induce the steeper triangular potential well at the interface of GaSb QDs and GaAs layer. Because of the change of electron energy level relative to the hole energy level, a blue shift of PL spectrum results. Three samples grown at different temperatures exhibit the almost linearly fit with $P^{1/3}$, which is the characteristic of the type-II band structure.
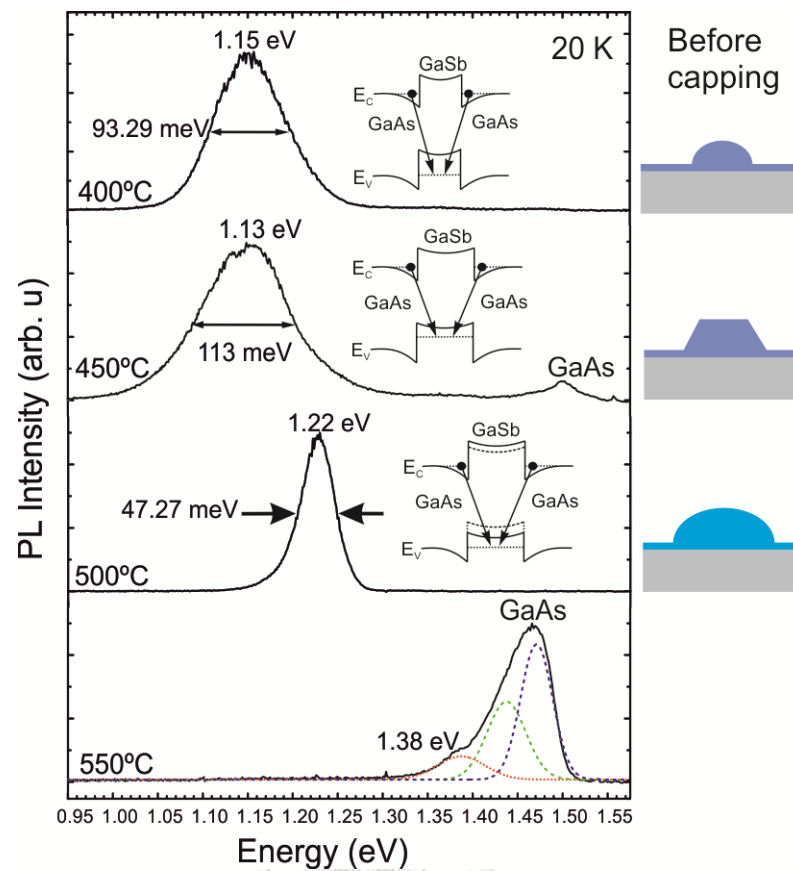
Figure 6.3 Low temperature PL spectra of 3 ML GaSb/GaAs QDs grown at different growth temperatures. The excitation power is 150 mW. The insets show the corresponding band structures. The schematics on the right of the figure illustrate the the GaSb/GaAs QDs before GaAs capping.
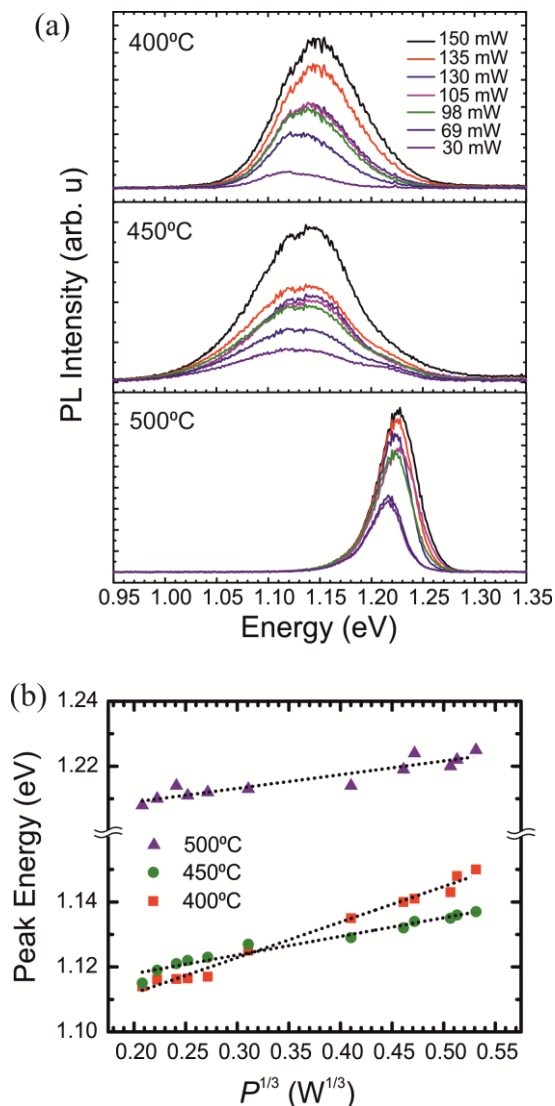
Figure 6.4 (a) Power-dependent PL spectra of GaSb/GaAs QDs grown at different temperatures. The blue shift of the QD PL peak with increasing excitation power indicates the type-II band characteristic. (b) The shift of the PL peaks energy as the third root of the excitation power at 20 K. The dashed line is a linear fit.

After discussing the strain effect in GaAs layer due to the presence of buried GaSb QDs in the Chapter 5, we will present the responding strain effects in this section. Raman spectroscopy is measured at RT by using 532-nm laser. The dominant peaks are TO and LO modes of GaAs and the GaSb related peaks are observed in 210 cm^{-1} to 250 cm^{-1} range as shown in Figure 6.5 (a). In this case, the GaSb-like modes can be clearly seen whilst it cannot be seen in the previous chapter (Chapter 5).

This indicates the qualitatively improvement of crystallinity of QDs in both formation and capping process with lower percentage of intermixing effect during capping. To quantify the peak positions, the peaks are fitted by Gaussian function as shown in Figure 6.5 (b). A drastic red shift of TO and LO modes of GaSb from 224.89 cm^{-1} and 236.44 cm^{-1} to 217.35 cm^{-1} and 230.25 cm^{-1} is observed since the LO and TO phonons in bulk GaSb are 238cm^{-1} and 228 cm^{-1} [20]. The red shift of the peaks is attributed to the dependency of strain of GaSb on QD size.
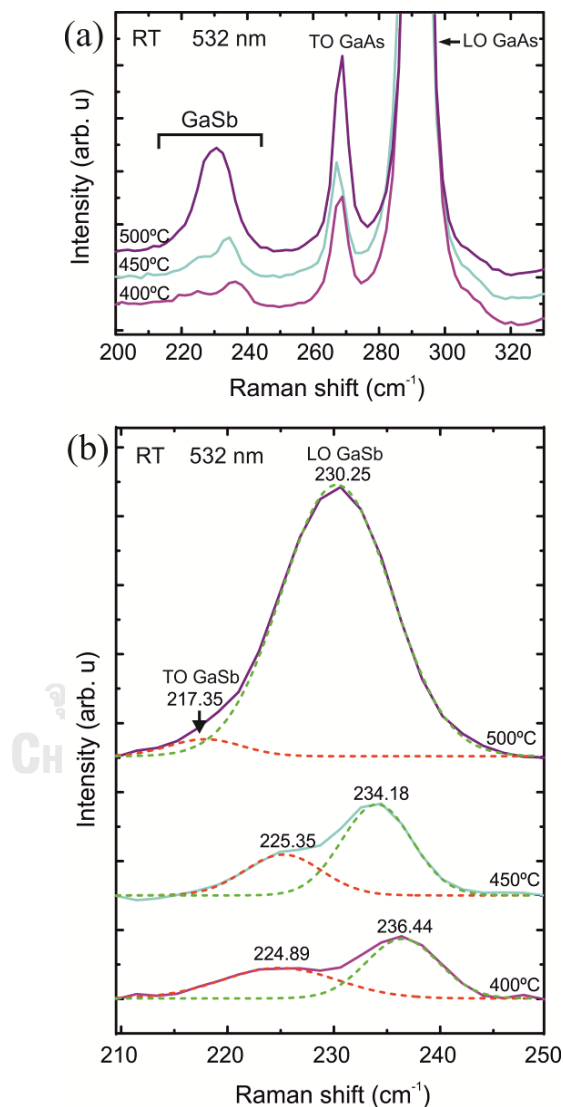

Figure 6.5 (a) Raman spectra measured from GaSb/GaAs QDs grown at different temperatures, (b) Raman spectra described the redshift of TO and LO GaSb peaks due to the relieved strain effect. (The dashed lines are from the Gaussian fits.)

6.2   Effects of Deposited GaSb Amount

From the previous section, the elongated 3 ML-GaSb QDs grown at 450ºC has been interested for its displayed QD array. For deeply understanding of QD shape transformation and size distribution, the effect of deposited GaSb/GaAs QDs amount by increasing GaSb deposition time is studied in this section.

QDs are grown with Ga growth rate ~0.11 ML/s at growth temperature 450ºC. Then GaSb QDs layer are capped by GaAs for PL measurement, and the upper QDs layer are deposited for AFM analysis. The buried QDs size will be smaller and thinner than the upper QDs size distribution due to Sb-for-As intermixing and diffusion effect.

The trend of QD transformation from 2D islands into 3D islands or self-assembled QDs are carefully observed by RHEED pattern transition. After Ga deposition for 15 s, RHEED pattern transforms form streaky pattern to spotty pattern results of 3D QD formation. Thus it can be assumed that the critical thickness of GaSb/GaAs QDs grown with growth rate 0.11 ML/s at 450ºC is about 1.5 ML nominal thickness. The bright and spotty RHEED pattern of 1.5 ML GaSb/GaAs QDs is shown in Figure 6.6. For further deposition of GaSb to the thickness of about 1.5 ML to 3.5 ML leads to a transformation of QDs shapes and size distribution. Figure 6.7 shows the AFM images of GaSb/GaAs QDs deposited in different thickness. At the stage of 1.5 ML nominal thickness, QDs size distribution is inhomogeneous and the GaAs layer surface is rough. This might be due to the Sb condensation and diffusion in low-growth-rate QDs at low growth temperature, causes the surface coarsening. The surface roughness becomes lower in further deposition of longer time 15 s to 35 s. The QDs in critical thickness 1.5 ML have an average height (diameter) of 4.3 nm (37.25 nm) with the low density of about 1.25×10^{10} cm^{-2}. As shown in the QDs height histogram of Figure 6.7 (a), accumulated QDs exhibit the large size distribution in mainly two groups, and the percentage of smaller QDs is higher than that of larger QDs. The QDs size and density increase by increasing GaSb deposited amount. The height (density) of GaSb QDs in different QD deposited amounts; 1.5 ML, 2 ML, 2.5 ML, 3 ML and 3.5 ML, are   4.8 nm (1.32×10^{10} cm^{-2}), 6.5 nm (1.87×10^{10} cm^{-2}), 7.4 nm (2.1×10^{10} cm^{-2}) and 8.8 nm

$(2.01 \times 10^{10} \text{ cm}^{-2})$ respectively. At 3.5 ML GaSb deposited amount, QDs density is lower again due to the material diffusion process from smaller QDs to larger QDs.

[110] azimuth
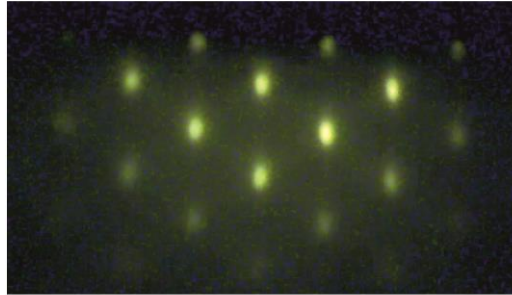
[100] azimuth
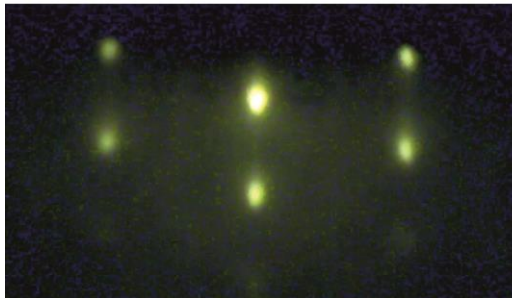

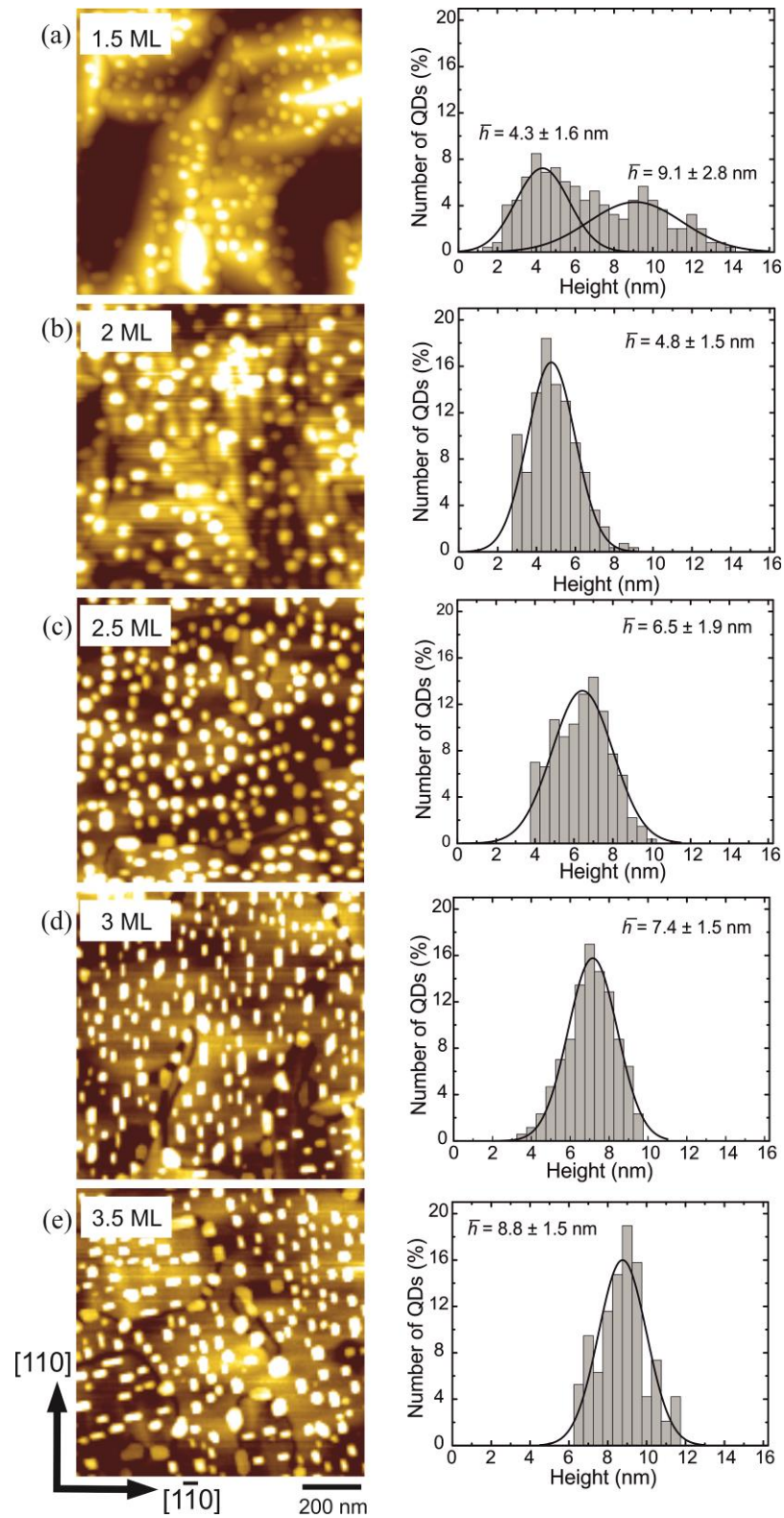Figure 6.6   RHEED patterns of 3 ML GaSb/GaAs QDs in [110] and [100] azimuths.

Figure 6.7 1×1 μm² AFM images and the corresponding height histograms of GaSb/GaAs QDs on GaAs APDs surface. The GaSb thicknesses are (a) 1.5 ML, (b) 2 ML, (c) 2.5 ML, (d) 3 ML, and (e) 3.5 ML.

At low growth rate and low growth temperature, the drastic transformation of QD size and shape as a function of GaSb deposition amount is investigated. The schematic diagrams of QD transition process by GaSb deposition time (amount) is depicted in Figure 6.8 (a). The process starts from the GaSb QDs critical thickness (deposition time) 1.5 ML (15 s) having average diameter 37.25 nm and the QDs transformation is discussed in five steps. From step 1 to step 3, the self-assembled 3D QDs is accumulated in circular based-shape. During further QD deposition time (steps 4 & 5), QDs shape transforms from circular based-shape to rectangular based-shape, in which steps, one side of QD or the length of QD along [1$\bar{1}$0] direction is shorter and the other side of QD or the length of QDs along [110] direction is longer. The QD height is higher by increasing of Ga deposited amount (See in Figure 6.8 (b)).

.   Statistical average height and lateral lengths of GaSb QDs by increasing deposition time are shown in Figure 6.9 (a) where the effect of GaSb deposited amount on geometrical anisotropy of GaSb QDs is summarized. It can be seen that the lateral lengths along the [110] and [1$\bar{1}$0] directions are nearly symmetric in GaSb depositied amounts; 1.5 ML, 2 ML and 2.5 ML. By further increasing the deposition amount to 3 ML, the QD width along [1$\bar{1}$0] direction is shorter and the length along [110] direction is longer. At 3.5 ML, the lengths of QD both in [1$\bar{1}$0] and [110] directions are longer. The elongation ratio or aspect ratio between the lateral lengths along [110] direction and [1$\bar{1}$0] direction vs. the GaSb deposition time graph is plotted as shown in the inset of Figure 6.9 (b). The elongation ratio increases from 1.02 to 1.71 by increasing GaSb deposition time since the QD length along [1$\bar{1}$0] direction is shorter and the length along [110] direction is longer. Therefore, the QD shape transforms from circular based-shape to rectangular-based shape. In the meantime, QD height is steadily increased by increasing dot deposited amount. Therefore, it can be assumed that the critical thickness of rectangular based-shape QD is around 3 ML (over 2.5 ML) with low growth rate ~0.11 ML/s at low growth temperature 450ºC. Compare to the reported works [79, 80], in our case, the elongated QDs have no flat top mesa by closer looking at the AFM image. This may be due to the small elongation ratio of the QD lengths and size distribution. To quantify the

formulated QDs, the surface orientation mapping, which is so-called facet-plot was analysed. Figure 6.10 shows the facet diagrams of 2.5 ML QDs and 3 ML QDs. Dots faceted plot showed the QD shape transition in different QD deposited amount. Beyond 2.5 ML of QD deposition, QD faceted plot transforms to the rectangular based-shape (See in Figure 6.10 (b)).
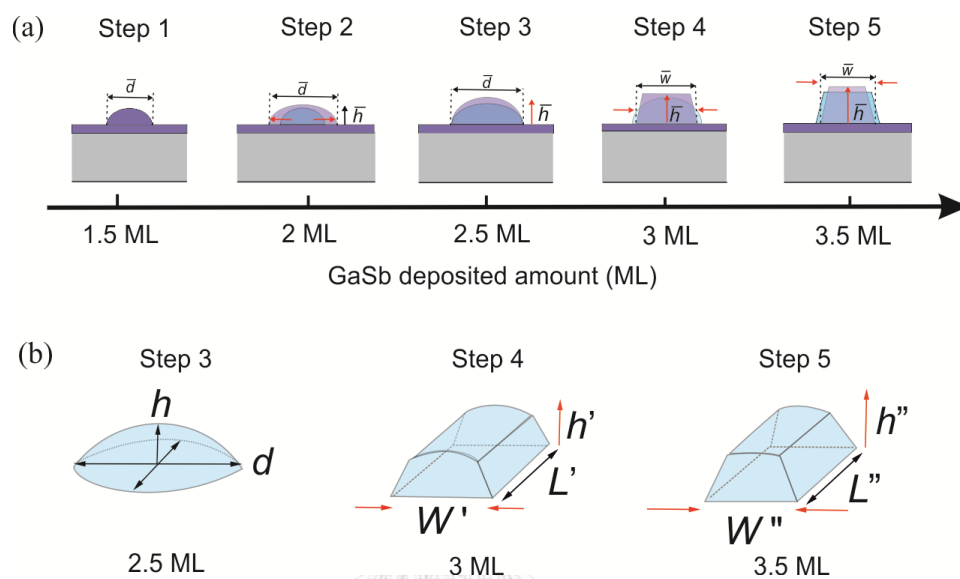
Figure 6.8 (a) Schematic diagram for showing the QD shape transformation in 5 steps of QD deposited amount. (b) Illustration of GaSb QD shape transformation from circular based-shape to rectangular based-shape with detailed information of QD lateral size and height. As increment of QD deposited amount beyond 2.5 ML, the QD lateral lengths W is shorter and the other side of QD lateral length L is longer in step 4, and both of lateral lengths are longer again in step 5. QD height h increases steadily during further QD deposition.
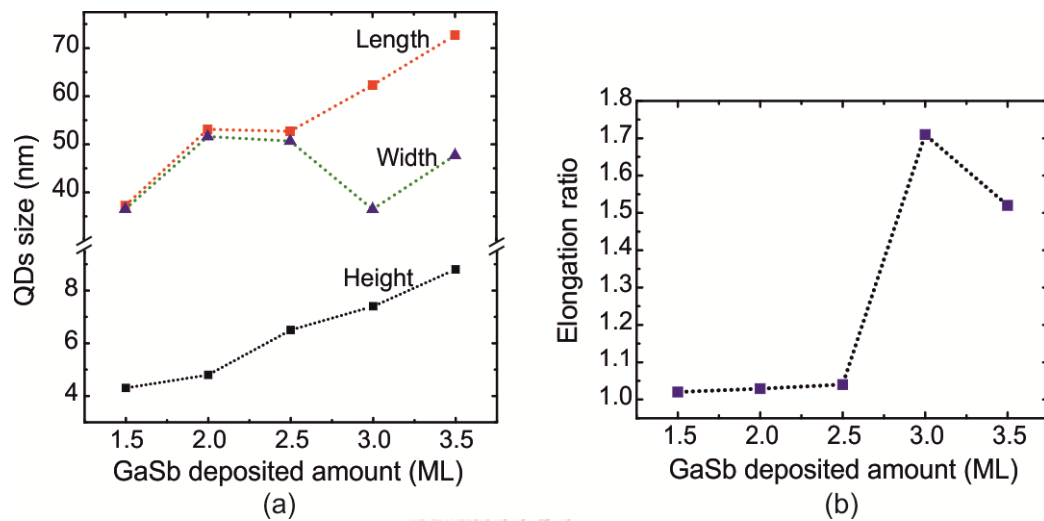
Figure 6.9 The graphs showing (a) the statistical average height and lateral lengths (length, width) for GaSb QDs vs. GaSb deposited amount, and (b) the elongation ratio (aspect ratio of length to width) as a function of GaSb deposited amount.
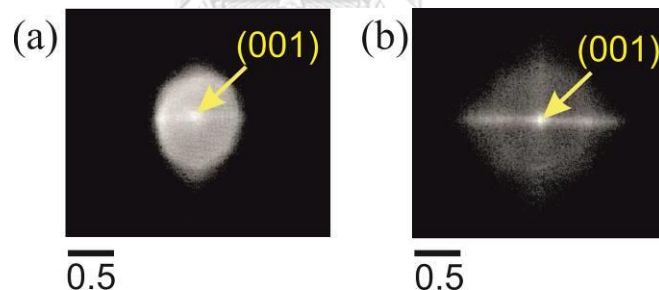
Figure 6.10 Facet plots of (a) circular based-shape 1.5 ML GaSb QDs and (b) rectangular based-shape 3 ML GaSb QDs.

The formation mechanism for elongated QDs can be discussed as mentioned in previous section 6.1. In this section, we observed the more detailed dot transformation by increasing dot deposited amount. We observed that QD shape transforms to rectangular base shape due to the shortening and extending of the QD lateral length along [1$\bar{1}$0] and [110] directions, and the higher QD thickness. This implies the effects of the interplay between the surface free energy and elastic strain

energy on the QD growth morphology. Larger 3D island has higher strain energy for the atoms at the edges than the smaller island, leads to the strain induced adatom detachment and diffusion from the large 3D island in order to maintain the stable condition of QD. Since any adatoms that attach to the island find their way to strain relieved area, QD lateral diameter/length saturates in a particular condition and QDs height increases. The anisotropic diffusion length of Ga adatoms in the [110] and [$1\bar{1}0$] directions creates the asymmetric strain induced energy around QDs, hence leading to the lateral length shortening and extending in [$1\bar{1}0$] and [110] directions. This can attribute to the higher strain energy in [$1\bar{1}0$] direction than that in [110] direction of GaSb/GaAs QD.

The low temperature PL measurement of GaSb/GaAs QDs grown at ~0.11 ML/s with QD deposited amounts of ~1.5 ML, 2 ML, 2.5 ML, 3 ML and 3.5 ML are shown in Figure 6.11. The PL peaks of GaSb QDs are observed in the range of 1.14 eV to 1.20 eV. The PL spectra show the QD deposited amount dependent QD size distribution and the QD size fluctuation as a function of QD deposited amount. The PL peak shifts to lower energy (1.2 eV to 1.14 eV) as a result of the larger QD size when the QD deposited amount increases. Further deposition of QD at 2 ML and   2.5 ML, there is no PL peak shifting is observed. This is because of the larger QD size fluctuation and density by accumulation of more Ga atoms. The broader PL linewidths of 2.5 ML QD and 3 ML QD than that of 2 ML QD show the decrease in QD size homogeneity. Further growth of 3 ML and 3.5 ML QD, the PL peak shifts to higher energy, this may be due to the higher Sb-for-As intermixing effect during capping process.
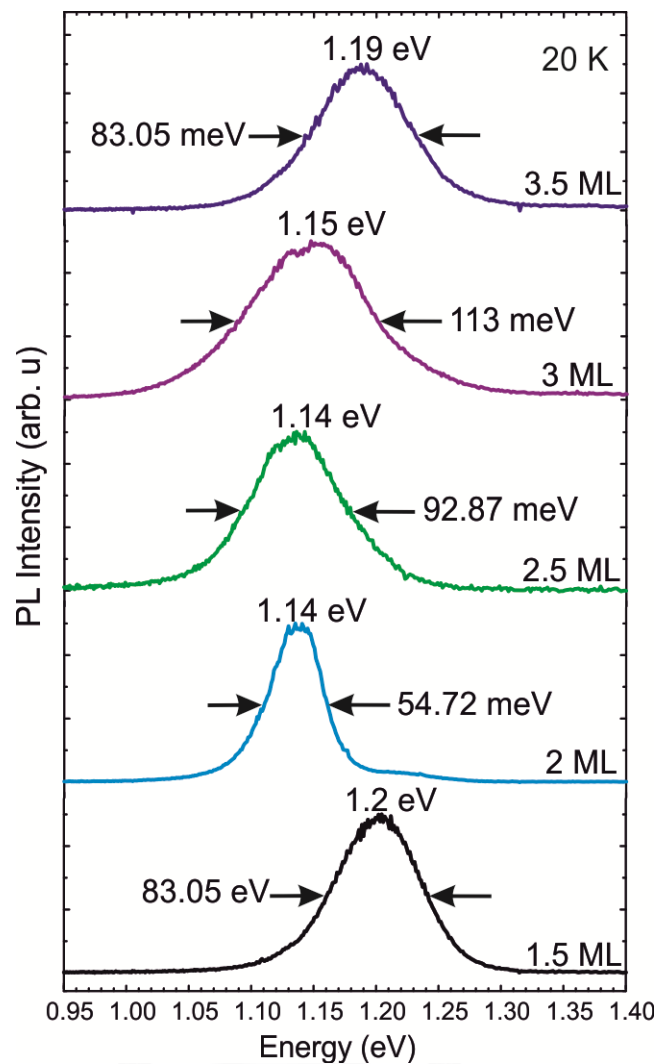
Figure 6.11 Normalized PL spectra of GaSb QDs for different GaSb deposited amount. The PL spectra are measured at temperature 20 K with excitation power 150 mW.

6.3 Effects of Ga Growth Rate on GaSb/GaAs QD

Based on the several reported works, the QD growth rate, amount of deposited QDs and QDs growth temperature can strongly affect the density and the size distribution of QDs. As it has been discussed in the previous Sections (Sec. 6.1 & 6.2), the GaSb QD morphology is greatly affected by the QDs growth temperature and amount of deposited QDs. Moreover, the elongated 3 ML-GaSb QDs grown at 450ºC has been interested for its displayed QD array and QD shape. Therefore, in this section, in order to understand about the elongated GaSb QD morphology and

properties by the effect of Ga growth rate, 3 ML GaSb QDs are grown with different growth rates; 0.24 ML/s, 0.18 ML/s, 0.14 ML/s, 0.11 ML/s and 0.09 ML/s at 450ºC. Sb_4 beam flux is fixed at ~ 5×10^{-7} torr. AFM analysis, Raman scattering measurement, power dependent PL measurement and polarized-resolved PL measurement are utilized to investigate the QD morphology and optical properties.

1×1 μm^2 AFM images of 3 ML GaSb QDs grown with different growth rates are shown in Figure 6.12. The statistical analysis of QDs size distribution is done by extracting the AFM data. By systematically reducing the Ga growth rate from 0.24 ML/s to 0.09 ML/s, the growth rate dependent QDs size and shape transformations are realized. QD height increases steadily by varying QD growth rate as shown in histograms of Figure 6.12, whilst, the QDs densities remains nearly the same as the decrease of growth rate from 0.24 ML/s to 0.11 ML/s as follows: 2.51×10^{10} cm^{-2}, 2.7×10^{10} cm^{-2}, 2.3×10^{10} cm^{-2} and 2.1×10^{10} cm^{-2}, except the very low growth rate at 0.09 ML/s exhibits the lower QD density 1.7×10^{10} cm^{-2}. This corresponds to the reduction of QD density with larger QD size when the growth rate is decreased.

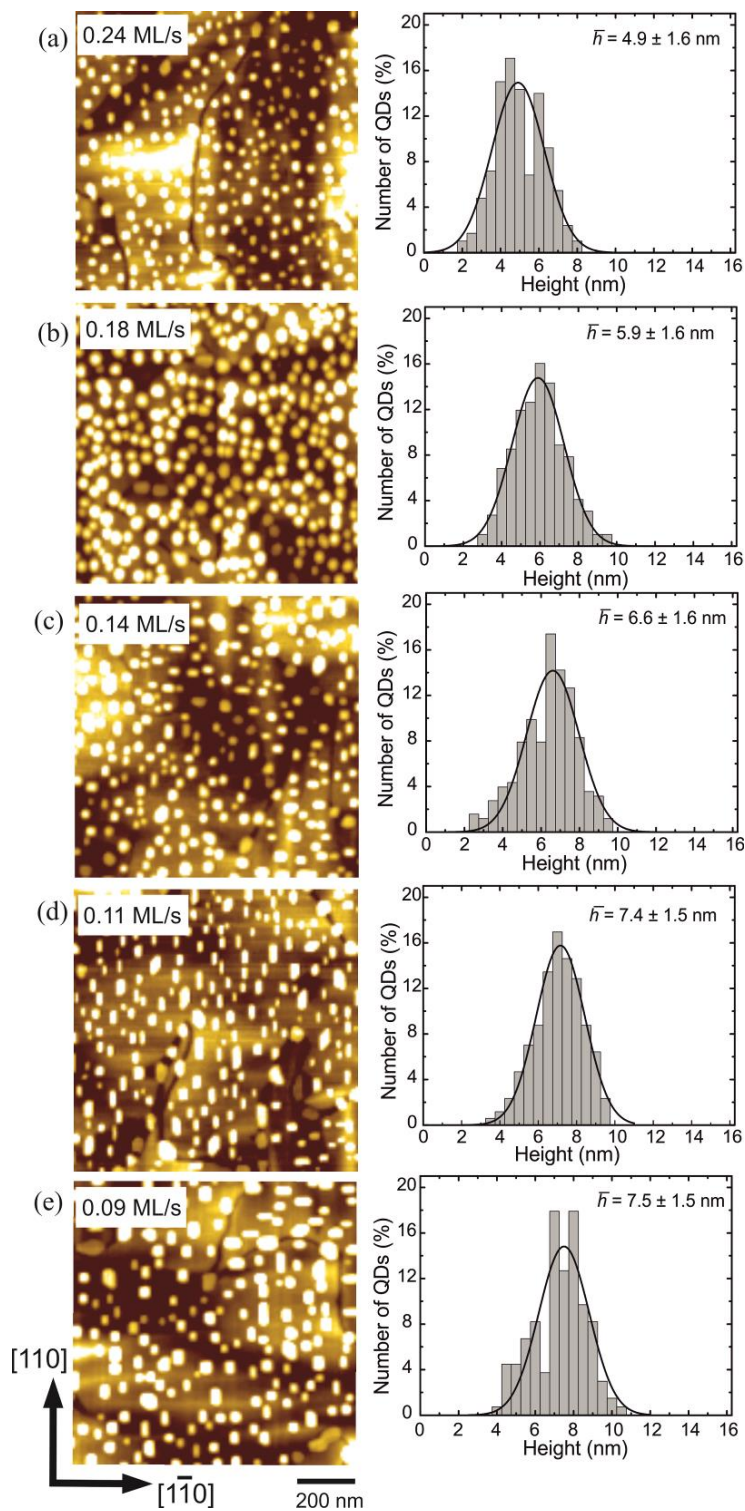Figure 6.12 1×1 μm² AFM images and the corresponding height histograms of GaSb/GaAs QDs grown with different Ga growth rates. The Ga growth rates are (a) 0.24 ML/s, (b) 0.18 ML/s, (c) 0.14 ML/s, (d) 0.11 ML/s, and (e) 0.09 ML/s.

Statistical average height and lateral lengths of GaSb QDs as a function of growth rate are quantitatively summarized in Figure 6.13. The average QDs lengths (widths) of QDs grown with different growth rates; 0.24 ML/s, 0.18 ML/s, 0.14 ML/s, 0.11 ML/s and 0.09 ML/s are 48.4 nm (46.1 nm), 49.2 nm (46.5 nm), 56.1 nm (44.5 nm), 62.3 nm (36.5 nm) and 62.1 nm (37.6 nm), respectively. Since the lateral length of QD along [110] direction (length) elongate and the other length of QD along [1$\bar{1}$0] direction is shorter by reducing the growth rate. , The elongation ratio of QD lateral sizes (length/width) is pronounced in slow growth QDs with growth rates; 0.11 ML/s and 0.09 ML/s lower than 0.18 ML/s. The aspect ratio (elongation ratio) of length to width of QD increases from 1.04 to 1.71 as shown in Figure 6.13 (b).
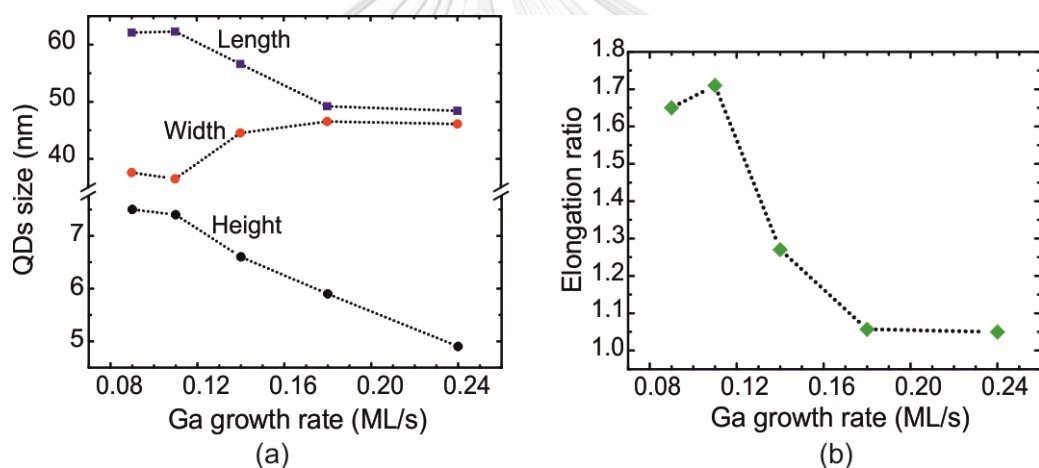

Figure 6.13 The graphs showing (a) the statistical average height and lateral lengths (length, width) for GaSb QDs vs. Ga growth rate, and (b) the elongation ratio (aspect ratio of length to width) as a function of Ga growth rate.

The schematic diagram of QD elongation process is depicted in Figure 6.14. The 2D to 3D QD transformation time is longer by reducing Ga growth rate. The longer transformation time results the longer diffusion length of Ga adatoms. Because of the anisotropic diffusion length of Ga adatoms in [110] and [1$\bar{1}$0] directions, QD can elongate to one specific direction. In our case, QD elongates to [110] direction.
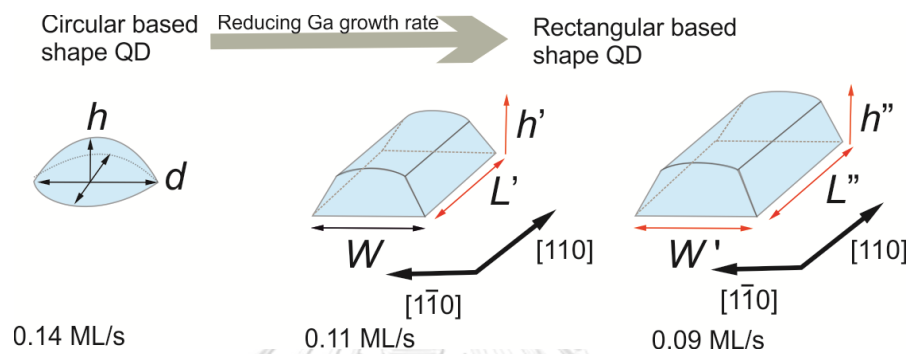
Figure 6.14 Illustration of GaSb QD shape transformation from circular based-shape to rectangular based-shape with detailed information of QD lateral size and height. By reducing Ga growth rate lower than 0.14 ML/s, the QD lateral length along [110] direction *L* elongates, whilst the lateral length along [1$\bar{1}$0] direction *W* is shorter. QD height *h* increases steadily during further QD deposition.

Compare to the previous study in section 6.2, we can speculate the QD elongation process as follows. The self-assembled GaSb QD shape transforms form circular based shape to rectangular based shape by GaSb depositing over 2.5 ML, in which QD lateral length along [1$\bar{1}$0] shortens while QD lateral length along [110] elongates. In this case, the Ga growth rate and Sb_4 beam flux are fixed at 0.11 ML/s and $\sim 5 \times 10^{-7}$ torr, and the QD deposited amount is increased from 1.5 ML to 3.5 ML steadily.

In this section, the growth rate dependent QD shape and size transformation are investigated by reducing growth rate from 0.24 ML/s to 0.09 ML/s at the same Sb_4

beam flux $\sim 5 \times 10^{-7}$ torr and QD deposition amount ~ 3 ML based on the previous study. The growth rate dependent QD morphology is observed. The anisotropic GaSb QD can be obtained at relatively low growth rate. It is observed that the evolution of elongated QD is very similar to the previous investigation of deposited material amount dependent QD. This shows that the anisotropy of QD structure can be controlled by the Ga growth rate. Another possible growth technique is the control of group V amount (Sb beam flux), where the V/III ratio (Sb/Ga) for QD growth should be relatively high. Therefore, it can be concluded that the elongated QD can be obtained at high V/III ratio; high Sb beam flux or low Ga growth rate. In our case, all of the samples are grown at high Sb beam flux and Ga growth rate is controlled.

The strain effect in GaAs layer due to the presence of buried GaSb QDs (Chapter 5) and the compressively strained effect in GaSb QD grown on GaAs layer at different growth temperature (Chapter 6, Section 6.1) have been discussed.

Figure 6.15 (a) shows the Raman spectra obtained from 3 ML GaSb/GaAs QDs grown with different Ga growth rates. All samples exhibit the vibrational modes (TO and LO modes) of GaAs and GaSb related peaks in 210 cm^{-1} to 250 cm^{-1} range. The Gaussian fitting is performed to quantify the peak positions as shown in Figure 6.15 (b). A slightly red shift of TO and LO modes of GaSb from 227.81 cm^{-1} and 236.00 cm^{-1} to 227.61 cm^{-1} and 234.97 cm^{-1} is observed. The red shift of the peaks is attributed to the QD size dependent strain effect of GaSb. The increasing of QD size and height by increasing Ga growth rate leads a shift of intense LO mode to lower energy.
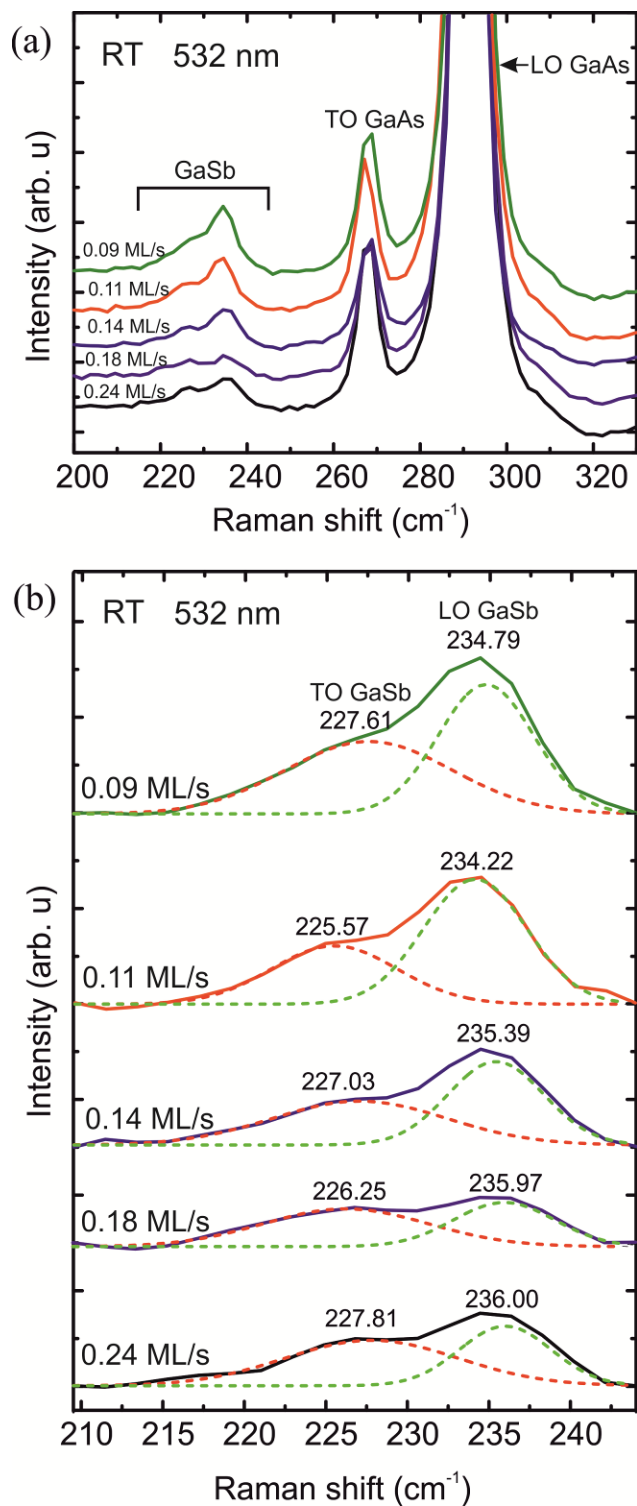
Figure 6.15 (a) Raman spectra measured from GaSb/GaAs QDs grown at different Ga growth rates, (b) Raman spectra described the redshift of TO and LO GaSb peaks due to the relieved strain effect. (The dashed lines are from the Gaussian fits.)

The low-temperature PL measurement is performed at 20 K with excitation power 150 mW are shown in Figure 6.16. The peaks can well be fitted by Gaussian function. The slightly red shift of GaSb PL peaks from 1.18 eV to 1.14 eV reveals the influence of larger QD size corresponds to the lower growth rate. From the AFM results of these QDs with lowering growth rate (0.24ML/s to 0.09 ML/s), the density of QDs does not change much but the height of QD is increased, and hence PL red shift can be attributed to the increasing of QD diameter/length and height of the QD. Whereas the growth rate is reduced from 0.14 ML/s to 0.11 ML/s, the PL peak shifts to higher energy and the PL linewidth is broader. Comparing to the AFM results, QD shape transforms from circular based-shape to rectangular based shape at growth rate 0.11 ML/s and QD size distribution is larger. This stage can be assumed as the dynamic stage of QD shape transformation. For further QD growth with lower growth rate ~0.09 ML/s, the PL peak slightly shifts to lower energy and the linewidth is narrower. This can be explained by the adatom diffusion process. At a low growth rate, the adatoms have the long diffusion length/time and reach more favourable sites before capping the QDs with GaAs. Therefore, QD grown at low growth rate has narrower QD size distribution, hence results the narrower PL linewidth.

The blue shift of GaSb QD peak in all samples is observed when the excitation energy is increased. Figure 6.17 (a) shows the power dependent PL spectra of GaSb QDs grown at different growth rates. The PL energy shift is linear to the cubic root of the excitation power ($P^{1/3}$) as shown in Figure 6.17 (b), which is the type-II characteristic of band alignment of GaSb/GaAs QDs. It can be seen that the integrated PL intensity increases steadily with increased excitation power because more photo-generated carriers are induced and confined in the QDs (holes) and localized around the QDs (electrons) as the excitation power increment.
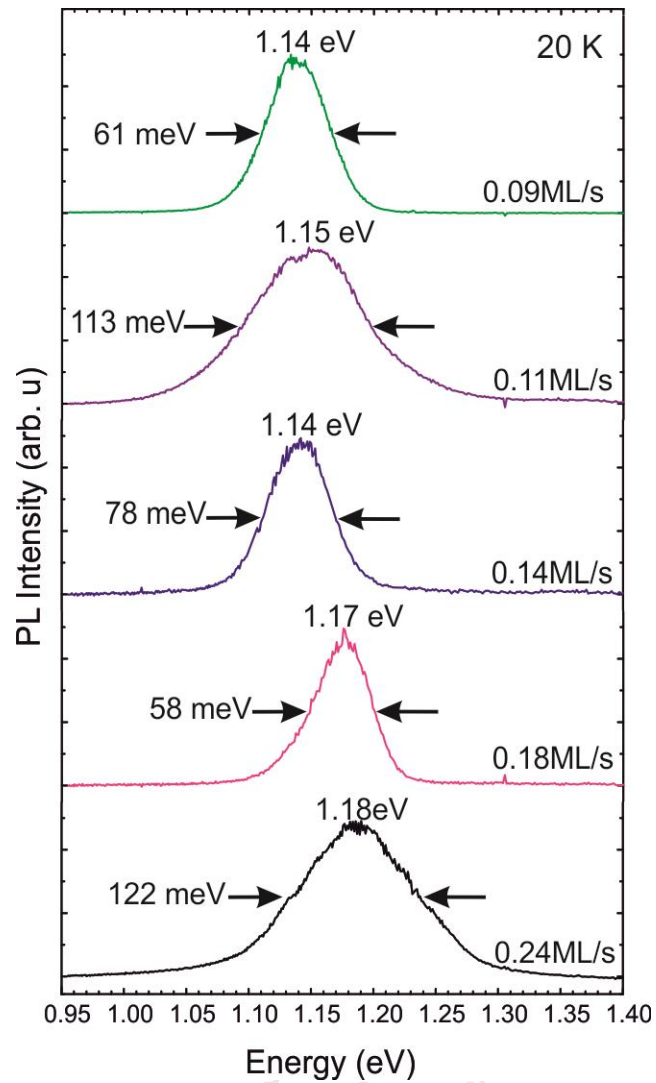
Figure 6.16 Normalized PL spectra of 3 ML GaSb QDs grown at different Ga growth
rates. The excitation power for the PL measurement is 150 mW.
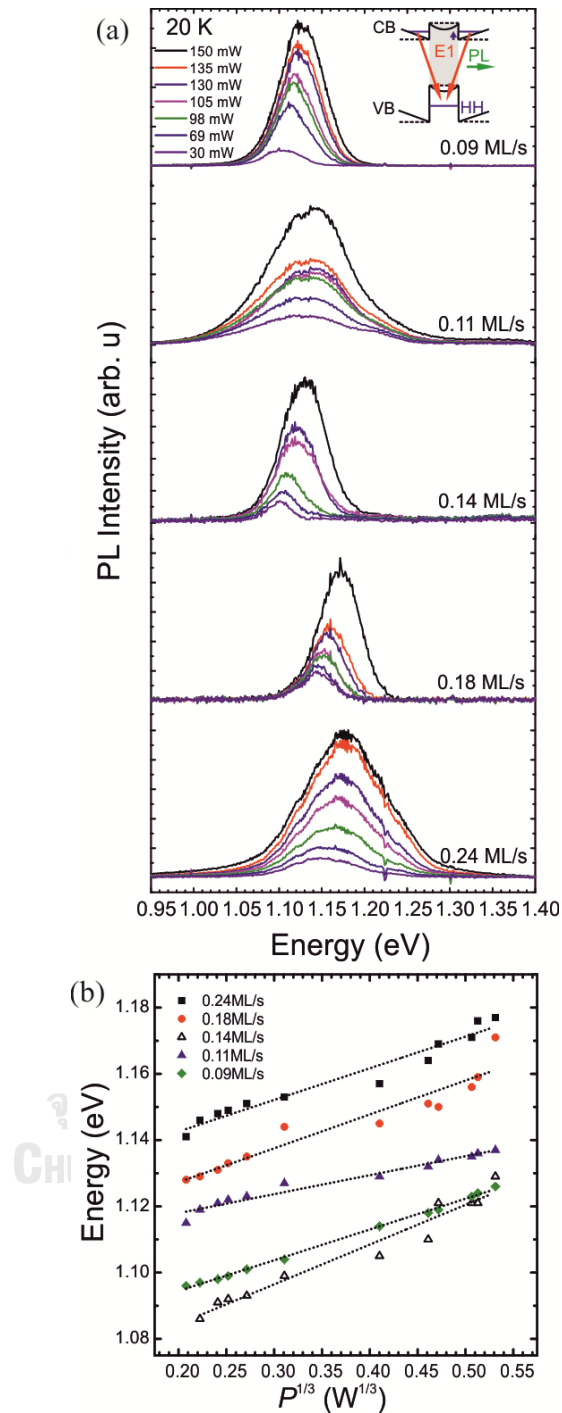
Figure 6.17 (a) Power dependent PL spectra of GaSb QD at different growth rates in the excitation range of 30 mW to 150 mW. The inset shows the carrier recombination mechanism of type-II band alignment. (b) Linear variations of GaSb QD peak energies as a function of the third root of excitation power. The dashed line is linear fit.

Emission polarization dependent PL is another characteristic of type-II GaSb QDs [83, 84]. As shown in Figure 6.18 (a, b), the elongated GaSb QDs at different growth rates of 0.09 ML/s and 0.11 ML/s exhibit the clear polarized luminescence behaviour. The polarization PL is measured at low temperature 20 K with the laser excitation power 150 mW. The percentage of polarization degree can be defined by

$$PD = \frac{(I_{//} - I_{\perp})}{(I_{//} + I_{\perp})} \times 100\% \qquad (6.1)$$

where the $I_{//}$ and $I_{\perp}$ are the PL intensities when the linear polarizer is parallel (perpendicular) to the sample edge. The GaSb QDs grown at growth rate 0.09 ML/s show the large polarization of $\sim 62\%$, whereas the GaSb QDs grown at 0.11 ML/s show the low polarization of $\sim 5\%$. Different degrees of polarization anisotropy (5% to 62%) are observed. The high polarization degree ($\sim 62\%$) could be attributed to the combination effect of the elongated QD shape and the type-II band alignment characteristic, and the QD size homogeneity.
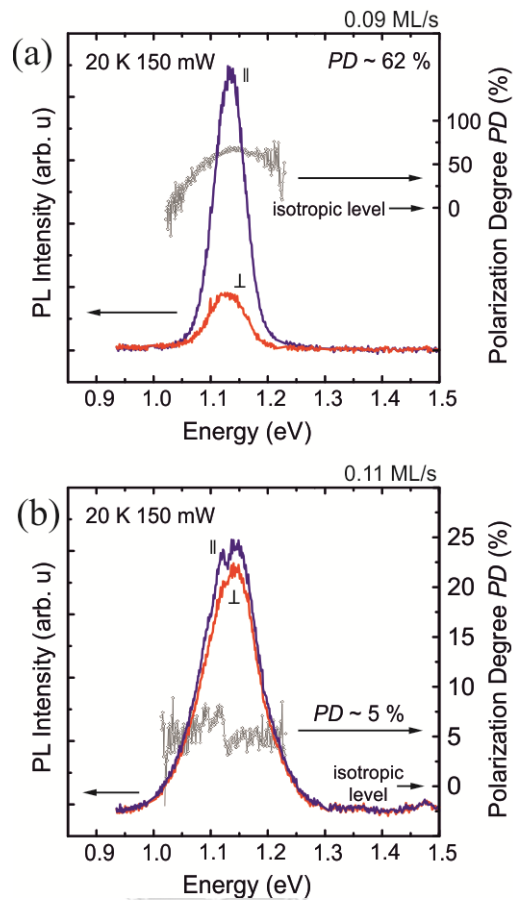
Figure 6.18 Polarization dependent PL spectra of elongated GaSb QDs grown at growth rates (a) ~0.09 ML/s, (b) ~0.11 ML/s.

In this chapter, GaSb/GaAs self-assembled QD grown on (001) Ge substrate at different growth conditions is presented. Details of the self-assembled growth by MBE in the SK growth mode are described. The elongated GaSb/GaAs QDs are realized at growth temperature 450°C with low growth rate ~0.11 ML/s. The elongated GaSb/GaAs QDs originates from orthogonal APDs. Based on these results, the effect of Ga deposition amount on GaSb/GaAs QDs is studied. The transformation of QD shape by the anisotropy Ga diffusion and strain effect corresponding to the Ga deposited amount are described. By varying the Ga growth rate, the strain relieved-QD with high polarization degree is realized at low growth rate ~0.09 ML/s. The observed PL results give the information of intermixing effect in some samples. Power dependence PL measurement shows that GaSb/GaAs QDs have the type-II band alignment characteristics.

Chapter 7
Self-Assembled InSb/GaAs Quantum Dots Grown on (001) Ge Substrates

This chapter presents the experimental results on the different growth conditions of InSb/GaAs self-assembled QDs are shown and discussed. The narrowest bandgap of 0.235eV of bulk InSb (at room temperature) and the large lattice mismatch of ~14.6% between InSb and GaAs attracts the high interesting for self-assembled InSb/GaAs QDs growth [85, 86]. The growth conditions dependent QDs morphology is presented in this work. The effect of QD growth temperature and growth rate on the positioning of QDs and the QD size, shape and density are observed.

QD nominal thickness ~2.5 ML InSb QDs at the low growth rates; 0.016 ML/s at different growth temperature, 0.09 ML/s at different growth temperatures and with different In growth rate at low temperature 300ºC are grown in this study. Sb_4 beam flux is fixed at ~5×10^{-7} torr. The series of samples are fabricated with the same growth parameters by varying QD growth temperatures; 300ºC, 350ºC and 400ºC, and In growth rate; 0.016 ML/s, 0.023 ML/s, 0.041 ML/s, 0.09 ML/s and 0.14 ML/s respectively.

The photoluminescence (PL) measurement is carried out at low temperatures 20 K by using 532-nm diode pump solid state laser (DPSSL) laser as an excitation laser source and cooled InGaAs photodetector.

7.1   QD Formation: Experiment

The 500 nm-GaAs buffer layer is grown on (001) Ge substrate at 550ºC. After the buffer layer growth, 2.5 ML of InSb QDs are deposited on the GaAs buffer layer. Then InSb QDs layer is capped by 150 nm GaAs layer in two step-growth method and upper InSb QDs layer is grown at the same growth conditions for AFM analysis. (The detailed growth procedure is described in Chapter 3).

RHEED intensity observation is performed to track the growth conditions during the growth process. Figure 7.1 (a) shows RHEED patterns reflected from GaAs buffer surface on (001) Ge substrate and the streaky RHEED patterns show that the

(2×2)-to-c(4×4) surface reconstruction of flat GaAs. As soon as the InSb QDs formulate on GaAs layer, RHEED pattern changes from the streaky patterns to spotty patterns as shown in figure 7.1 (b).

[110] azimuth   [100] azimuth
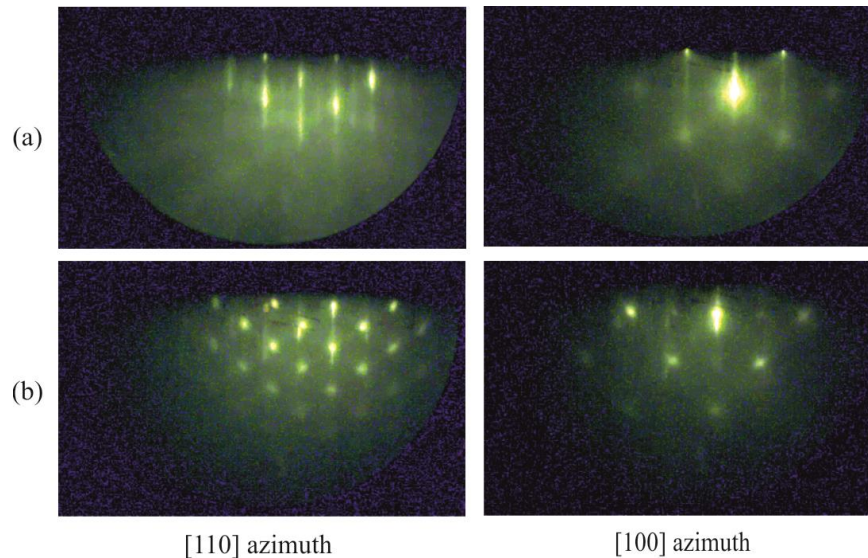
Figure 7.1 RHEED patterns recorded after the growth of (a) GaAs buffer layer on (001) Ge substrate and (b) InSb QDs on GaAs matrix layer along the [110] and [100] azimuths.

As shown in Figure 7.2, the critical QD thickness and the thickness of being grown QDs are experimentally observed by the collecting of RHEED intensities as a function of time taken. When the Sb_4 valved cracker cell is opened, RHEED intensity is recorded simultaneously. After 60 s of Sb soaking, In cell shutter is opened to deposit the QDs. After 105 s depositing of In atoms, the abrupt increasing of RHEED intensity occurs. This is because of the fully relaxation and formulation of InSb in sequence of events after wetting layer nucleation. Then In cell shutter is remain opened about 40 s more and the 2.32 ML thickness of InSb QDs are received. The critical thickness of InSb QDs at low growth rate is ~ 1.68 ML.

In this case, InSb QD is grown with low growth rate at low temperature 300ºC. The QD formation critical thickness corresponds to the RHEED transition time will be different by varying growth temperature. Because In desorption rate will be higher

by increasing growth temperature (See in Chapter 3). The critical thickness can be varied from 1.68 ML to 2 ML.
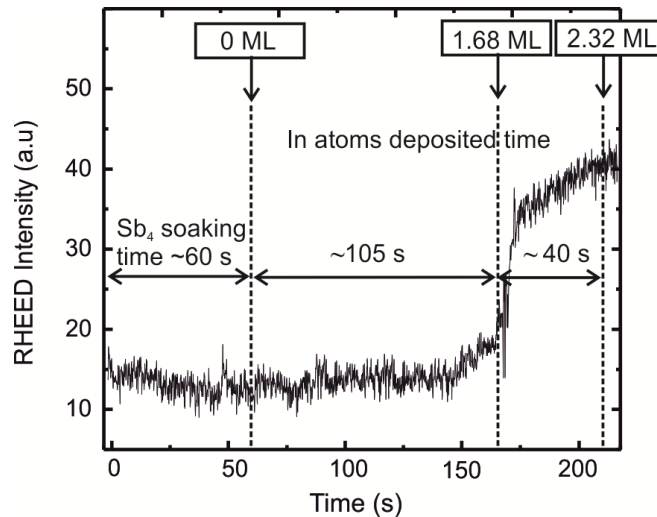
Figure 7.2 RHEED intensity as a function of time during InSb/GaAs QDs formation

7.2   Effects of Growth Temperature and Growth Rate

7.2.1 InSb/GaAs QD grown with growth rate ~0.016 ML/s at different growth temperatures

To investigate the effect of QD growth temperature on the morphology of InSb QD, the QD growth temperature is increased from 300ºC to 400ºC, and the growth rate is kept at ~0.016 ML/s. The shape transformation of QDs from rectangular-based shape to round-based shape as a function of QD growth temperature is observed. Figure 7.3 (a-c) shows the formulated InSb/GaAs QDs grown at different growth temperature. It is observed that QDs can preferably formulate in and along APBs than on the APDs surface. This can be attributed to the elimination of threading dislocations originated from the misfit strain relaxation in APDs and which lead to the In atoms deposition in and along the low strained APBs. As shown in Figures 7.3 (a, b), InSb QDs elongate and align along the APBs conducted by the [110] and [1$\bar{1}$0] crystallographic orientations of APDs at low temperatures 300ºC and 350ºC.

The 3D AFM views of InSb QDs are shown on the right of corresponding AFM images. The aligned and elongated InSb QDs along APBs meet and perpendicular to each other at the orthogonal APBs. The chains of InSb QDs form by connecting the elongated InSb QDs to each other. The chain of InSb QD can be long from 450-500 nm, and 150 nm-long single QD is also observed. It can be speculated that the nature of APBs mainly effect on the positioning of QDs, the surface morphology and the QD elongation. When the growth temperature is increased to 400ºC, QDs shape transforms from rectangular based shape to circular based dome shape in large size distribution. And also the QD density ($\sim 3.8 \times 10^8$ cm^{-2}) is relatively lower than the densities of QDs grown at 300ºC (1.9×10^9 cm^{-2}),and at 350ºC (1.4×10^9 cm^{-2}), respectively. Therefore, the density of InSb/GaAs QDs decreases as a function of the QDs growth temperature.
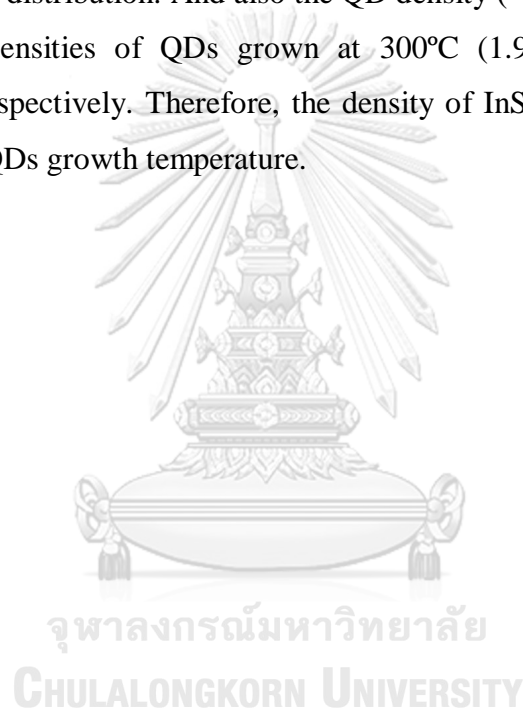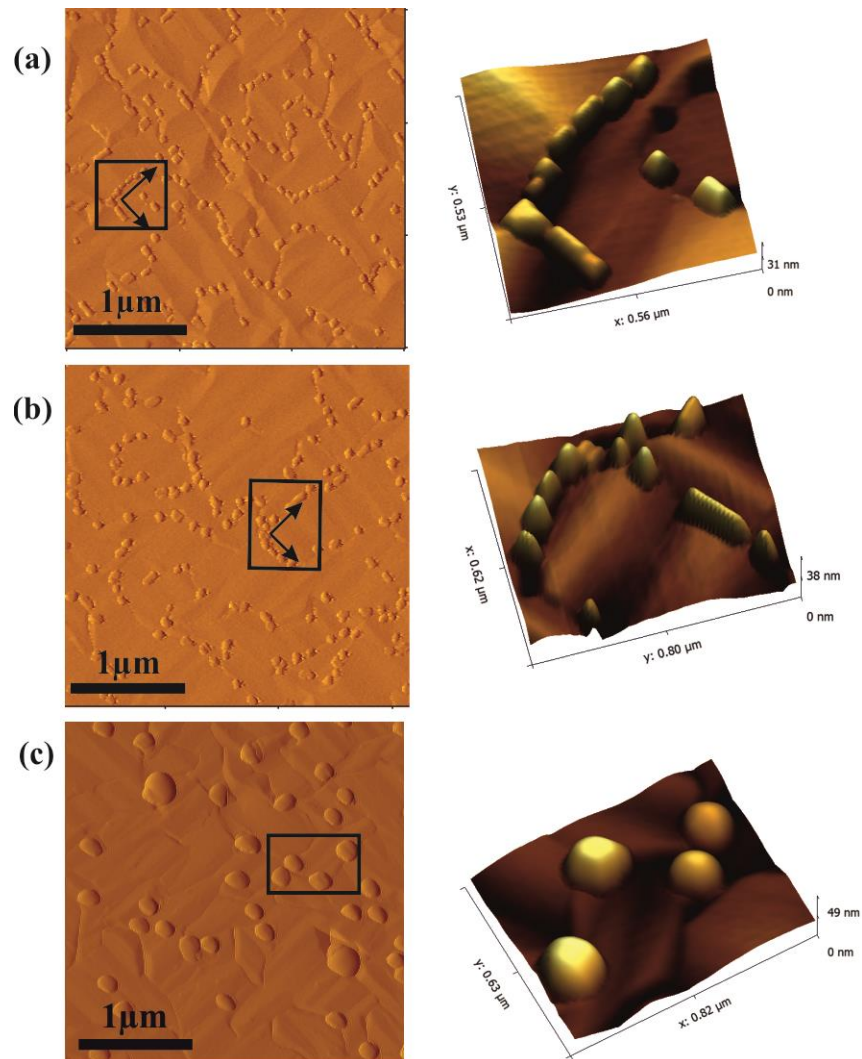
Figure 7.3 $3 \times 3 \ \mu m^2$ AFM images of InSb QDs grown at 300ºC (a), 350ºC (b) and 400ºC (c). 3D AFM images shown on the right are the highlighted areas of InSb QDs marked with the rectangular boxes in the respective AFM image.

Figures 7.4 (a-c) show the 3D AFM images of the single QDs grown at different temperatures and the characterization of respective AFM images by the facet analysis. The QD bases having irregular lens-shape are observed. In order to investigate the nanostructures of deposited QDs in different growth temperatures, the surface orientation mapping is performed. The plotted facet diagrams of respective QDs are shown on the right side of corresponding QD in Figures 7.4 (a-c). From the

facet analysis of the QD surface, it is observed that the rectangular base InSb QDs grown at 300ºC have {10n} side facets and the shape of QDs grown at 350ºC is defined by {10n} and {11n} oriented facets. At 400ºC, QDs shape completely changed to circular based dome shape. The flat (001) top surfaces are observed in QDs grown at all growth temperatures.
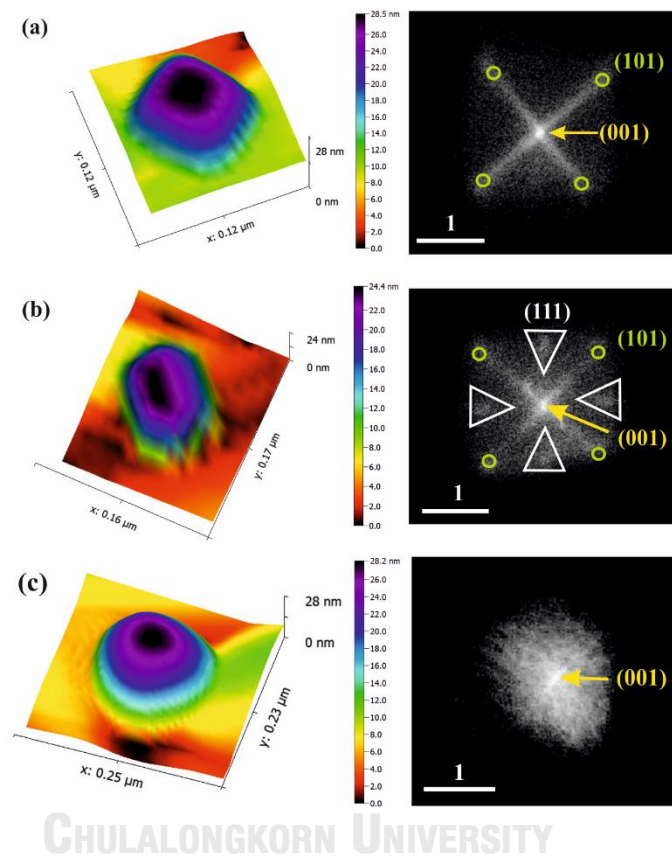
Figure 7.4 Facet plots of the InSb QDs labelling on their respective side facets grown at (a) 300ºC (b) 350ºC and (c) 400ºC, accompanied by the magnified 3D AFM images of respective QDs nanostructure [87].

Figure 7.5 shows the histograms of the QDs lengths and diameters (a-c) and those of the QDs height (d-f) at different temperatures. The extracted values of the average QD length, diameter and height are fitted by Gaussian function. It can be revealed that the average QD length/diameter and height increases by increasing

growth temperature, while the QDs density decreases as a function of growth temperature. The observed values of average QD length/diameter and height at 300ºC, 350ºC and 400ºC corresponds to 86.96 ± 17.7 nm, 98.07 ± 11.6 nm and 158.4 ± 24.9 nm, and 16.47 ± 5.57 nm, 21.54 ± 7.5 nm and 27.2 ± 4.5 nm, respectively. This trend of the nature of QD formulation agrees with the reported QD systems [88].
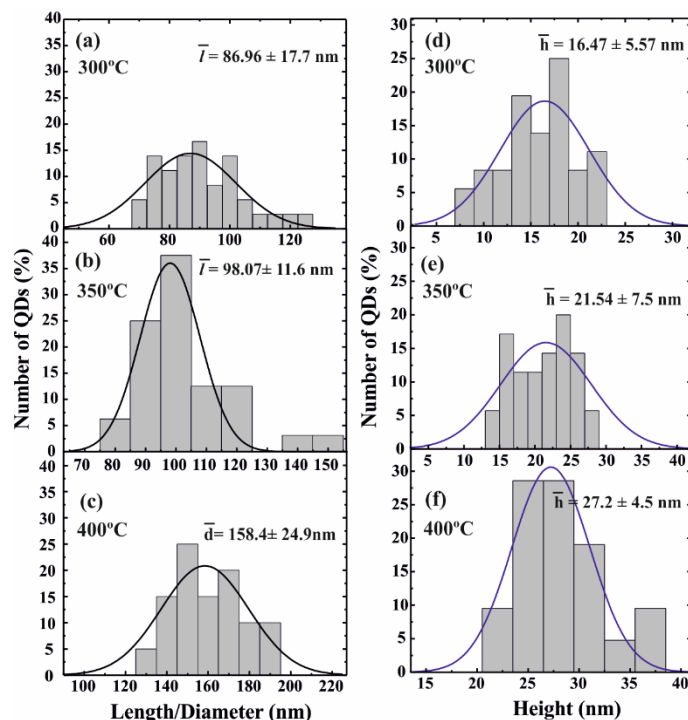
Figure 7.5 (a-f) Histograms show the distributions of InSb QDs by comparing length/diameter and height of QDs grown at 300ºC, 350ºC and 400ºC. Solid lines are Gaussian fits. Dot density, mean and standard deviation of height and length/diameter values are shown [87].

7.2.2 InSb/GaAs QD grown with growth rate ~0.09 ML/s at different growth temperatures

In order to investigate the growth rate effect related with growth temperature and the QD positioning, for this work, the substrate temperature is controlled in the range of 300ºC-400ºC (the same growth conditions as the previous work) while the InSb growth rate is increased to ~ 0.09 ML/s.

Figure 7.6 shows the 3×3 μm^2 AFM images of InSb/GaAs QDs grown at different growth temperatures. The sample surface at the highest growth temperature 400ºC, no InSb QDs form due to the high In desorption rate. For the growth at 300ºC and 350ºC, the InSb QDs densely form and align in the APBs while dilute QD array is observed on the flat surface of each boundary. This indicates that the preferential position of InSb QD formation is in the APBs. The average QD length increases from 69.72 nm to 90.62 nm, the average QD width increases from 57.41 nm to 73.3 nm, and the average QD height as well increases from 5.5 nm to 6.3 nm with increasing temperatures from 300ºC to 350ºC. Similar to other QD systems, the larger InSb QD sizes are observed when the higher growth temperature is applied.

Compare to the previous study, in this case, by increasing InSb growth rate to ~0.09 ML/s, QD can accumulate on both APDs and APBs, and the QD size is smaller. QDs connect to each other aligns along the APBs and they are smaller than those on APDs. Since one APD enlarges about area of 1 μm^2, the pathway of APB is relatively smaller leading to the QD density in APB is lower than those on APDs. When closer look on the array of these free-standing QDs, at 300ºC, QD bases likely change to circular base while the lower growth rate (~0.016 ML/s) QD shows rectangular based-shape in the previous study.
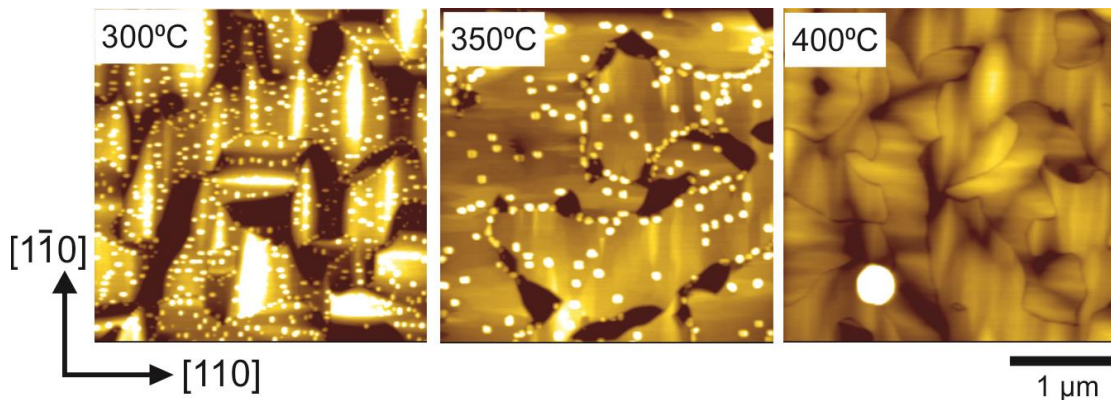
Figure 7.6 3×3 μm^2 AFM images of 2.5 ML InSb/GaAs QDs grown on Ge (001) substrate at different temperatures: 300ºC, 350ºC and 400ºC.

The low-temperature PL spectra of 2.5 ML InSb/GaAs QDs at a growth rate ~0.09 ML/s at different growth temperatures; 300ºC, 350ºC and 400ºC are shown in Figure 7.7. PL spectra are normalized by maximum peak intensity. For the QD grown at 300ºC, the PL emission occurs at ~1.21 eV for the 300ºC growth InSb/GaAs layer and at ~1.3 eV for the 350ºC growth InSb/GaAs layer. For 400ºC growth QD, the peak is observed at 1.3 eV also, and therefore, we attribute that the peaks are emitted mainly from InSb/GaAs ($In_xGa_{1-x}Sb_yAs_{1-y}$) layer by means of anion exchange reaction during QD growth. On the other hand, PL measurements are carried out in the wavelength range of 800–1600 nm by using LN_2 cooled InGaAs detector. Therefore, the QD emission PL range (1.2 μm–1.4 μm) [89] is beyond the available detecting range of InGaAs detector. By increasing the growth temperature, a blue shift of PL peak from 1.21 eV (300ºC) to 1.3 eV (350ºC & 400ºC) is observed. This can be due to the high In desorption rate at high growth temperature which results the different material composition amount in grown InSb/GaAs. At 300ºC, InSb peak intensity is strong and GaAs peak cannot be seen. At 350ºC, InSb peak intensity is smaller and GaAs peaks appear, and GaAs peak is stronger than InSb at 400ºC.
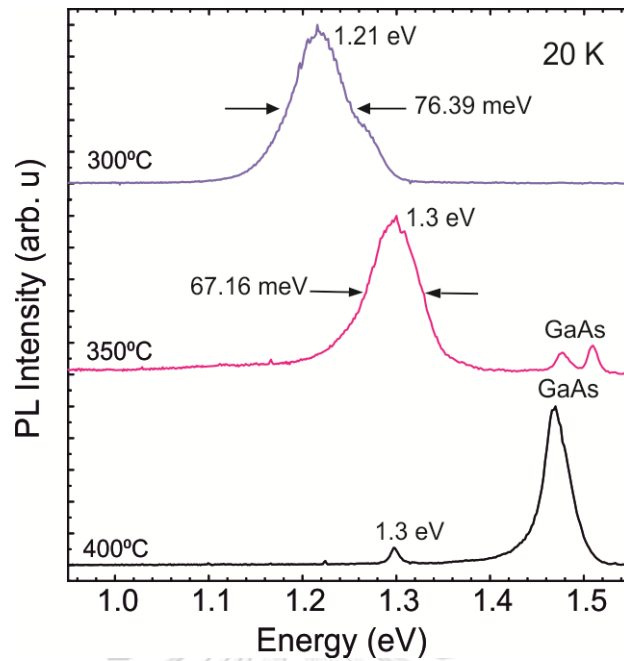
Figure 7.7 Normalized PL spectra of 2.5 ML InSb/GaAs QDs grown at different growth temperature with low growth rate ~0.09 ML/s. The excitation power is 150 mW.

7.2.3 InSb/GaAs QD grown with different growth rate at low growth temperature 300°C

The InSb growth rate effect on the InSb/GaAs QD morphologies corresponding to the QD size, shape and local growth position are studied. The In growth rate is increased form ~ 0.023 ML/s to 0.041 ML/s, 0.09 ML/s and 0.14 ML/s while the substrate temperature is fixed at 300°C. For all samples growths, the constant Sb_4 flux ~ 5×10^{-7} torr is used.

When the growth rate is varied, the observed InSb/GaAs QD morphologies are considerably changed. Figure 7.8 show AFM images of InSb/GaAs QDs grown at different growth rates. At low growth rates of 0.023 and 0.041 ML/s, the InSb/GaAs QDs are formed only in the APBs while the QDs grown with higher growth rates of 0.09 and 0.14 ML/s, accumulate on both APDs and APBs result the high density InSb/GaAs QDs. At the growth rate of 0.14 ML/s, the array of high density InSb QDs (~ 1.01×10^{10} cm^{-2}) is obtained. Interestingly, the QD size and shape are very different for the QDs in APBs as compared with the QDs on the flat GaAs APDs. Figures 7.9

(a-c) show the variations of QDs lateral size, height and dot density as a function of In growth rate. According to the AFM results, accumulated QDs are separated into two groups; QDs on APDs and QDs in APBs. By increasing the In growth rate, the sizes and height of QDs in APBs are smaller, and such QD formulation nature can be found in all four samples. The density of QDs in APBs increases and QDs occupy the whole area of APBs. At higher growth rates; 0.09 ML/s and 0.14 ML/s, QD can be deposited both on APD and in APBs, and the density increases as well. The QDs grown at ~0.14 ML/s has smaller QD size with higher QD density than those grown at ~0.09 ML/s.

Generic growth scenarios for the self-assembled QD growth on surface decorated with APD as well as the roles of growth rate and local growth position on the material diffusion on the material diffusion (Figure 7.10) are developed based on this experiment.
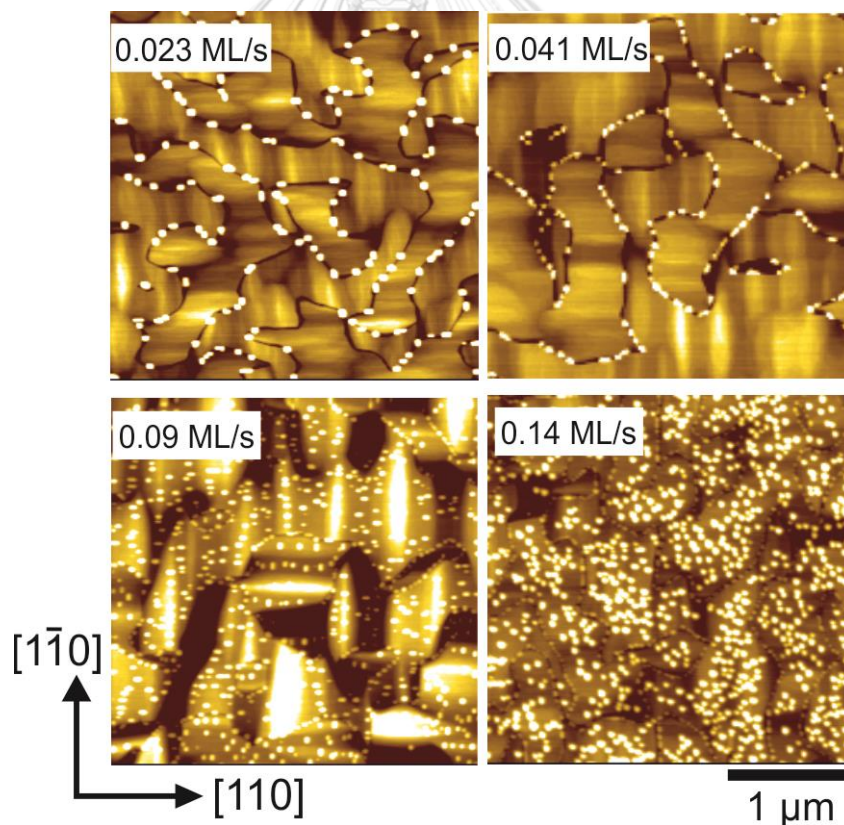
Figure 7.8 3×3 μm^2 AFM images of 2.5 ML InSb/GaAs QDs grown on Ge (001) substrate at different In growth rate; 0.024 ML/s, 0.041 ML/s, 0.09 ML/s and 0.14 ML/s at growth temperature 300ºC.
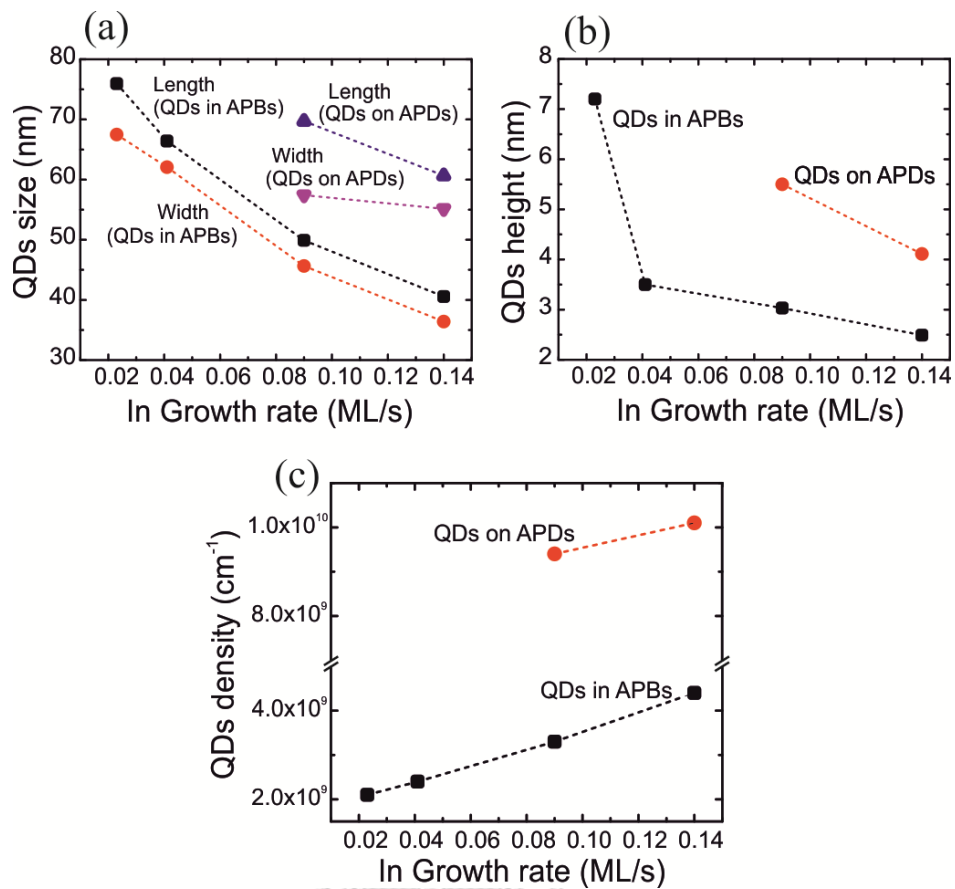
Figure 7.9 Dependence of InSb QDs (a) size , (b) height and (c) density on various In growth rate; 0.024 ML/s, 0.041 ML/s, 0.09 ML/s and 0.14 ML/s. At higher growth rates; 0.09 ML/s and 0.014 ML/s, the array of high density InSb QDs are obtained both on APDs and in APD boundaries (APBs).
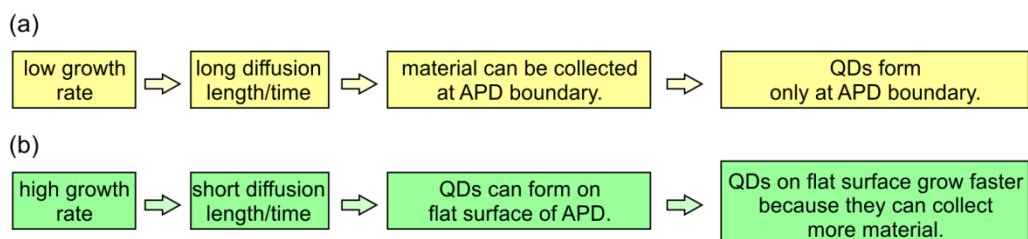
Figure 7.10 Generic scenarios for describing the self-assembled QD growth on the surface decorated with APDs: In case of (a) low growth rate and (b) high growth rate.

The normalized PL spectra of 2.5 ML InSb/GaAs at the different In growth rate; 0.023 ML/s, 0.041 ML/s, 0.09 ML/s and 0.14 ML/s are shown in Figure 7.11. The excitation power is 150 mW. Although the PL peak energy position is nearly the same and no PL peak shift is observed, the emission peak energy of InSb/GaAs is very well consistent with the reported vale range of 1-1.2 eV [19].
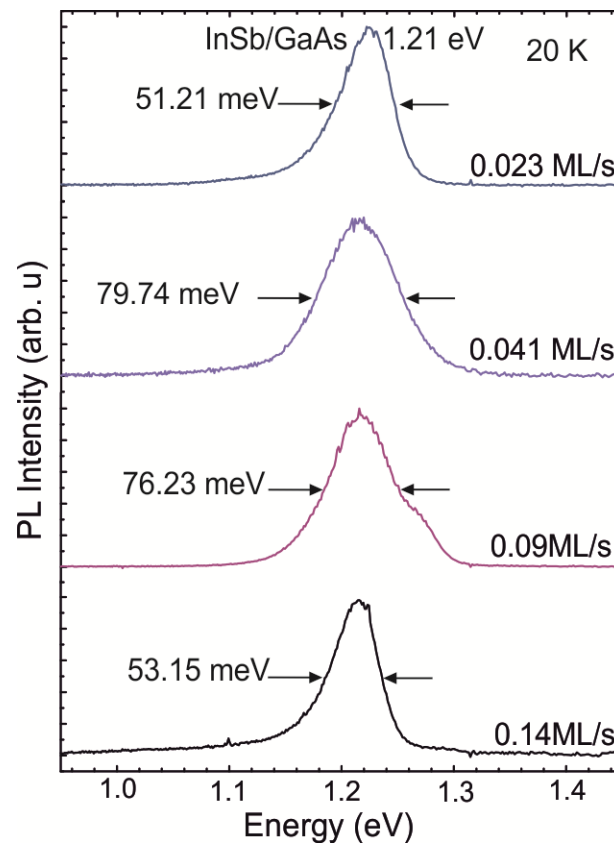
Figure 7.11 Normalized PL spectra of InSb/GaAs QDs samples grown with different growth rates at growth temperature 300ºC. The excitation power is 150 mW.

This chapter presents the effects of QDs growth temperature and In growth rate on the morphologies and structural properties of InSb/GaAs QDs grown on (001) Ge substrate. The preferential formation of QD is the APB due to the mismatch strain in this material system. By changing the QD growth temperature and growth rate, the QD shape, size, density and local positioning can be varied.

For the QDs grown with different growth rates, QD size and shape are affected strongly by In growth rate. By using very low growth rate, the large and rectangular based-shape QD are formed in the APBs. This is because In atoms having longer diffusion length/time can deposit more in low strained APBs. RHEED intensities are recorded to observe experimentally the critical thickness of InSb and to track the QDs formation process. By using different growth conditions; temperature dependence and growth rate dependence, the critical thickness of InSb can vary in the range of 1.68-2 ML.
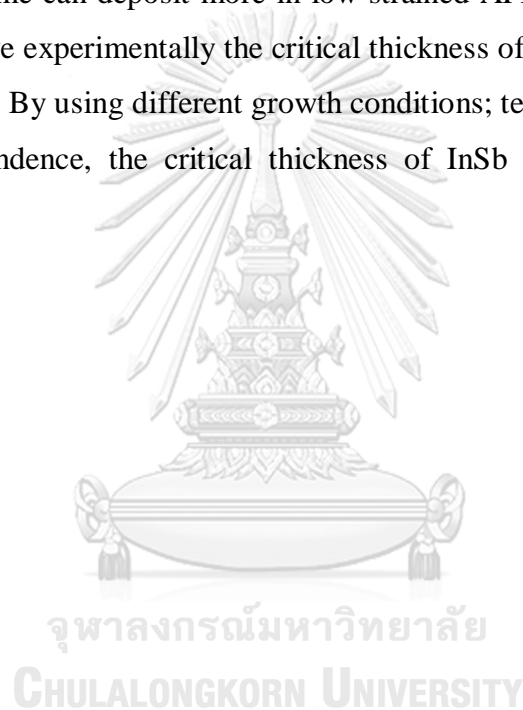
Chapter 8

Conclusions

This work presents the growth of GaSb/GaAs and InSb/GaAs nanostructures on (001) Ge substrates by MBE in the SK growth mode. The QDs morphologies and optical properties are characterized by *ex situ* AFM, Raman and PL. Calibration of substrate temperature, the growth rates, and the QD formulation process are monitored by *in situ* RHEED observations.

GaSb/GaAs QDs and InSb/GaAs QDs are successfully grown on APDs decorated GaAs layer by using (001) Ge substrates. The flat APDs layer is achieved at low V/III (As/Ga) ratio ~10 at growth temperature 550ºC. The orthogonal APDs and APBs play the main role in the QDs formulating and positioning in both types of QDs system.

Effects of various growth parameters on GaSb/GaAs and InSb/GaAs QDs systems are studied. The growth of GaSb/GaAs self-assembled QD at different growth conditions is divided into three sections: growth temperature dependence, Ga deposited amount dependence and Ga growth rate dependence.

By increasing growth temperature from 400ºC to 500ºC, larger QD and lower QD density are realized. The QD growth temperature strongly affects the low growth rate (Ga growth rate ~0.11 ML/s) GaSb/GaAs QD shape and size distribution. At growth temperature 450ºC, the elongated GaSb/GaAs QDs originates from different APDs which rotate perpendicular to each other. The self-assembled GaSb QD shape transforms from circular based shape to rectangular based shape by GaSb depositing over 2.5 ML.

Effects of Ga growth rate on the GaSb/GaAs QD shape and size are studied. The growth rate dependent QD morphology is observed. At high growth rate, small and circular based-shape QDs can be deposited. By reducing growth rate, large and rectangular based-shape QDs are realized. The increment of anisotropic GaSb QD can be obtained at relatively low growth rate.

Therefore, one can conclude that the elongated GaSb/GaAs QD along [110] direction can be obtained after QD depositing over 2.5 ML with low growth rates ~0.11 ML/s and 0.09 ML/s at growth temperature 450ºC. The emitted PL peaks of

GaSb QDs grown with different growth conditions agree with the AFM results. The PL emission from QDs exhibits a strong blue shift with increasing the excitation power, which is the characteristic of type-II band alignment. Strain-induced peak energy redshift of GaSb grown by reducing Ga growth rate is found by Raman scattering spectroscopy.   Finally, the elongated GaSb/GaAs QDs having large polarization degree *PD* ~62% is observed.at low rate growth ~0.09 ML/s.

We realize the influences of QD growth temperature and In growth rate on the morphologies of self-assembled InSb/GaAs QDs grown on (001) Ge substrate. The APDs and APBs formation affects the QD positioning and orientated InSb QDs elongation which can be visually observed by AFM. The two main themes can be concluded for InSb QDs growth are;

1.   APBs become the important role in the growth of InSb QDs. Low-growth-rate InSb QDs can localize in APBs and elongate along with the APDs directions; [110] and [$1\bar{1}0$], by the guidance of APBs while InSb QDs grown at high growth rate form on flat GaAs APDs.

2.   The effect of growth temperature and growth rate can highly control the QDs shape, size and density. QD size and shape are affected strongly by In growth rate. By using very low growth rate, the large and rectangular based-shape QD are formed in the APBs because In atoms having longer diffusion length/time can deposit more in low strained APBs. We attribute the preferential formation of QD at the APB to the mismatch strain in this material system. By changing the QD growth temperature, the QD density can be varied. The average QD size (both height and length/diameter) decreases when the growth temperature reduced.

By comparing the GaSb/GaAs and InSb/GaAs QDs systems, the GaSb/GaAs QD positioning depends on the QDs growth temperature while the InSb/GaAs QD positioning depends on the growth rate. By increasing the growth temperature at low growth rate, GaSb/GaAs QDs shape transforms from circular based shape to rectangular based shape whereas InSb/GaAs QDs shape transforms from rectangular based shape to circular based shape.

The generic scenarios for describing the self-assembled GaSb/GaAs and InSb/GaAs QDs growth on the surface decorated with APDs corresponding to the different growth conditions are developed based on this dissertation.

REFERENCES

1. Arakawa, Y., and Sakaki, H., *Multidimentional quantum well laser and temperature dependence of its threshold current.* Applied Physics Letters, 1982. **40**(11): p. 939-941.

2. Bennett, B.R., et al., *Molecular beam epitaxial growth of InSb, GaSb and AlSb nanometer-scale dots on GaAs.* Applied Physics Letters, 1996. **68**(4): p. 505-507.

3. Chia, C.K., et al., *Role of AlxGa1-xAs buffer layer in heterogeneous integration of GaAs/Ge.* Journal of Applied Physics, 2011. **109**: p. 066106-1-066106-3.

4. Fang, S.F., et al., *Gallium arsenide and other compound semiconductors on silicon.* Journal of Applied Physics, 1990. **68**(7): p. R31-R58.

5. Banerjee, S., et al., *Stranski–Krastanow growth of multilayer In(Ga)As/GaAs QDs on Germanium substrate.* Applied Physics A, 2010. **99**: p. 791-795.

6. Holt, D.B., et al., *Properties and structure of antiphase boundaries in GaAs/Ge solar cells.* Materials Science and Engineering, 1996. **B42**: p. 204-207.

7. Okumura, H., et. al., *Carbon contamination free Ge(100) surface cleaning for MBE.* Applied Surface Science, 1998. **125**: p. 125-128.

8. Li, W., et al., *Growth of device-quality GaAs layer directly on (001) Ge substrates by both solid-source and gas-source MBE.* Journal of Crystal Growth, 2001. **227-228**: p. 104-107.

9. Rogalski, A., *Recent progress in infrared detector technologies.* Infrared Physics & Technology, 2011. **54**(3): p. 136-154.

10. Downs, C., and Vandervelde, T. E., *Progress in infrared photodetectors since 2000.* Sensors (Basel), 2013. **13**(4): p. 5054-5098.

11. Razeghi, M., et al., *Advances in antimonide-based Type-II superlattices for infrared detection and imaging at center for quantum devices.* Infrared Physics & Technology, 2013. **59**: p. 41-52.

12. Tantiweerasophon, W., et al., *Self-assembled InAs quantum dots on anti-phase domains of GaAs on Ge substrates.* Journal of Crystal Growth, 2011. **323**(1): p. 254-258.

13. Songmuang, R., et al., *Photoluminescence investigation of low-temperature capped self-assembled InAs/GaAs quantum dots.* Journal of Crystal Growth, 2003. **251**(1-4): p. 166-171.

14. Thongkamkoon, N., et al., *Bimodal optical characteristics of lateral InGaAs quantum dot molecules.* Journal of Crystal Growth, 2011. **323**(1): p. 206-210.

15. Hayne, M., et al., *The structural, electronic and optical properties of GaSb/GaAs nanostructures for charge-based memory.* Journal of Physics D: Applied Physics, 2013. **46**(26): p. 264001 (10pp).

16. Yamaguchi, K., et al., *Chapter 8-GaSb/GaAs quantum nanostructures by molecular beam epitaxy.* Handbook of self assembled semiconductor nanostructures for novel devices in photoincs and electronics, 2008(Z. Wang (Ed.)): p. 271-292.

17. Xu, F., et al., *Enhanced performance of quantum dot solar cells based on type II quantum dots.* Journal of Applied Physics, 2014. **116**(13): p. 133102-1-133102-5

18. Tatebayashi, J., et al., *Formation and optical characteristics of type-II strain-relieved GaSb/GaAs quantum dots by using an interfacial misfit growth mode.* IEEE Transactions on Nanotechnology, 2009. **8**(2): p. 269-274.

19. Bennett, B.R., et al., *Self-assembled InSb and GaSb quantum dots on GaAs (001).* Journal of Vacuum Science & Technology B: Microelectronics and Nanometer Structures, 1996. **14**(3): p. 2195-2198.

20. Bennett, B.R., et al., *Composition and strain of self-assembled (In,Ga,Al)Sb/(Ga,Al)As quantum dots.* Superlattices and Microstructures, 1997. **21**(2): p. 267-272.

21. Zon, et al., *Investigation of GaSb/GaAs quantum dots formation on Ge (001) substrate and effect of anti-phase domains.* MRS Advances, 2016. **1**(23): p. 1729-1734.

22. Ringel, S.A., et al., *Anti-phase domain-free GaAs on Ge substrates grown by molecular beam epitaxy for space solar cell applications.* 26th IEEE Photovoltaic Specialists Conference-1997, 1997: p. 793-798.

23. Li, Y., et al., *On the formation of antiphase domains in the system of GaAs on Ge.* Journal of Crystal Growth, 1996. **163**: p. 195-202.

24. Zon, et al., *Raman and photoluminescence properties of type II GaSb/GaAs quantum dots on (001) Ge substrate.* Electronic Materials Letters, 2016. **12**(4): p. 517-523.

25. Li, Y., et al., *On the sublattice location of GaAs grown on Ge.* Journal of Applied Physics, 1994. **76**(10): p. 5748-5753.

26. Bimberg, D., et al., *Quantum dot heterostructures.* Chichester: Wiley, 1999: p. 339.

27. Sugawara, M., *Chapter 1-Theoretical bases of the optical properties of semiconductor quantum nano-structures.* Semiconductors and Semimetals, 1999. **60**: p. 1-116.

28. Gilmer, G.H., and Grabow, M. H., *Models of thin film growth modes.* Journal of Metals, 1987: p. 19-23.

29. Herman, M.A., et al., *Epitaxy: Physical Principles and Technical Implementation.* Berlin: Spinger-Verlag, 2004: p. 507.

30. Rogalski, A., *Competitive technologies of third generation infrared photon detectors.* Opto-Electronics Review, 2006. **14**(1): p. 87-101.

31. Müller-Kirsch, L., et al., *Many-particle effects in type II quantum dots.* Applied Physics Letters, 2001. **78**(10): p. 1418-1420.

32. Glaser, E.R., et al., *Photoluminescence studies of self-assembled InSb, GaSb and AlSb quantum dot heterostructures.* Applied Physics Letters, 1996. **68**(25): p. 3614-3616.

33. Hatami, F., et al., *Radiative recombination in type-II GaSb/GaAs quantum dots.* Applied Physics Letters, 1995. **67**(5): p. 656-658.

34. Suzuki, K., et al., *Structural and optical properties of type II GaSb/GaAs self-assembled quantum dots grown by molecular beam epitaxy.* Journal of Applied Physics, 1999. **85**(12): p. 8349-8352.

35. Qiu, F., et al., *An investigation of exciton behavior in type-II self-assembled GaSb/GaAs quantum dots.* Nanotechnology, 2016. **27**(6): p. 065602 (6pp).

36. Kunrugsa, M., et al., *Molecular beam epitaxial growth of GaSb/GaAs quantum dots on Ge substrates.* Journal of Crystal Growth, 2014. **401**: p. 441-444.

37. Sieg, R.M., et al., *Anti-phase domain-free growth of GaAs on offcut (001) Ge wafers by molecular beam epitaxy with suppressed Ge outdiffusion.* Journal of Electronic Materials, 1998. **27**(7): p. 900-907.

38. Kittel, C., *Introduction to solid state physics.* New York: Wiley, 1996. **7th (Ed.)**: p. p. 689.

39. Herman, M.A., and Sitter, H., *Molecular beam epitaxy: Fundamentals and current status.* Berlin: Spinger-Verlag, 1989: p. 393.

40. Dabrowska-Szata, M., *Analysis of RHEED pattern from semiconductor surfaces.* Materials Chemistry and Physics, 2003. **81**(2-3): p. 257-259.

41. LaBella, V.P., et al., *Atomic structure of the GaAs(001)-(2×4) surface resolved using scanning tunneling microscopy and first-principles theory.* Physical Review Letters, 1999. **83**(15): p. 2989-2992.

42. Ichimiya, A., and Cohen, P. I., *Reflection high energy electron diffraction.* Cambridge: Cambridge University press, 2004: p. 350.

43. Ohring, M., *The Materials Science of Thin Films.* Academic Press. New York: Boston, 1992.

44. Shchukin, V.A., and Bimberg, D., *Spontaneous ordering of nanostructures on crystal surfaces.* Reviews of Modern Physics, 1999. **71**: p. 1125-1171.

45. Bennett, B.R., et al., *Stranski-Krastanov growth of InSb, GaSb, and AlSb on GaAs: structure of the wetting layers.* Journal of Crystal Growth, 1997. **175/176**: p. 888-893.

46. Kiravittaya, S., et al., *Advanced quantum dot configurations.* Reports on Progress in Physics, 2009. **72**: p. 046502 (34pp).

47. Richter, J., et al., *GaSb quantum dots on GaAs with high localization energy of 710 meV and an emission wavelength of 1.3 μm.* Journal of Crystal Growth, 2014. **404**: p. 48-53.

48. Geller, M., et al., *450 meV hole localization in GaSb/GaAs quantum dots.* Applied Physics Letters, 2003. **82**(16): p. 2706-2708.

49. Sun, C.-K., et al., *Optical investigaions of the dynamic behavior of GaSb/GaAs quantum dots.* Applied Physics Letters, 1996. **68**(11): p. 1543-1545.

50. Ramiro, I., et al., *Analysis of the intermediate-band absorption properties of type-II GaSb/GaAs quantum-dot photovoltaics.* Physical Review B, 2017. **96**(12): p. 125422-1-125422-13.

51. Ferrini, R., et al., *Interband optical properties of molecular-beam epitaxially grown GaAs1−xSbx on GaAs substrates.* Journal of Applied Physics, 1999. **86**(8): p. 4706-4708.

52. Nakai, T., et al., *Control of GaSb/GaAs quantum nanostructures by molecular beam epitaxy.* Japanese Journal of Applied Physics, 2004. **43**(4B): p. 2122-2124.

53.	Jiang, C., et al., *Sb/As intermixing in self-assembled GaSb/GaAs type II quantum dot systems and control of their photoluminescence spectra.* Physica E: Low-dimensional Systems and Nanostructures, 2005. **26**(1-4): p. 180-184.

54.	Grundmann, M., et al., *Ultranarrow luminescence lines from single quantum dots.* Physical Review Letters, 1995. **74**(20): p. 4043-4046.

55.	Bosi, M., and Attolini, G., *Germanium: Epitaxy and its applications.* Progress in Crystal Growth and Characterization of Materials, 2010. **56**(3-4): p. 146-174.

56.	Lazzarini, L., et al., *Antiphase disorder in GaAs/Ge heterostructures for solar cells.* Micron, 2000. **31**: p. 217-222.

57.	Bosi, M., et al., *Effect of temperature on the mutual diffusion of Ge/GaAs and GaAs/Ge.* Journal of Crystal Growth, 2011. **318**(1): p. 367-371.

58.	Agarwal, S.K., et al., *Effect of growth parameters on the MOVPE of GaAs/Ge for solar cell applications.* Solar Energy Materials & Solar Cells, 1999. **59**: p. 19-26.

59.	Wanarattikan, P., et al., *Influences of two-step growth and off-angle Ge substrate on crystalline quality of GaAs buffer layers grown by MOVPE.* Journal of Crystal Growth, 2015. **414**: p. 15-20.

60.	Kohen, D., et al., *The role of AsH3 partial pressure on anti-phase boundary in GaAs-on-Ge grown by MOCVD – Application to a 200 mm GaAs virtual substrate.* Journal of Crystal Growth, 2015. **421**: p. 58-65.

61.	Horikoshi, Y., et al., *Growth process of III-V compound semiconductors by migration-enhanced epitaxy.* Journal of Crystal Growth, 1990. **105**: p. 326-338.

62.	Oh, J., et al., *Thermal desorption of Ge native oxides and loss of Ge from the surface.* Materials Science in Semiconductor Processing, 2010. **13**(3): p. 185-188.

63.	Regiński, K., et al., , *Static phase diagrams of reconstructions for MBE-grown GaAs (001) and AlAs (001) surfaces.* Thin Solid Films, 1995. **267**: p. 54-57.

64.	Smakman, E.P., et al., *GaSb/GaAs quantum dot formation and demolition studied with cross-sectional scanning tunneling microscopy.* Applied Physics Letters, 2012. **100**(14): p. 142116.

65.	Ito, A., et al., *MicroRaman study on GaAs layers directly grown on (100) Si by molecular beam epitaxy.* Journal of Applied Physics, 1992. **72**(6): p. 2531-2533.

66.	Suzuki, K., and Arakawa, Y., *Growth of stacked GaSb/GaAs self-assembled quantum dots by molecular beam epitaxy.* Journal of Crystal Growth, 1999. **201/202**: p. 1205-1208.

67.	Hatami, F., et al., *Carrier dynamics in type-II GaSb/GaAs quantum dots.* Physical Review B, 1998. **57**(8): p. 4635-4641.

68.	Mahajumi, A.-S., et al., *Rapid thermal annealing and photoluminescence of type-II GaSb single monolayer quantum dot stacks.* Journal of Physics D: Applied Physics, 2013. **46**(30): p. 305104.

69.	Alonso-Álvarez, D., et al., *Optical investigation of type II GaSb/GaAs self-assembled quantum dots.* Applied Physics Letters, 2007. **91**(26): p. 263103.

70. Tang, D., et al., *Investigation of single-layer/multilayer self-assembled InAs quantum dots on GaAs1-xSbx/GaAs composite substrates.* Journal of Applied Physics, 2015. **118**(9): p. 094303.

71. He, J., et al., *Capping effect of GaAsSb and InGaAsSb on the structural and optical properties of type II GaSb/GaAs quantum dots.* Applied Physics Letters, 2012. **100**(17): p. 171914.

72. Farad, S., et al., *Temperature effects on the radiative recombination in self-assembled quantum dots.* Surface Science, 1996. **361/362**: p. 778-782.

73. Kawazu, T., et al., *Optical properties of GaSb/GaAs type-II quantum dots grown by droplet epitaxy.* Applied Physics Letters, 2009. **94**(8): p. 081911.

74. Kawazu, T., et al., *Thermal annealing of GaSb quantum dots in GaAs formed by droplet epitaxy.* Physica E: Low-dimensional Systems and Nanostructures, 2010. **42**(10): p. 2742-2744.

75. Yin, H., et al., *Temperature effect of activation energy for GaSb quantum dots using variable temperature photoluminescence.* Journal of Nanoscience and Nanotechnology, 2013. **13**(2): p. 1022-1025.

76. Suzuki, K., et al., *Density control of GaSb/GaAs self-assembled quantum dots (~25nm) grown by molecular beam epitaxy.* Japanese Journal of Applied Physics, 1998. **37**: p. L203-L205.

77. Hogg, R.A., et al., *Optical spectroscopy of self-assembled type II GaSb/GaAs quantum dot structures grown by molecular beam epitaxy.* Applied Physics Letters, 1998. **72**(22): p. 2856-2858.

78. Balakrishnan, G., et al., *III/V ratio based selectivity between strained Stranski-Krastanov and strain-free GaSb quantum dots on GaAs.* Applied Physics Letters, 2006. **89**(16): p. 161104.

79. Jiang, C., et al., *Molecular beam epitaxial growth of very large lateral anisotropic GaSb/GaAs quantum dots.* Journal of Crystal Growth, 2007. **301-302**: p. 828-832.

80. Jiang, C., and Sakaki, H., *Controlling anisotropy of GaSb(As)/GaAs quantum dots by self-assembled molecular beam epitaxy.* Physica E: Low-dimensional Systems and Nanostructures, 2006. **32**(1-2): p. 17-20.

81. Tseng, C.-C., et al., *Influence of As on the morphologies and optical characteristics of GaSb/GaAs quantum dots.* IEEE Journal of Quantum Electronics, 2011. **47**(3): p. 335-339.

82. Kamarudin, M.A., et al., *GaSb quantum dot morphology for different growth temperatures and the dissolution effect of the GaAs capping layer.* Journal of Physics D: Applied Physics, 2010. **43**(6): p. 065402 (5pp).

83. Liang, B., et al., *GaSb/GaAs type-II quantum dots grown by droplet epitaxy.* Nanotechnology, 2009. **20**(45): p. 455604 (4pp).

84. Klenovský, P., et al., *Polarization anisotropy of the emission from type-II quantum dots.* Physical Review B, 2015. **92**(24): p. 241302-1-241302-5.

85. Vurgaftman, I., et al., *Band parameters for III–V compound semiconductors and their alloys.* Journal of Applied Physics, 2001. **89**(11): p. 5815-5875.

86. Sato, T., et al., *Dislocation-limited electron transport in InSb grown on GaAs(001).* Physica B: Condensed Matter, 2006. **376-377**: p. 579-582.

87. Zon, et al., *Morphology of self-assembled InSb/GaAs quantum dots on Ge substrate.* Journal of Crystal Growth, 2017. **468**: p. 541-546.

88.   Stangl, J., et al., *Structural properties of self-organized semiconductor nanostructures.* Reviews of Modern Physics, 2004. **76**: p. 725-783.
89.   Aissat, A., et al., *Electrical and optical properties of InSb/GaAs QDSC for photovoltaic.* International Journal of Hydrogen Energy, 2017. **42**(30): p. 19518-19524.

APPENDIX

List of Publications

International Journals and International Conferences

1.   **Zon**, Thanavorn Poempool, Suwit Kiravittaya, Suwat Sopitpan, Supachok Thainoi, Songphol Kanjanachuchai, Somchai Ratanathammaphan and Somsak Panyakeow, "Investigation of GaSb/GaAs Quantum Dots Formation on Ge (001) Substrate and Effect of Anti Phase Domains", *MRS Advances* 1, 1729 – 1734 (2016).

2.   Thanavorn Poempool, **Zon**, Suwit Kiravittaya, Suwat Sopitpan, Supachok Thainoi, Songphol Kanjanachuchai, Somchai Ratanathammaphan and Somsak Panyakeow, "GaSb and InSb Quantum Nanostructures :Morphologies and Optical Properties", *MRS Advances* 1, 1677 – 1682 (2016).

3.   **Zon**, Thanavorn Poempool, Suwit Kiravittaya, Noppadon Nuntawong, Suwat Sopitpan, Supachok Thainoi, Songphol Kanjanachuchai, Somchai Ratanathammaphan and Somsak Panyakeow, "Raman and photoluminescence properties of type II GaSb/GaAs quantum dots on (001) Ge substrate", *Electronic Materials Letters* 12, 517-523 (2016).

4.   **Zon**, Thanavorn Poempool, Suwit Kiravittaya, Suwat Sopitpan, Supachok Thainoi, Songphol Kanjanachuchai, Somchai Ratanathammaphan, Somsak Panyakeow, "Morphology of self-assembled InSb/GaAs quantum dots on Ge substrate", *Journal of Crystal Growth* 468, 541 – 546 (2017).

5.   Supachok Thainoi, Suwit Kiravittaya, Thanavorn Poempool, **Zon**, Suwat Sopitpan, Songphol Kanjanachuchai, Somchai Ratanathammaphan, Somsak Panyakeow, "Growth of truncated pyramidal InSb nanostructures on GaAs substrate", *Journal of Crystal Growth* 468, 737 – 739 (2017).

6.   Supachok Thainoi, Suwit Kiravittaya, Thanavorn Poempool, **Zon**, Noppadon Nuntawong Suwat Sopitpan, Songphol Kanjanachuchai, Somchai Ratanathammaphan, Somsak Panyakeow, "Molecular beam epitaxial growth of InSb/GaAs quantum nanostructures", *Journal of Crystal Growth* 477, 30-33 (2017).

International Conference Proceedings

1. **Zon**, T. Poempool, P .Prongjit, S .S .Han, S .Kiravittaya, S .Sopitpan, S .Thainoi, S .Kanjanachuchai, S .Ratanathammaphan and S .Panyakeow, Growth Mechanism of Type II GaSb/GaAs Quantum Dots on (001) Ge Substrates, Abstract Book of 8th AUN/SEED-NET International Conference on EEE, Manila, Philippines, November 16th-17th, 2015 (2015).

2. **Zon**, Thanavorn Poempool, Suwit Kiravittaya, Supachok Thainoi, Songphol Kanjanachuchai, Somchai Ratanathammaphan and Somsak Panyakeow, GaSb/GaAs Quantum Dots grown on Ge (001) Substrate, Abstract Book of the 25th International Photovoltaic Science & Engineering Conference (PVSEC-25) Global Photovoltaic Conference (GPVC), Busan, Korea November 15th-20th, 2015 (2015).

3. **Zon**, Thanavorn Poempool, Suwit Kiravittaya, Supachok Thainoi, Songphol Kanjanachuchai, Somchai Ratanathammaphan and Somsak Panyakeow, Investigation of GaSb/GaAs Quantum Dots Formation on Ge (001) Substrate and Effect of Anti-Phase Domains, Abstract Book of the 2015 MRS Fall Meeting & Exhibit, 29th Nov-4th Dec, 2015 (2015).

4. Thanavorn Poempool, **Zon**, Suwit Kiravittaya, Suwat Sopitpan, Supachok Thainoi,Songphol Kanjanachuchai, Somchai Ratanathammaphan, and Somsak Panyakeow, GaSb and InSb Quantum Nanostructures :Morphologies and Optical Properties, Abstract Book of the 2015 MRS Fall Meeting & Exhibit, 29th Nov – 4th Dec, 2015 (2015).

5. Thanavorn Poempool, **Zon**, Suwit Kiravittaya, Suwat Sopitpan, Supachok Thainoi, Songphol Kanjanachuchai, Somchai Ratanathammaphan and Somsak Panyakeow, InSb Quantum Nano-Stripes by Molecular Beam Epitaxy, The 43rd Physics and Chemistry of Surfaces and Interfaces (PCSI) (2016).

6. Thanavorn Poempool, Suwit Kiravittaya, Suwat Sopitpan, **Zon**, Supachok Thainoi, Songphol Kanjanachuchai, Somchai Ratanathammaphan and Somsak Panyakeow, Local Positional Alignment of InSb Nanostructures by Self-Assembled Epitaxial Growth on Ge Substrate, The 60th International Conference on Electron, Ion, and Photon Beam Technology and Nanofabrication (EIPBN-60) (2016).

7. **Zon**, Thanavorn Poempool, Suwit Kiravittaya, Suwat Sopitpan, Supachok Thainoi, Songphol Kanjanachuchai, Somchai Ratanathammaphan and Somsak Panyakeow, InSb/GaAs quantum stripes grown on on-axis (001) Ge substrate by molecular beam epitaxy, International Union of Materials Research Societies – International Conference on Electronic Materials (IUMRS-ICEM), Suntec City, Singapore, July 4th-8th (2016).

8. Thanavorn Poempool, **Zon**, Suwit Kiravittaya, Suwat Sopitpan, Supachok Thainoi, Songphol Kanjanachuchai, Somchai Ratanathammaphan and Somsak Panyakeow, Type II InSb/GaAs and type III InSb/InAs nanostructures :Molecular beam epitaxial growth and their characterization, The 33rd International Conference on the Physics of Semiconductors (ICPS) (2016).

9. **Zon**, Thanavorn Poempool, Suwit Kiravittaya, Suwat Sopitpan, Supachok Thainoi, Songphol Kanjanachuchai, Somchai Ratanathammaphan and Somsak Panyakeow, Morphology of self-assembled InSb/GaAs quantum dots on Ge substrate, The 18th International Conference on Crystal Growth and Epitaxy (ICCGE-18), Nagoya, Japan, August 7th-12th (2016).

10. Supachok Thainoi, Suwit Kiravittaya, Suwat Sopitpan, **Zon**, Songphol Kanjanachuchai, Somchai Ratanathammaphan and Somsak Panyakeow, InSb quantum nanostructures on InGaAs/GaAs substrates and their photoluminescence Properties, The 18th International Conference on Crystal Growth and Epitaxy (ICCGE-18), Nagoya, Japan, August 7th-12th (2016).

11. Suwit Kiravittaya, **Zon**, Thanavorn Poempool, Supachok Thainoi, Songphol Kanjanachuchai, Somchai Ratanathammaphan and Somsak Panyakeow, Effects of Material Intermixing on Electronic Energy Levels in Ga)As(Sb/GaAs quantum dots, Proceedings of the Electrical Engineering/Electronics, Computer, Telecommunications Information Technology Conference (ECTI-CON) (2016).

12. Suwit Kiravittaya, Supachok Thainoi, **Zon**, Somchai Ratanathammaphan, Songphol Kanjanachuchai, Somsak Panyakeow, Toward Quantum State Manipulation in Twin InSb/GaAs Quantum Dots, Proceedings of the International Electrical Engineering Congress (iEECON) (2017).

13. **Zon**, Supachok Thainoi, Suwit Kiravittaya, Aniwat Tandaechanurat, Somsak Panyakeow and Yasutomo Ota, Satoshi Iwamoto, Yasuhiko Arakawa, Photoluminescence Properties of GaSb/GaAs Quantum Dots Grown on Ge and GaAs Substrates, the 64th JSAP Spring Meeting, Yokohama, Japan, March 14th-17th (2016).

14. **Zon**, Pakawat Phienlumlert, Supachok Thainoi, Suwit Kiravittaya, Aniwat Tandaechanurat, Noppadon Nuntawong, Suwat Sopitpan, Visittapong Yordsri, Chachana Thanachayanont, Songphol Kanjanachuchai, Somchai Ratanathammaphan, Somsak Panyakeow, Yasutomo Ota, Satoshi Iwamoto and Yasuhiko Arakawa, Unique polarization-dependent photoluminescence property of GaSb/GaAs quantum dots on (001) Ge substrate grown by molecular beam epitaxy, Compound semiconductor week CSW, Cambridge. MA, USA, 29th May-1st June (2018).

15. **Zon**, S .Thainoi, S .Kiravittaya, A .Tandaechanurat, N .Nuntawong, S .Sopitpan, V .Yordsri, C .Thanachayanont, S .Kanjanachuchai, S .Ratanathammaphan, S . Panyakeow, Anti-phase domain induced morphological difference of self-assembled InSb/GaAs quantum dots grown on Ge substrate, 20th International Conference on Molecular Beam Epitaxy, Shanghai, China, September 2nd-7th (2018). (Accepted)
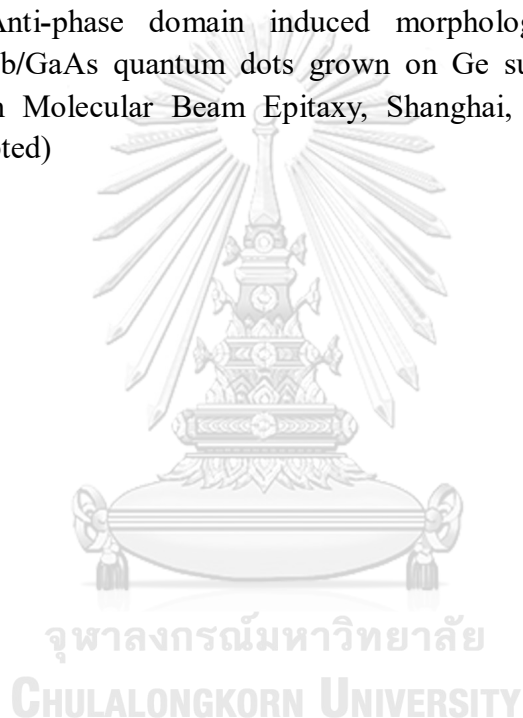
VITA

Zon was born in Mandalay, Myanmar on June 24, 1986. She entered East Yangon University specializing in Physics in 2002. She received Bachelor of Science (Physics) (Honours) in 2006 and Master of Science (Physics) in 2009 from East Yangon University. Then she moved to the University of Yangon in 2011 for Doctoral degree doing research on material science.

While she was attending in the University of Yangon, she received the scholarship supported by the Japan International Cooperation Agency (JICA) for ASEAN University Network/South-East Asia Engineering Education Development Network (AUN/SEED-Net) in August 2014 for integrated direct Ph.D program.

She entered the Graduate School of Chulalongkorn University, Thailand in August 2014 as a student for Doctoral degree at Semiconductor Device Research Laboratory (SDRL), Department of Electrical Engineering, Faculty of Engineering. Her research interest is nano-electronics and photonics of III-V compound semiconductors.